UC Irvine

UC Irvine Electronic Theses and Dissertations

Title

ALD-Functionalized Plasmonic Nantennas: Towards a Platform for Single-Molecule Studies of Photocatalysis

Permalink

https://escholarship.org/uc/item/4r02b1j8

Author

Luan, Zhongyue

Publication Date

2019

Peer reviewed|Thesis/dissertation

eScholarship.org Powered by the California Digital Library
University of California

UNIVERSITY OF CALIFORNIA,
IRVINE

ALD-Functionalized Plasmonic Nantennas: Towards a Platform for Single-Molecule Studies of Photocatalysis

DISSERTATION

submitted in partial satisfaction of the requirements
for the degree of

DOCTOR OF PHILOSOPHY

in Materials Science and Engineering

by

Zhongyue Luan

Dissertation Committee:
Associate Professor Matt Law, Chair
Associate Professor Daniel Mumm
Assistant Professor Allon Hochbaum

2019

Part of 1.1 reproduced with permission from ref 25. © IOP Publishing
Part of 1.1 reprinted with permission from ref 14. © 2011, American Chemical Society
Part of 1.1 reprinted by permission from Springer Nature Customer Service Centre GmbH: Nature, Ref 49, © 2013
Part of 1.2 reprinted from Ref 59, © 2014, with permission from Elsevier
Part of 1.2 reprinted with permission from ref 54. © 2005, American Chemical Society
Part of 1.2 reprinted with permission from ref 52. © 2010, American Chemical Society
Part of 1.2 reprinted by permission from Springer Nature Customer Service Centre GmbH: Plasmonics, ref 60, © 2016
Part of 1.3 reprinted by permission from Springer Nature Customer Service Centre GmbH: Nature Reviews Materials, ref 78, © 2016
Part of 1.3 reprinted with permission from ref 85. © 2009, American Chemical Society
Part of 1.3 reprinted from ref 86, © 2009, with permission from Elsevier
Part of 1.3 reproduced with permission from ref 88. © 2011 SPIE
Part of 1.3 republished with permission of Royal Society of Chemistry, from ref 95. © the Owner Societies 2008
Part of 2.2 reprinted with permission from ref 237. © 2014 American Chemical Society
Part of 2.2 reprinted from ref 238, with the permission of AIP Publishing. © 2005 American Institute of Physics
Part of 5.2 reprinted with permission from ref 296. © 2014 American Chemical Society
All other materials © 2019 Zhongyue Luan

DEDICATION

To

my love Qingqing Xu

my mother Shuyan Wang

my father Fulin Luan

my daughter Ellie Luan

in recognition of their love and support

TABLE OF CONTENTS

LIST OF FIGURES

Page

LIST OF TABLES

Page

ACKNOWLEDGMENTS

First and foremost, I would like to thank my parents for their consistent support. It is their active support both mentally and financially that makes it possible for me to continue my education all the way through. As the 1st generation college student in my family, I feel grateful to them for their prudent decision to send me abroad for higher education.

Pursuing a Ph.D. is a tough journey, especially for an international student like me who needs to face both academic and cultural challenges. As my PI, Matt helped me go through the hardest time during this journey. I appreciate the time he has spent with me to motivate me, making progress in this challenging project. More importantly, the problem solving and critical thinking skills I have learned from him will benefit me far beyond graduate school. It is my great pleasure to spend six years of my life to work with him.

Among all the senior students who have mentored me, I especially want to thank Dr. Vineet Vijayakrishnan Nair for his great patience to teach me from the ground level undergrad till I become an independent researcher in the lab. I was also lucky enough to meet and shadow other greatest 1st generation "law labers" including Dr. Jason Tolentino, Dr. Moritz Limpinsel, Dr. Mark Gibbs, Dr. Amanda Weber, and Dr. Nima Farhi. Their generous help regarding my future career shows me the strong connections we have does not fade over time. As the 2nd generation "law labers" myself, my success completion of the program ties strongly to the help from my lab mates Alex Abelson, Caroline Qian, Trenton Salk, Yash Gargasya, Andy Yang, Dr. Kan Fu, Dr. Juliette Micone, Dr. Claire Elizabeth, Dr. Sam Keene, Dr. Christian Engelbrekt, Dr. Deep Punj, Dr. Chao Yi, and Dr. Darren Neo. Besides, my collaborators and friend Dr. Kate Rodriguez, Henrik Gabold, Karolina Sokołowska, and John Houlihan have worked with me shortly while fruitfully. On the other hand, I was happy to mentor Stephanie Jean, Avetis Pisikyan, and Komal Syed as they gave me the chance to share my knowledge and inspire young scientist in this field.

Along with my Ph.D. research, it is truly my honor to serve the Irvine Materials Research Institute (IMRI) as a lab assistant for five years. Not only my research depends on the state-of-the-art instruments in IMRI, but also the development of my technical skills benefits from the staff scientists Dr. Toshihiro Aoki, Dr. Qiyin Lin, Dr. Ich Tran, Dr. Li Xing, and the director Dr. Jian-Guo Zheng there. I would also like to thank Dr. Dmitry Fishman from the Laser Spectroscopy Labs (LSL), Dr. Philip Dennison from the NMR Facility, and Dr. Felix Grun from the Mass Spectrometry Facility for their help in specific topics of my thesis.

As a member supported by the Chemistry at the Space-Time Limit (grant number CHE-1414466), I'm grateful to Dr. V. Ara Apkarian for his mind-opening discussion and Dr. Venkat Bommisetty, Tammy Livingstone, Danielle Watt for managing the CaSTL "family".

Special thanks to the Junor family for sharing the best time with my family.

I cannot think of any words that can express my gratitude to my darling, Qingqing Xu, who is willing to share her life with me. I love you.

CURRICULUM VITAE

Zhongyue Luan

EDUCATION

University of California, Irvine 2019
Ph.D. in Materials Science and Engineering
Advisor: Matt Law

University of California, Irvine 2015
M.S. in Materials Science and Engineering

China University of Geosciences, Beijing 2012
B.S. in Materials Chemistry

Experience

Collaborative bilingual materials scientist with six years' experience on metal/metal oxide nanomaterials synthesis, semiconductor characterization, and device fabrication towards plasmonic and solar fuel applications. Participate in building materials characterization facilities and developing cutting-edge thin film deposition equipment from the ground up to meet quality, reliability, productivity, and functionality requirements. Work as a lab assistant to provide scientific support to researchers and perform 24/7 on-call instrument maintenance in Irvine Materials Research Institute (IMRI) for five years.

PUBLICATIONS

Luan, Z., Abelson, A., Law, M. (2019). Reversible Aggregation of Covalently Cross-Linked Gold Nanocrystals by Linker Oxidation. *In Preparation*

Pala, R., Mohieldin, A. M., Sherpa, R. T., Kathem, S. H., Shamloo, K., Luan, Z., ... & Nauli, S. M. (2019). Ciliotherapy: Remote Control of Primary Cilia Movement and Function by Magnetic Nanoparticles. *ACS nano*.

Gabold, H., Luan, Z., Paul, N., Opel, M., Müller-Buschbaum, P., Law, M., & Paul, A. (2018). Structural and magnetic properties of cobalt iron disulfide (Co x Fe 1− x S 2) nanocrystals. *Scientific reports*, *8*(1), 4835.

Seraya, E., Luan, Z., Law, M., & Heyduk, A. F. (2015). Synthesis of Catecholate Ligands with Phosphonate Anchoring Groups. *Inorganic chemistry*, *54*(15), 7571-7578.

ABSTRACT OF THE DISSERTATION

ALD-Functionalized Plasmonic Nantennas:
Towards a Platform for Single-Molecule Studies of Photocatalysis

By

Zhongyue Luan

Doctor of Philosophy in Materials Science and Engineering

University of California, Irvine, 2019

Professor Matt Law, Chair

In the recent push toward single molecule spectroscopy and photochemistry, plasmonic nanostructures have emerged as an attractive and experimentally tractable design. We have developed a versatile experimental platform based on plasmonic core-shell nanocrystal dimers (termed nantenna) using colloidal assembly and atomic layer deposition (ALD) to achieve functional, stable structures for single-molecule time-resolved studies of charge transfer reactions and chemical transformations important in (photo)electrocatalysis and plasmon-driven chemistry.

The steady-state SERS study has been performed on two platforms as a proof-of-concept: Platform I consists of Ag/TiO_2/N719/TiO_2; Platform II consists of Au/TiO_2/DBDT/Al_2O_3. Later, we explored the reversible assembly of citrate-capped Au NCs and hexa(ethylene glycol) dithiol (HEGDT). The dithiol-triggered polymerization of the Au NCs results in complete precipitation of the NCs in a short time. However, we have shown that by injecting an appropriate oxidizing reagent into the solution, we can oxidize the dithiols to disulfonic acids, resulting in the destruction of the dithiol linkers and complete

depolymerization of the Au NCs to re-form a stable colloidal solution of individual Au NCs. We have studied the polymerization and depolymerization process with a suite of methods (optical absorption spectroscopy, FT-IR, DLS, SAXS, XPS, TEM, NMR, mass spectrometry, zeta potential, and pH measurements) to establish details of the chemistry and learn how to arrest the polymerization reaction, with a goal of a stable colloidal suspension of dimers.

Lastly, we investigated a facile synthesis of 100% dimers by triggering the surface thiol-ene click reaction under plasmonic heating around dimers. The PEGylated maleimides and acrylates are identified as the most effective reagent to passivate the dithiol-triggered aggregation through NMR kinetics study and click reaction in Au NCs suspension. The initial study of illuminating Au NCs monomers at different wavelengths demonstrates the plasmonic heating effect successfully.

1 Introduction

1.1 Localized Surface Plasmon Resonance (LSPR)

1.1.1 Plasmons, Localized Plasmons, and Nantennas

Plasmons are quantization of plasma oscillation which contains collective oscillations of the free electron gas[1,2]. In analogy to the plasma (ionized gas[3,4]), surface plasmon (SP) can be treated as coherent displacement of the electron cloud from their equilibrium positions induced by light waves traveling at the interface of metal and dielectrics under a specific condition in solid materials[5,6]. Plasmons can propagate along with the interface when the wave vector of the incoming light is nearly parallel to the metal surface due to the strong coupling between electromagnetic (EM) wave and free electron gas (Figure 1.1 A top). In this case, the propagating surface plasmons like water waves are defined as surface plasmon polaritons (SPP). On the contrary, the plasmons cannot propagate within a metallic nanocrystal (NC) when the size of the NC is much smaller than the wavelength of incoming light (Figure 1.1 B). In this case, the polarized conductive electrons that are "trapped" around the NCs are defined as localized surface plasmons (LSP). The negatively charged electrons collectively oscillate around the positively charged nucleus (protons) in response to ligh via simple Coulomb attraction[2,5,6]. This is similar to a wired antenna working in receiving mode to convert EM waves at radio frequency to oscillating electric current[7,8]. Thus, metallic NCs that exhibit such properties colloquially termed *nano-antenna* (abbreviated as *nantenna*). The NCs can also act like a nano-emitter in analogy to the antennas in transmission mode.

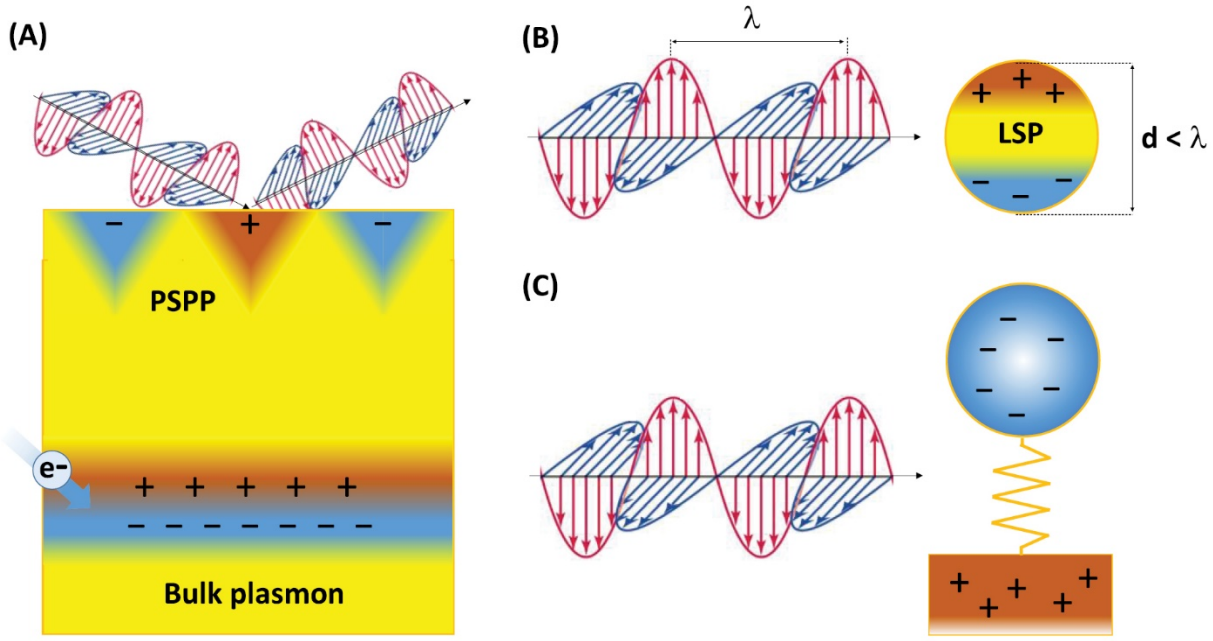

Figure 1.1 Illustration of bulk and surface plasmons.

(A) Bulk plasmons excited by electron wave (bottom) and SPP excited by the evanescent wave (top). (B) LSPR of Au NCs excited by light, (C) Harmonic oscillator approximation of the LSPR in Au NCs. Reproduced with permission from ref 25. © IOP Publishing.

1.1.2 Factors Affecting Plasmonic Properties

Models have been developed to gain a conceptual understanding of factors influencing the LSPR. The simple damped harmonic oscillators (HOs) approximation has been employed successfully to explain the redshift of the near field properties (extinction, scattering, and absorption) peak comparing to the far field properties (spatial and intensity distribution of the EM field enhancements)[9,10,11] peak. In this model, the electrons collectively oscillate as a dipole in resonance with the electric field of the EM wave (Figure 1.1 C). To employ the HO approximation, the electron density is treated as mass, and the Coulomb force between electrons and nucleus corresponds to the spring constant[9,10,11]. In

1908, Gustav Mie solved Maxwell's equations and described the scattering, absorption, and extinction of light by spherical particles much smaller than the wavelength of light[12]. The widely accepted LSPR extinction σ_{ext} and scattering σ_{sca} cross-section of NCs derived from Mie theory are shown below:

Equation 1 Relationship between extinction, scattering, and absorption cross-section[13].

$$\sigma_{ext} = \sigma_{sca} + \sigma_{abs}$$

Equation 2 The complex metal dielectric constant.

$$\tilde{\varepsilon} = \varepsilon_1(\lambda) + i\varepsilon_2(\lambda)$$

Equation 3 Extinction cross-section of a spherical particle[14].

$$\sigma_{ext} = \frac{18\pi\varepsilon_m^{3/2}V}{\lambda} \frac{\varepsilon_2(\lambda)}{[\varepsilon_1(\lambda) + 2\varepsilon_m]^2 + \varepsilon_2(\lambda)^2}$$

Equation 4 Scattering cross-section of a spherical particle[14]

$$\sigma_{sca} = \frac{32\pi^4\varepsilon_m^2V^2}{\lambda^4} \frac{[\varepsilon_1(\lambda) - \varepsilon_m]^2 + \varepsilon_2(\lambda)^2}{[\varepsilon_1(\lambda) + 2\varepsilon_m]^2 + \varepsilon_2(\lambda)^2}$$

where λ is the light wavelength, ε_m is the real part of the dielectric constant of the medium (assuming the medium does not absorb light), V is the volume of the particle. The complex metal dielectric constant follows Equation 2. The absorption cross-section σ_{abs} can be derived from Equation 1. From the equations above, it is obvious that:

1. The far-field plasmonic property of the material (any dielectric "scatterer") fundamentally depends on its $\tilde{\varepsilon}$. Also, it changes with the incident light as the $\tilde{\varepsilon}$ is frequency dependent. The polarization direction of light plays another important role when discussing anisotropic shape particles.

2. σ_{ext}, σ_{sca}, and σ_{abs} increase linearly with V. It is hard to distinguish small objects from a background of large objects due to the rapid scaling of σ_{sca} with respect to a^6 (a is the radius of the spherical particle).

3. The LSPR peaks when $\varepsilon_1(\lambda) = -2\varepsilon_m$ (Fröhlich condition[15,16]). Clearly, the peak position of the LSPR depends on the medium ε_m as well. In this thesis, the predicted peak position (524 nm, Figure 5.1, right) is very close to the experimentally observed peak position (527 nm, Figure 4.7 b) of 24 nm Au NCs.

4. While $\varepsilon_1(\lambda)$ defines the LSPR peak frequency, $\varepsilon_2(\lambda)$ defines the peak width (broadening) as a damping term due to the processes including radiative damping[10,17,18], electron-electron/phonon/defect scattering[19,20,21], and metal heating losses[22,23,24,25]. Particularly, the heating losses mechanism of the plasmon damping (decay) is used in this study to selective trigger the passivation reactions on NC dimers (section 5.1).

The optical properties of nanoparticles can be predicted well based on the above equations. For example, assuming the Au and Ag nanoparticle have the same size, shape, and surrounding environment. To satisfy the Fröhlich condition ($\varepsilon_{1Ag} = \varepsilon_{1Au} = -2\varepsilon_m$), the LSPR wavelength of Ag is always blue-shifted relative to Au due to the real part of their dielectric constant (Figure 1.2 a). In addition, Au suffers higher loss than Ag (ε_{2Au} is higher than ε_{2Ag}) due to the interband transition that occurs near the LSPR peak region, which results in the decay of the surface plasmons into electron-hole pairs. Whereas the

frequency that allows the interband transition in Ag is higher than the its screened plasmon frequency[26]. The extinction spectrum of Au NCs (Figure 3.1 b) shows a clear increase below 450 nm compared to Ag NCs (Figure 3.6 b), due to this interband transition. However, Au NCs are more widely used than Ag NCs due to its higher biological and chemical compatibility. Our early work showed even brief (less than 10 seconds) UV/Ozone treatment or transition metal ion exposure significantly altered the shape of Ag NCs (Figure 3.5). In addition, SERS signal of N719 decayed nearly exponentially over time from Ag NC clusters which might be an indication of instability of the structure (Figure 3.3). On the contrary, Au NCs exhibit great stability in strong oxidizing environments or under laser illumination. 1 hour of continueoues ozone bubbling or 2 mW/cm^2 laser illumination at the LSPR peak frequency did not change the NCs at all based on the extinction spectrum.

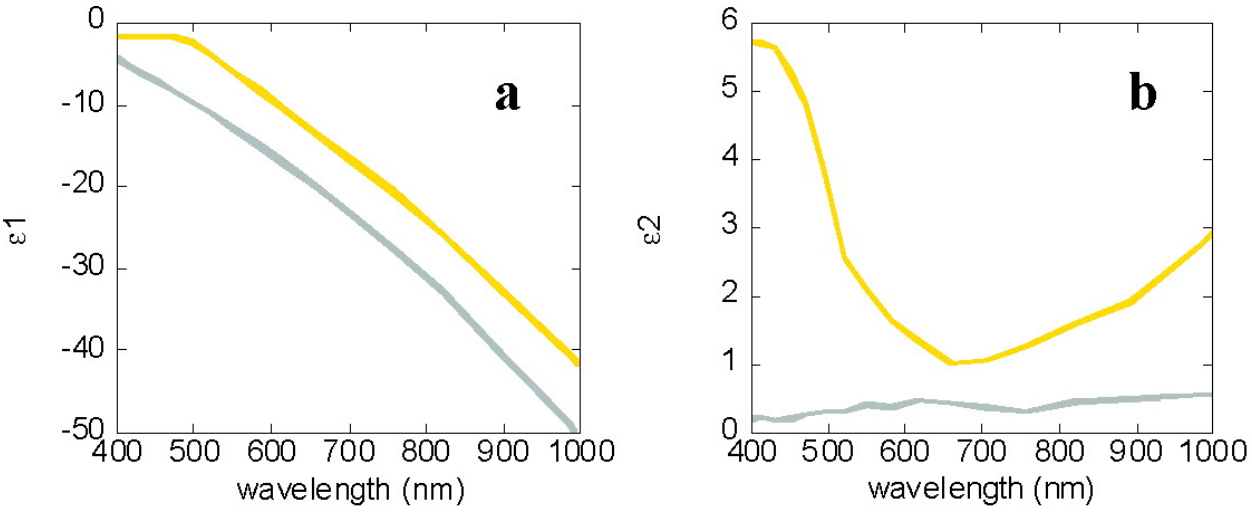

Figure 1.2 Complex dielectric constant of Au and Ag.

(a) Real and (b) imaginary parts of the complex dielectric constant of Au (upper curves) and Ag (lowers curves). Reprinted with permission from ref 14. © 2011, American Chemical Society.

As development of Mie theory, Richard Gans[27] took the three dimensions of spheroidal particles into consideration in 1912. The absorption cross-section σ_{sca} is then modified to Equation 5 for a prolate spheroid which is obtained by rotating ellipse along one of the long axis A (short axis B = C < A). Here, ω is the frequency of the light, c is the speed of the light, P_j is the depolarization factors, R is the aspect ratio. The anisotropic shape of the particle eventually leads to the anisotropic depolarization factors which result in two LSPR peaks. The transverse plasmon mode from B and C axis plus the longitudinal plasmon mode from A axis consist of the absorption cross-section of the spheroidal particle. Equation 5 reveals the importance impact of the aspect ratio on the plasmonic properties of the materials. Other factors that affect the plasmonic protreptics such as absorbing dielectric medium[28], plexcitons[29], surface chemistry[30], temperature[31], quantum effect[32], and plasmon coupling[33] are not discussed here. The effect of plasmon coupling in nanoparticle dimer is discussed in section 1.3.2.

Equation 5 Absorption cross-section of spheroidal particle[14].

$$\sigma_{abs} = \frac{\omega}{3c}\varepsilon_m^{3/2} V \sum_j \frac{\left(1/P_j^2\right)\varepsilon_2}{\left\{\varepsilon_1 + \left[\left(1-P_j\right)/P_j\right]\varepsilon_m\right\}^2 + \varepsilon_2^2}$$

$$P_A = \frac{1-e^2}{e^2}\left[\frac{1}{2e}\ln\left(\frac{1+e}{1-e}\right)\right] - 1 \qquad P_B = P_C = \frac{1-P_A}{2}$$

$$e = \left[1 - \left(\frac{B}{A}\right)^2\right]^{1/2} = \left(1 - \frac{1}{R^2}\right)^{1/2}$$

1.1.3 Methods to Study LSPR Modes

One can derive the red-shift of the longitudinal plasmon peak concerning a larger aspect ratio from Equation 5. In the case of NC aggregation, we observed the same red-shift as the aggregates grew larger (Figure 3.2 and Figure 3.7). While Equation 5 is intuitive to show the impact of shape/aspect ratio, it is hard to apply the same method to analyze more complicated structures. Instead, numerical methods such as the finite difference time domain (FDTD) simulation[34,35,36], the discrete dipole approximation (DDA)[37,38,39], and the finite element method (FEM)[40,41] have been used to predict the optical properties of NCs[42]. FDTD simulation of the extinction cross-section of Au NC dimer with different inter-NC spacing (Figure 5.1) has been used as guidance to selectively pump the longitudinal plasmon mode of dimers in this study (section 5.1).

On the other hand, the simple optical extinction (UV-Vis) spectrum has been used widely to probe the LSPR of NCs colloidal suspension. While the extinction spectrum provides a semi-quantitative in situ approach to trace the NCs in the solution, it is an ensemble measurement which contains all possible plasmon modes from particles rotating in all directions. Thanks to recent advances in electron microscopy, electron energy loss spectroscopy[43,44] (EELS), energy filtered TEM[45,46] (EFTEM), and cathodoluminescence spectroscopy (CL)[47,48], we can now image plasmons directly the single particle limit. Figure 1.3 a and b compare the extinction spectrum of Ag nanocube (35 nm) solution made during this study and ensemble EELS spectrum of single Ag nanocube (100 nm) acquired at two tilting angles and 5 locations under vacuum in the electron microscope[49].

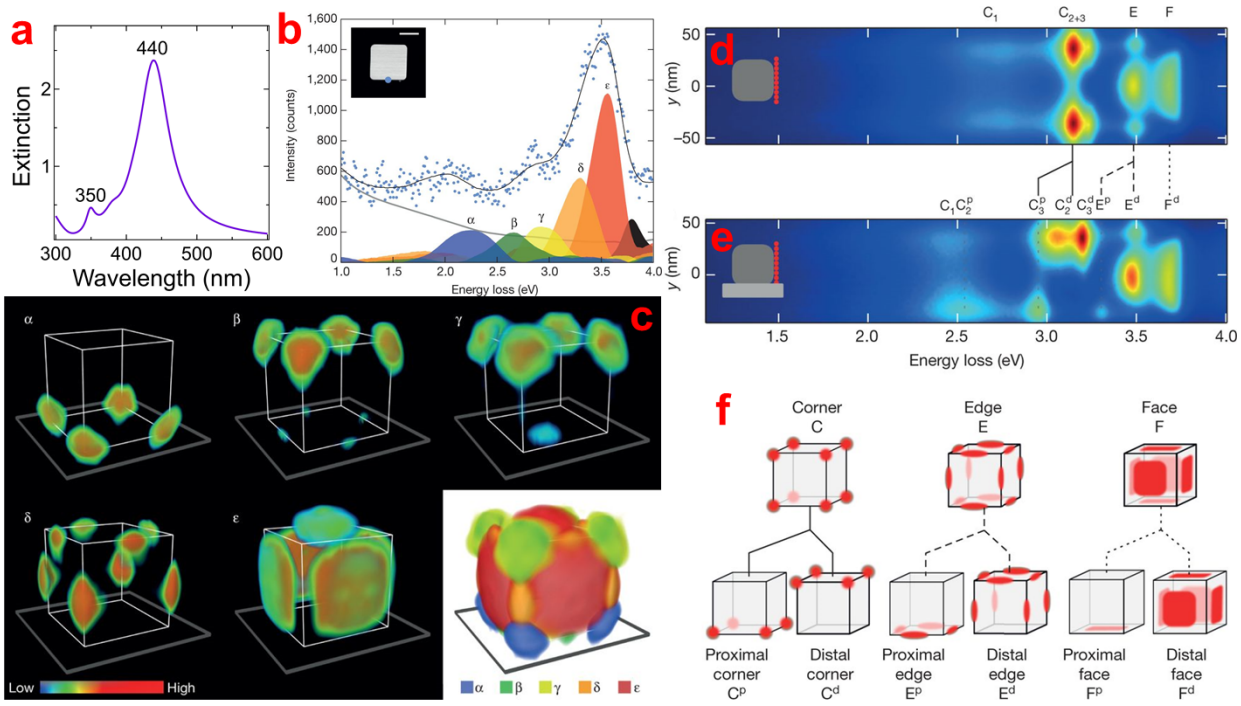

Figure 1.3 Comparison of experimental and numerical studies of Ag nanocubes.

(a) Extinction spectrum of 35 nm Ag nanocube made in our lab. (b) Nonnegative matrix factorization (NMF) spectral components weighted based on the value at the blue dot in the inset (100 nm Ag nanocube). Five components α, β, γ, δ, and ε are assigned to the unprocessed spectrum (blue dots). Ag volume plasmon is assigned as the black area. The grey line consists of zero loss peak (ZLP) tail, contamination, and low energy diploe loss. The black line is the sum of all components. (c) 3D tomographic reconstruction of the LSPR components from EELS mapping. DDA simulation of line spectra starts from the face of Ag nanocube in the vacuum (d) and on the silicon nitride substrate (e). (f) Scheme of the hybridization plasmon modes induced by the substrate. Reprinted by permission from Springer Nature Customer Service Centre GmbH: Nature, Ref 49, © 2013.

The overall shape of the two spectrums are quite similar despite the shift in LSPR peak due to different particle sizes and ε_m. In addition, the EELS spectrums taken at different locations on a Ag nanocube contain location information of individual plasmon modes which make precise plasmon 3D reconstruction possible (Figure 1.3 c). The complementary DDA simulation further reveals the origin of the proximal component (close to the substrate) and distal component (away from substrate) of the plasmon modes (Figure 1.3 d-f).

1.2 Applications of LSPR

1.2.1 Optical Extinction

From the above discussion, the optical properties (especially the LSPR peak position) of NCs are sensitive to the medium (ε_m). Alternatnion of the environment or attaching molecules on the surface may alter the LSPR significantly. This give rise to a whole field of optical sensing applications for gaseous molecules[50,51]. In this study, we observed the LSPR peak of Au NCs shifted immediately upon carbon monoxide or ozone bubbling into the solution (Figure 1.4 c). With a spectrometer capable of measuring small spectral shifts on the order of 10^{-3} nm, inert gas sensing can be achieved with fast response[52] (Figure 1.1 d). While the absorption cross-section σ_{abs} scales with a^3 (Equation 5), the scattering cross-section σ_{sca} scales with a^6 (Equation 4). A 40 nm Au NC scatters 4-5 order of magnitude more light than the light emission form a typical dye[53]. Combining other unique properties including high surface-to-volume ratio, easy synthesis and functionalization, biocompatibility, photostability, chemical stability, low luminescence, and LSPR rapid

relaxation, Au NCs are ideal for labeling and imaging cells[54], DNA[55], and proteins[56,57,58] (Figure 1.4 b). Unlike other imaging techniques which require complicated system design, expensive optical components, and complex image processing, imaging of highly efficient "scatterers" only requires a simple dark field condenser which collects scattered light at high angles[59] (Figure 1.4 a).

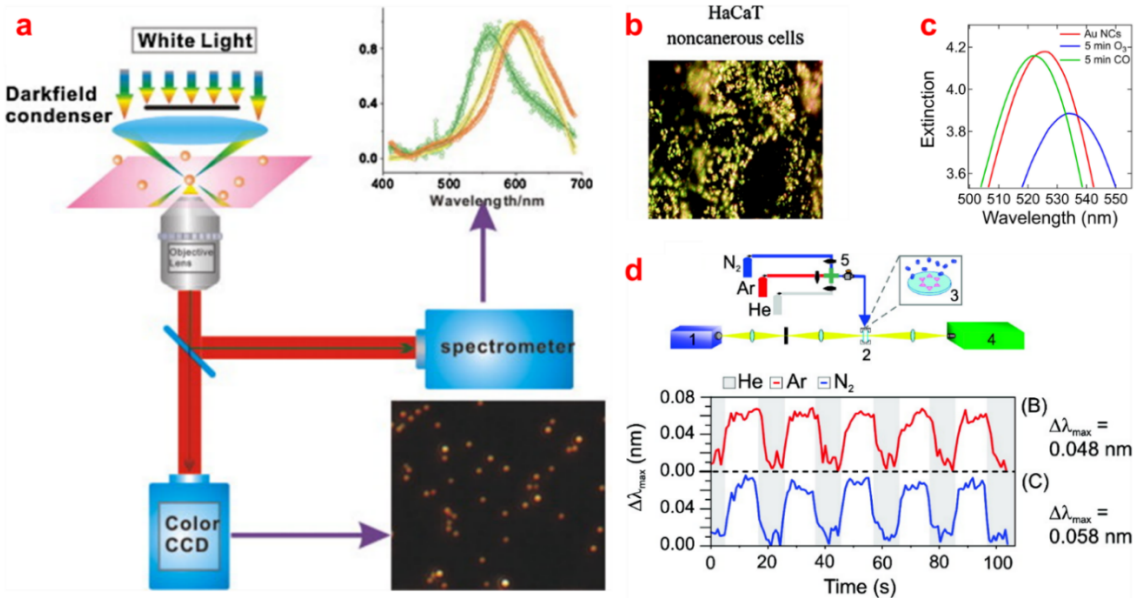

Figure 1.4 Imaging and sensing applications using LSPR.

(a) Scheme of the typical dark-field imaging/spectroscopy setup. (b) Dark-field image of HaCaT noncancerous cells decorated with Au NCs conjugated to anti-EGFR. (c) Extinction spectrum of Au NCs solution treated with O_3 or CO for 5 minutes. (d) (top) HR-LSPR gas sensing setups with lamp, flow cell, Ag NCs on substrate, spectrometer, and gas dosing system. (bottom) Change of LSPR peak position of Ag NCs versus time after treating with He, Ar, or N_2. (a) Reprinted from Ref 59, © 2014, with permission from Elsevier. (b) Reprinted with permission from ref 54. © 2005, American Chemical Society. (d) Reprinted with permission from ref 52. © 2010, American Chemical Society.

1.2.2 Local-field Enhancement

From the simple damped harmonic oscillator (HO) approximation, the collective oscillation of electrons (plasmons) is driven by the incoming EM wave. Thus, the frequency of the plasmon is close to the EM wave (driving force) which in turn leads to significant enhancement of the EM field locally around the particle due to the plasmon resonance[60] (Figure 1.5). The particles act like "nano lenses", which amplify the incoming light. The enhancement of various optical effects has been studied, such as absorption at visible/IR region[61,62], photoluminescence[63,64], fluorescence[65,66], Raman scattering[67,68], optical force[69,70], and other nonlinear optical phenomena[71,72]. Notably, the surface-enhanced Raman spectroscopy (SERS) which will be used to conduct single-molecule studies of photocatalysis in our research is discussed in the following section in details.

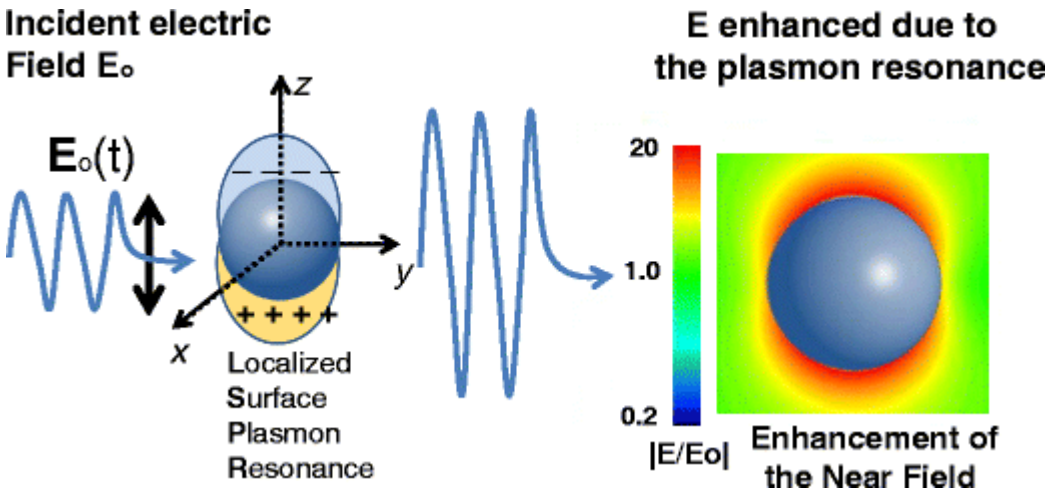

Figure 1.5 Scheme of the LSPR and FEM simulation of electric field enhancement.

Reprinted by permission from Springer Nature Customer Service Centre GmbH: Plasmonics, Ref 60, © 2016.

1.3 Surface-enhanced Raman spectroscopy (SERS)

1.3.1 Enhancement Mechanism

While the exact enchantment mechanism is still under debate especially the "chemical enhancement" due to charge transfer between molecule and metal[73,74], it is generally believed the enhancement mechanism that contributes most to the signal is a two-step process (Figure 1.6) related to the local electric field[75]. Step 1, the LSPR of the nantennas which has received EM waves at a frequency of ω_0 are excited. In return, the exited dipolar plasmon (dipole of the particle) radiates light as dipolar radiation. The radiation is coherent with the excited field, thus constructive or destructive interference occurs which results in a spatial distribution of the EM field enhancement[76]. Step 2, the induced dipole of the molecules and the dipole of the particle are mutually excited at a frequency of ω_R. The SERS enhancement factor $G(\omega)$ is proportional to the square of the ratio between the local electric field with and without particle ($E_{loc}(\omega)/E_0(\omega)$). The total enhancement factor G from step 1 and 2 is expressed in Equation 6. Note, the above model of simple spherical particle dimer provides a pictorial description of the enhancement mechanism. Numerical methods mentioned in section 1.1.3 are needed to describe more complicated system considering factors such as the vectorial nature of the fields[76] and the hybridization of different plasmon modes[77].

Equation 6 SERS enhancement factor[78].

$$G = G_1(\omega_0)G_2(\omega_R) = \frac{|E_{loc}(\omega_0)|^2|E_{loc}(\omega_R)|^2}{|E_0(\omega_0)|^2|E_0(\omega_R)|^2} \approx \frac{|E_{loc}(\omega_R)|^4}{|E_0(\omega_0)|^4}$$

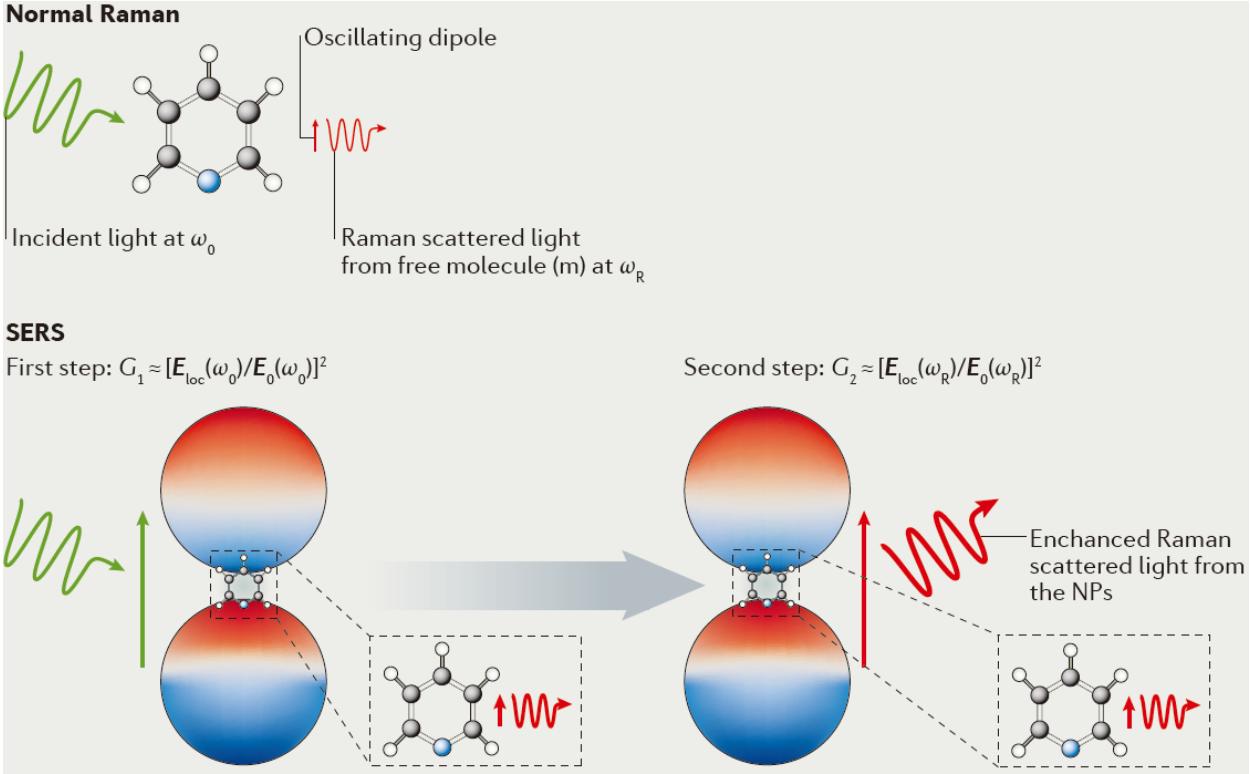

Figure 1.6 Scheme of SERS enhancement mechanism.

Reprinted by permission from Springer Nature Customer Service Centre GmbH: Nature Reviews Materials, Ref 78, © 2016

1.3.2 Larger Enhancement toward Single Molecule SERS

From the discussion above, the strong local electric field induced by LSPR enhances both incoming EM waves and outgoing Raman scattered light. The fact that the Raman enhancement factor (EF) is the 4th power of the electric field enhancement further amplifies the effect. This enables a new field of single-molecule Raman spectroscopy which otherwise would be impossible due to the extremely low signal[79]. However, the enhancement from single nanoparticle wasn't large enough to see signals from the single molecule during the early stage of SERS study. Thus, most studies used small clusters to

boost the chance of finding molecules residing in the junction ("hotspots")[80,81]. Structures with more defined geometry were developed with top-down or bottom-up methods[82], which will be discussed in the next section.

In order to assemble the structure with larger EF rationally, it is vital to understand the origin and factors that contribute to the electric field enhancement within the junction first. Starting from a single particle, the factors that impact the plasmonic properties discussed in section 1.1.2 play an important role here as well. Fundamentally, the enhancement depends on the complex dielectric constant of the material. Other than the highly effective Ag, Au and Cu, studies have shown that other metals such as Li, Na, K, In, Pt, Fe, Co, Ni, Ru, Pd, Al, and certain alloys also present weak LSPR upon excitation[83]. Besides, SERS intensity (electric field enhancement) at the area with higher curvature is much higher due to the "lightning rod" effect and suppressed interband transition at a higher wavelength[84]. As a result, synthesis methods for non-spherical particles with a sharp edge or corner have been developed. Figure 1.7 a-b compared the electric field enhancement of Ag sphere versus cube. The calculated EF at 0.5 nm above the surface along the edge of a cube is 400 times higher than that fo a sphere[85]. Another important consideration is the polarization dependence of the EF in both single asymmetric particle and particle assembly. The most significant EF of cube structure is achieved when the polarization is along the face diagonal direction[86] (Figure 1.7 c, top role).

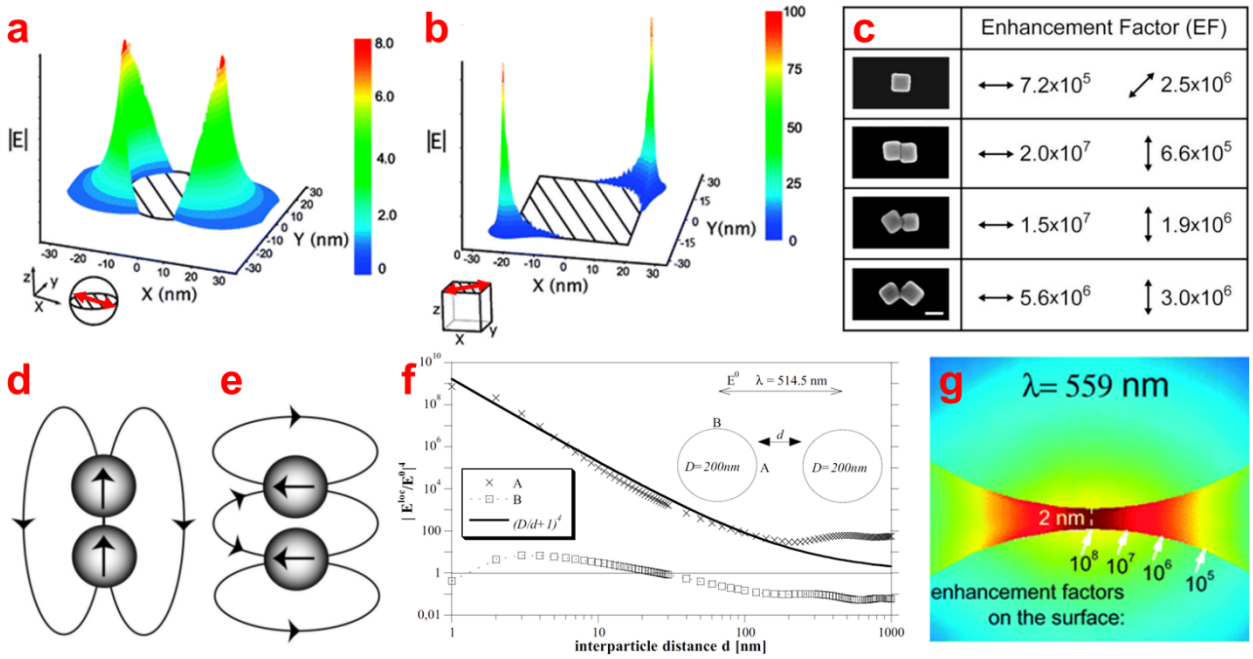

Figure 1.7 Dependence of SERS enhancement.

DDA calculated electric field distribution of (a) d = 35 nm Ag sphere and (b) 38 nm Ag cube with 514 nm excitation. Red arrow indicates the light polarization direction. (c) SERS EF of 4-MBT on d = 100 nm Ag cube monomer or dimer with 514 nm excitation. Black arrow indicates the light polarization direction with respect to the SEM image. Scheme of induced dipole moments coupling in metal nanoparticle dimer excited by light polarized in parallel (d) and perpendicular (e) direction to the dimer's main symmetry axis. (f) Calculated[87] EF of d = 200 nm Ag sphere dimer with 514.5 nm excitation polarized along the main axis at location A and B. (g) EF distribution of d = 60 nm Au sphere dimer with 559 nm excitation polarized along the main axis. (a-b) Reprinted with permission from ref 85. © 2009, American Chemical Society. (c) Reprinted from ref 86, © 2009, with permission from Elsevier. (d-f) Reproduced with permission from ref 88. © 2011 SPIE. (g) Republished with permission of Royal Society of Chemistry, from ref 95. © the Owner Societies 2008.

Even though single asymmetric particle exhibits promising plasmonic properties already, coupling them into dimer further improves the EF by order of magnitude higher. When the polarization direction of light matches the longitudinal axis of the dimer, EF reaches 10^7 in face-to-face and corner-to-face geometry (Figure 1.7 c). Based on the simple damped harmonic oscillators (HOs) approximation, the Coulomb attraction force between free electrons and nucleus in each particle in the dimer is either increased (Figure 1.7 d) or decreased (Figure 1.7 e) by its neighbor[2,88]. Thus, we could expect a blue shift of transverse plasmon mode excited by light polarized perpendicular to the longitudinal axis. Similarly, a red shift of the longitudinal plasmon mode is expected. In general, the smaller the gap, the higher the EF (Figure 1.7 f) while it cannot increases without a limit due to the quantum effects such as coherent quantum tunneling at sub-nm scale[89,90]. Typically, dimer consists of aspherical particles[91,92] or other sophisticated structures[93,94] that designed particularly for SERS exhibit even higher EFs. Another factor that hasn't been considered so far is the spatial distribution of EF in the junction area. Figure 1.7 g shows that the highest EF around 10^8 is only limited to a volume of about 2 nm^3 between two 60 nm Au spheres[95]. The EF decreases an order of magnitude even 1 nm away from this area. It is tricky to ensure molecule loading into the right space though only one molecule is needed for SERS. Thus, dimer consists of cubes with face-to-face configuration is better than dimer with spheres due to the increased junction area.

1.4 Assemble of Nantennas

1.4.1 Controllable Aggregation towards NC Dimers

The demonstration of stable alkanethiolate-capped colloidal gold nanocrystals by Brust et al.[96] launched a wave of research on surface functionalization strategies to control the assembly of plasmonic metal nanocrystals (NCs)[97,98,99,100,101,102]. Schemes that enable NC aggregation with fine control of the aggregate size distribution are important for the application of plasmonic NCs. The random assembly of NCs with poor size distribution without proper design would not lead to better SERS substrates. The simplest and in many ways most important aggregate is the NC dimer. Despite its simplicity, the deterministic fabrication of NC dimers has proven a tremendous challenge, and no method has yet been developed for the quantitative conversion of a dispersion of individual colloidal NCs into NC dimers. The two main approaches for assembling colloidal NC dimers are asymmetric functionalization and arrested aggregation.

The former approach utilizes assembly at solid-liquid[103,104,105,106,107] or liquid-liquid interfaces[108,109] to break symmetry and selectively make dimers, but processing is complicated, and dimer yields are usually low. Arrested aggregation involves stopping the NC aggregation process at an early stage of polymerization in order to produce a dispersion of NC oligomers that contains a high percentage of dimers. This is typically achieved by using dilute reactants to ensure slow polymerization and/or terminating the polymerization by encapsulating the NCs with polymers[110,111,112,113,114,115,116], silica[117,118,119,120,121], or phospholipids[122,123]. Aggregation initiators include DNA[124,125,126,127], biotin-streptavidin[128,129], amide bond formation[130,131], dithiol

linkers[132,133,134,135,136,137,138,139,140,141,142,143], salt[144,145,146,147], poor solvents[148,149], and neutral non-bridging ligands[150,151,152]. Since NC aggregation inevitably results in a distribution of aggregate sizes (monomers, dimers, and higher oligomers), post-fabrication separation is often used to enrich the dimer content[153,154,155]. In addition to asymmetric functionalization and arrested aggregation (bottom-up strategy), several types of novel lithography (top-down strategy) have also been used to make NC dimers for SERS studies[156,157,158].

1.4.2 Reversible Aggregation

While exploring routes to the deterministic fabrication of colloidal Au NC dimers, we accidentally discovered that precipitates of Au NCs covalently cross-linked by dithiols[159] could be completely depolymerized and redispersed in water by brief exposure to ozone. Ozone has been previously used to induce reversible shifts of the LSPR of Au NCs[264,265,266,267] and to oxidize organic ligands from colloidal and surface-supported Au NCs[160,161]. Reversibility is interesting because it allows for dynamic tuning of the aggregates, real-time response to stimuli, resetting of the NC assembly to its initial state, and reuse of the NCs. Reversible NC aggregation has been demonstrated using the full gamut of non-covalent interactions, including hydrogen bonding, solvophobicity, electrostatic and van der Waals forces, and π-effects.

Reversible assembly schemes have been based on biomolecular recognition of DNA[162,163,164,165,166,167,168], aptamer-analyte[169,170,171], antibody-antigen[172,173], and protein-substrate complexes[174,175,176,177], stimuli-responsive polymer coatings triggered by pH[178,179,180,181,182,183], temperature[184,185,186,187,188], light[189,190,191], solvent

polarity[192,193,194,195], and solution composition[196], hydrogen bonding between small molecules[197,198,199,200,201,202], metal ion complexation[203,204,205,206,207], host-guest chemistry[208,209,210,211,212], charge-transfer complex formation[213], control of electrostatic stabilization by ionic strength[214], temperature[215], photoisomerization of azobenzene-functionalized ligands[216,217,218,219,220], and partial exchange with non-bridging ligands[221,222,223,224,225,226,227], and light-driven thermophoresis[228] and plasmofluidic trapping[229].

In contrast, there are few examples of reversible aggregation of metal NCs cross-linked with covalent bonds. He *et al*. employed photodimerization and photocleavage of a coumarin-functionalized thiol ligand to achieve the reversible covalent cross-linking of Au NCs[230]. Guarise and co-workers used a dithiol linker with a chemically cleavable ester backbone to depolymerize aggregates of Au NCs[231]. Displacement of multidentate thioether linkers by monothiols was shown by Lim *et al*. to result in disassembly of Au NC aggregates[232]. Current approaches rely on specialized or relatively weak covalent linkers. A general method for reversible self-assembly of covalently cross-linked Au NCs has not been demonstrated.

1.5 Scope of This Work

The goal of this work is to study space-time limited single-molecule dynamics of charge transfer reactions and chemical transformations important in (photo)electrocatalysis. ALD-functionalized plasmonic nantennas (Figure 1.8) can be a powerful platform for single-molecule SERS movie making, offering sufficient signal enhancement for single-molecule spectroscopy, reasonable control of geometry and layer thicknesses, a wide selection of

core/shell materials and molecules, and enhanced system stability with simple fabrication. The short-term focus is on platform development, and the proof-of-concept study using ALD coated stochastic NC dimers loaded with SERS reporters (DBDT) and Grätzel cell[233] dyes (N719). Synthesis, cleaning, and ALD of TiO_2/Al_2O_3 of the Ag and Au NCs will be addressed and monitored using UV-Vis, SEM, TEM, STEM, EELS, XPS, and ISS. The SERS activity of the platforms after molecule loading are verified by home build Raman spectrometer.

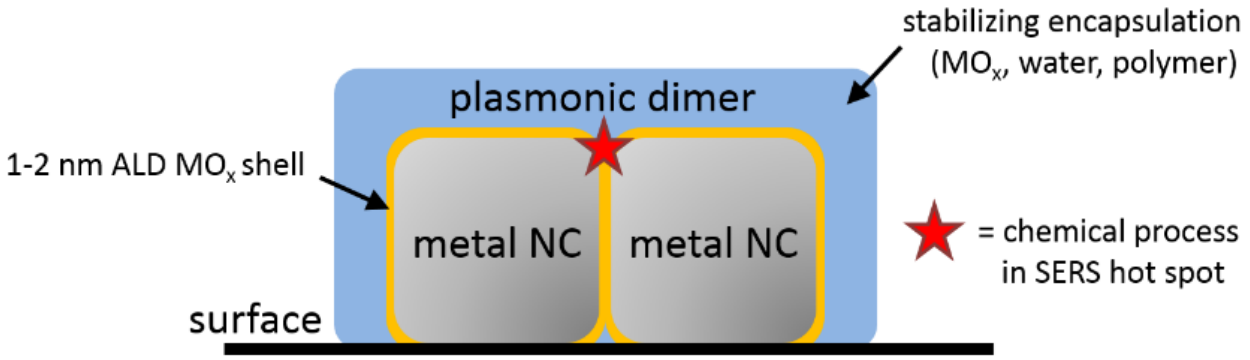

Figure 1.8 Scheme of ALD-functionalized plasmonic nantennas.

The mid-term focus is to achieve high yield and controllable dimerization of NCs using Raman silent dithiol linker. n-alkanedithiol, biphenyl-4-4'-dithiol (DBDT) and Hexa(ethylene glycol) dithiol (HEGDT) were explored as the chemical linker to trigger the dimerization of citrate-capped Au NCs. Meanwhile, the termination of the active bonding ligand (-SH) via oxidants such as ozone and H_2O_2 will be studied to stop/reverse the unwanted aggregation. UV-Vis, DLS, NTA, SAXS, and TEM are involved in monitoring the linking reaction kinetics in terms of aggregate sizes. In addition, pH, NMR, MS, and zeta potential measurement will reveal the reaction mechanism as well as the surface state of

the particles before and after oxidation. Particularly, TEM with cryo/cooling holder will be used to monitor the “true” gap distance at the hotspots without electron beam induced particle deformation. Raman spectroscopy of the linker and reporter molecules loaded at the hotspots will also prove the versatility of the platform for future single molecule studies of photocatalysis.

Finally, we will explore a new assemble method toward yielding 100% dimers from Au NC monomers by combing thiol-ene click reaction and selective plasmonic local heating.

2 Materials and Methods

2.1 Materials

All chemicals were used as received unless otherwise noted. 18.2 MΩ water (Milli-Q Gradient) was used throughout the study. Hydrogen tetrachloroaurate(III) trihydrate ($HAuCl_4 \bullet 3H_2O$, 99.99%) was purchased from Alfa Aesar. Trisodium citrate dihydrate (≥99.8%) was purchased from MP Biomedical. Hexa(ethylene glycol) dithiol (HEGDT, >97%), 2,2'-(ethylenedioxy)diethanethiol (EDD, 95%), pentaerythritol tetrakis(3-mercaptopropionate) (PTM, 95%), 1,3-propanedithiol (Pro, 99%), 1,4-butanedithiol (But, 97%), 1,5-pentanedithiol (Pen, 96%), 1,6-hexanedithiol (Hex, 99.5%), sodium hydroxide (NaOH, 97%), 3-mercaptopropionic acid (MPA, 99%), 1-thioglycerol (TG, ≥97%), thioglycolic acid, (TGA, ≥98%), 2-mercaptoethanol (ME, ≥99.0%), 11-mercaptoundecanoic acid (MUDA, 95%), 16-mercaptohexadecanoic acid (MHDA, 99%), 3-(trimethylsilyl)-1-propanesulfonic acid sodium salt (DSS sodium salt, 97%), biphenyl-4,4'-dithiol (DBDT, 95%), poly(ethylene glycol) (PEG, average M_n 400), anhydrous ethanol (>99.5%), deuterium oxide (D_2O, 99.9 atom % D), sodium sulfide (Na_2S, >99.99%, anhydrous), zinc chloride ($ZnCl_2$, >98%), cobalt(II) chloride hexahydrate ($CoCl_2 \bullet 6H_2O$, 98%), manganese(II) chloride ($MnCl_2$, >99%), iron(II) chloride ($FeCl_2$, 98%), iron(III) chloride ($FeCl_3$, >99.99%), chromium(II) chloride ($CrCl_2$, 95%), nickel(II) chloride ($NiCl_2$, 98%), copper(I) chloride (CuCl, >99.99%), copper(II) chloride ($CuCl_2$, 97%), sodium borohydride ($NaBH_4$, 99%), tert-butylamine (TBA, ≥99.5%), 4-aminothiophenol (4-AMT, 97%), polyvinylpyrrolidone (PVP, average M_n 55k), silver trifluoroacetate (>99.99%), titanium(IV) chloride ($TiCl_4$,

99.9%), trimethylaluminum (TMA, 97%), hydrogen peroxide solution (H_2O_2, ultratrace analysis), sodium iodide (NaI, >99%), iodine (I_2, ≥99.99%), sodium chloride (NaCl, ≥99%), acetone (≥99.5%), acetonitrile (ACN, 99.8%), maleimide (MI, 99%), 6-maleimidohexanoic acid (MCA, 90%), n-(2-hydroxyethyl)maleimide (HEMI, 97%), di(ethylene glycol) ethyl ether acrylate (DEE, ≥90%), 3-sulfopropyl acrylate potassium salt (SAC), and gold nanoparticles (30 nm, PDI<0.2, citrate buffered) were purchased from Sigma Aldrich. Hexa(ethylene glycol) monothiol (HEGMT, 98%) was purchased from BroadPharm. Tetrahydrofuran (THF, 99.9%) and ethylene glycol (EG, >99%) were purchased from Acros Organics. Oxygen (>99.993%), argon (>99.999%), and nitrogen (>99.999%) were purchased from Praxair. Fresh aqua regia was prepared by mixing hydrochloric acid (HCl, 36.5-38.0%, ACS grade, J.T.Baker) and nitric acid (HNO_3, 69.0-70.0%, ACS grade, J.T.Baker) in a molar ratio of 3:1. Nitric acid (TraceMetal grade, Fisher Scientific) was double distilled for ICP-MS. Methanol (LC-MS grade) and formic acid (90%) were purchased from J.T.Baker. mPEG-Mal350 (PEGMI350, 97%), mPEG-Mal1K (PEGMI2k, 97%), and mPEG-Mal2K (PEGMI2k, 97%) were purchased from Biochempeg. Cis-diisothiocyanato-bis(2,2'-bipyridyl-4,4'-dicarboxylato) ruthenium(II) bis(tetrabutylammonium) (N719) was purchased from SOLARONIX. Carbon monoxide (CO, 99.9%) was purchased from Matheson.

2.2 Preparation of the Nantennas Platform

2.2.1 Ag NCs Synthesis and Cleaning

The synthesis was modified from the well-known procedure published in 2007[234]. All of the glassware and stir bars that in contact with reactants needed to be washed in HCl first and completely dried. In general, 5 mL EG was first heated in a 25 mL round bottom flask at 150 °C for 1 hour to remove water. Meanwhile, the following four EG solutions were prepared: 3 mM of Na_2S (dehydrated in the lab), 3 mM of HCl, 20 mg/mL of PVP, and 282 mM of silver trifluoroacetate. While the EG was stirring, 95 μL of Na_2S solution was quickly injected with a pipette. After 2 min, 750 μL of HCl, and 1.25 mL of PVP solution were added in the same fashion. 2 min later, 400 μL of silver trifluoroacetate was finally added. The reaction was quenched in an ice bath for 2 min when the right color (Figure 2.1) showed up (usually took 15-30 min).

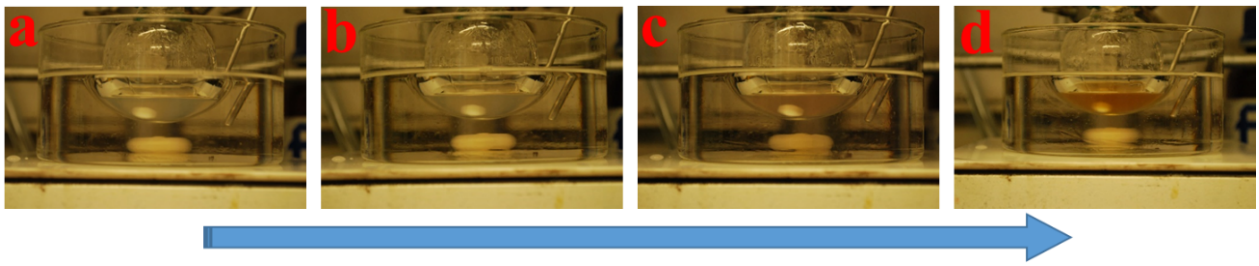

Figure 2.1 The color change of the Ag NCs synthesis over time.

There was no exact reaction time due to the extreme sensitivity of the reaction kinetics to the error in weighing. In addition, the silver trifluoroacetate is light sensitive, and Na_2S is air/moisture sensitive. Adjusting the second reaction according to the color change in the

first one is usually needed. The as-synthesized Ag NCs was transferred to a centrifuge tube (Corning Model 430921) with 50 mL of acetone followed by 4400 rpm centrifugation for 5 minutes. The supernatant was discarded then the Ag NCs were resuspended in 50 mL room temperature or 80 °C water followed by another four wash at 12000 rpm for 15 min. The as-made Ag NCs were resuspended in ethanol then stored in the fridge.

To further remove the surface PVP, Ag NCs dried on Si substrate (University Wafer ID 2654) was soaked in 5 mL of 75 μM transition metal (Zn(II), Co(II), Mn(II), Fe(II), Cr(II), Ni(II), Cu(I, II)) chloride ethanol solution for 5 minutes then cleaned with ethanol and dried. We also tried 10 to 60 seconds of UV-Ozone treatment of dried Ag NCs with our home build setup. In addition, the Si substrate loaded with as-made Ag NCs was submerged in 5 mL of $NaBH_4$/TBA ($NaBH_4$: TBA : H_2O = 0.38 mg : 4 mL : 1 mL)[235] for 30 minutes then cleaned with ethanol and dried. Similarly, the substrate was soaked in 2 mg/mL of 4-AMT aqueous solution for 24 hours to promote the exchange of PVP[236].

2.2.2 Au NCs Synthesis and Cleaning

Citrate-capped gold nanocrystals (NCs) were synthesized using a sequential injection method[237], as shown in Figure 2.2. Briefly, 1 mL of a 25 mM aqueous solution of HAuCl4•3H2O was added by pipette to 150 mL of 2.2 mM aqueous trisodium citrate dihydrate in a 250 mL round bottom flask under 1000 rpm stirring at 100 °C. The solution color changed from yellow to dark blue, then light red. After a reaction time of 15 minutes, the solution was cooled to 90°C, and 1 mL of 60 mM aqueous trisodium citrate dihydrate was injected into the flask, followed by 1 mL of a 25 mM aqueous solution of HAuCl4•3H2O two minutes later. This sequential injection of the two precursors was repeated 14 times

(at 30 minutes intervals) at 90°C to increase the NC diameter. Finally, the reaction was quenched with an ice bath, and the NC dispersion was stored without purification at 2-8°C.

Amicon® Centrifugal Filter Units (UFC905024, MWCO 50k) was used to further clean the as-made Au NCs (Figure 2.3 left). Briefly, 12 mL of Au NCs was filled to the filter device followed by 2000 rpm centrifugation for 30 minutes in a fixed angle rotor (Eppendorf Model F-34-6-38) centrifuge (Eppendorf Model 5804). Water was then added to the device to resuspend the concentrated NCs collected at the bottom of the unit. The above procedure was repeated multiple times until the desired cleanliness was reached. Note, 12 mL of 0.1 M NaOH solution was passed through the filter three times to clean the protective glycerin layer before using the device. Water was needed to keep the regenerated cellulose filter wet after using the device. Similarly, MACROSEP Advance Centrifugal Devices with MWCO 30k (MAP030C36) or 10k (MAP010C36) polyethersulfone filter from Pall Corporation was used.

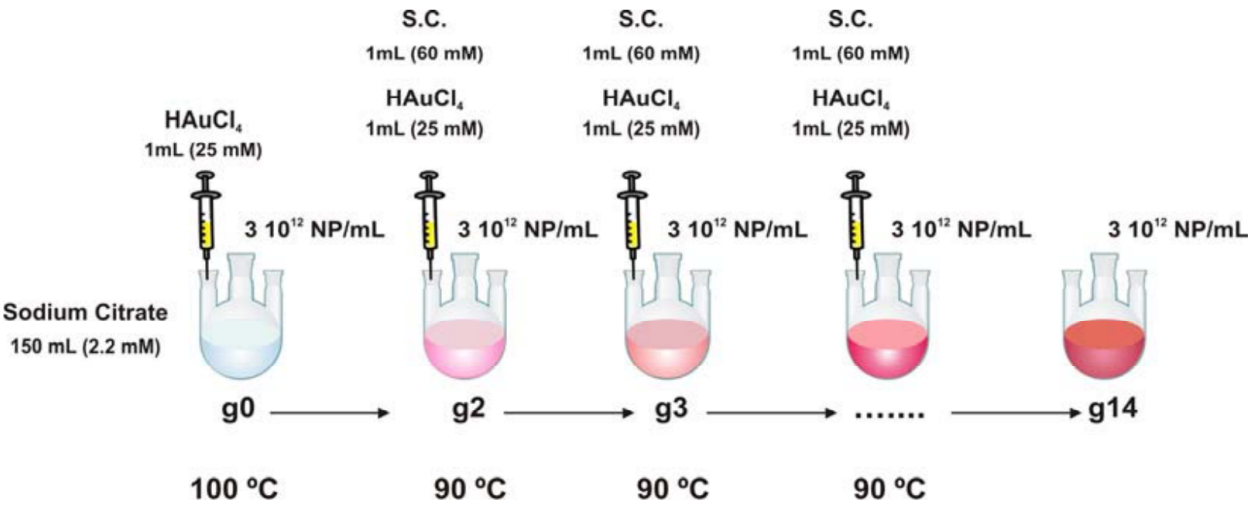

Figure 2.2 Scheme of the seeded growth of Au NPs.

Reprinted with permission from ref 237. © 2011 American Chemical Society.

Amicon® Stirred Cell (UFSC20001, 200 mL) was tested for NCs cleaning as well. The cell was first assembled by placing the regenerated cellulose membrane (Biomax® Ultrafiltration Membrane, MWCO 30k) or the customized polycarbonate membrane (Sterlitech, 0.01 Micron, 63.5 mm) into the membrane holder on the base. Then, the cell body was screwed into the base with a stir bar inserted. The cap was oriented, sealed, and locked after loading 150 mL of Au NCs solution followed by pressurizing the cell with 60 psi of Ar. 140 mL of water was added when the Au NCs solution was concentrated down to 10 mL under 350 rpm stir.

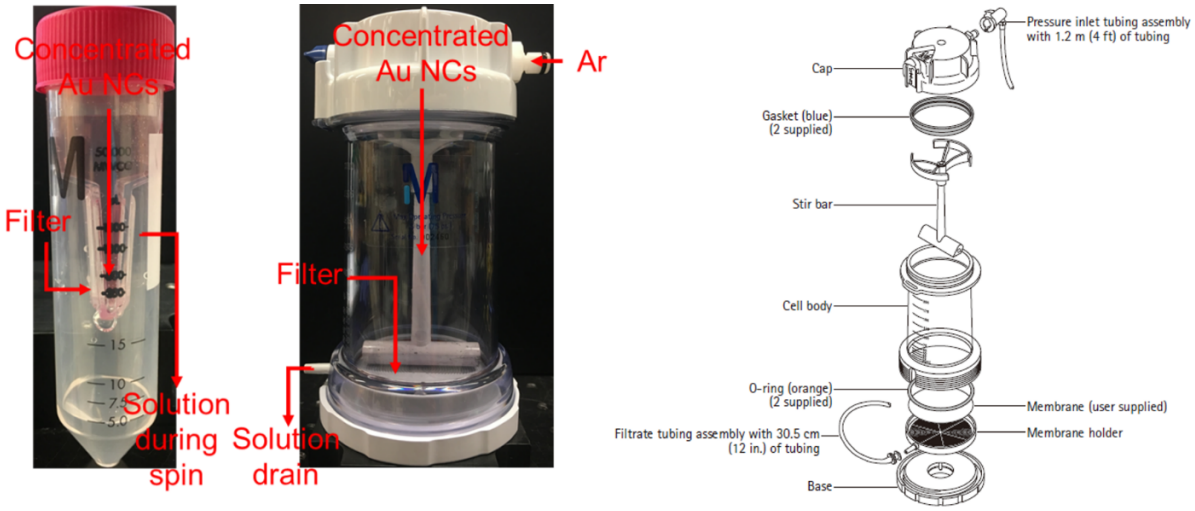

Figure 2.3 Scheme of the Amicon® Centrifugal Filter Units (left) and Stirred Cells (right).

2.2.3 Atomic Layer Deposition (ALD)

Atomic Layer Deposition (ALD) is a deposition method that allows atomic layer by atomic layer growth of materials enabled by the sequential pulsing of reactant A and B with the purging of the by-product in between as illustrated in Figure 2.4[238]. In this study, TiO_2 or Al_2O_3 were deposited on the surface of Au or Ag NCs by reacting $TiCl_4$ or TMA (reactant A) with freeze-pump-thaw degassed water (reactant B).

NCs was first dried on a lacey carbon copper grid (Ted Pella, 01824), silicon grid with silicon nitride support film (Ted Pella, 21569-10), or Si substrate. The ALD chamber was then pumped down below 80 mtorr after loading the sample on the copper plate. For one atomic layer (cycle) deposition of TiO_2 at 75 °C, $TiCl_4$ (reactant A) was pulsed (step #1) for 40 ms followed by 30 seconds purging (step #2). Then H_2O (reactant B) was pulsed (step #3) for 15 ms, followed by 30 seconds purging (step #4). The total number of cycles was determined by the thickness needed. Similarly, Al_2O_3 deposition was done with 40 ms (step #1), 20 seconds (step #2), 30 ms (step #3), and 30 seconds (step #4) at 75 °C. In general, the growth rate was ~1.1 Å/cycle.

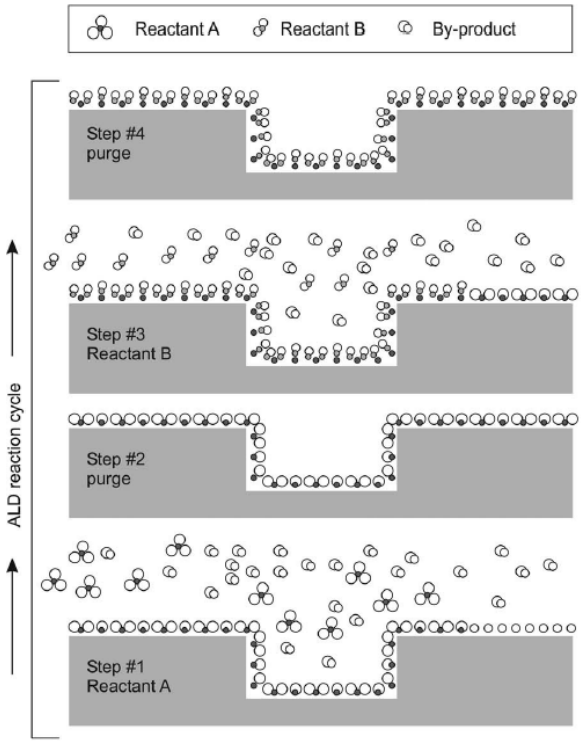

Figure 2.4 Scheme of one ALD cycle.

Reprinted from ref 238, with the permission of AIP Publishing. © 2005 American Institute of Physics.

2.2.4 Molecule Loading

2 nm of amorphous TiO_2 was grown by ALD on cleaned Ag NCs dried on a proper substrate. N719 was loaded by soaking the substrate with Ag/TiO_2 NCs in 0.5 mM of N719 ACN solution for 24 hours. Later on, the ACN cleaned Ag/TiO_2/N719 structure was protected by another 20 nm TiO_2 using ALD. The final configuration of the platform I with N719 is illustrated in Figure 2.5 (left).

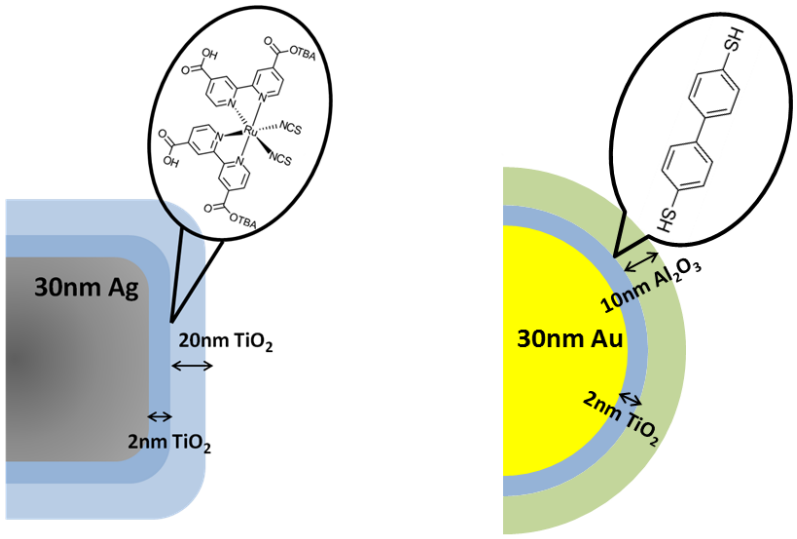

Figure 2.5 Configuration of the complete platform after molecule loading.
(left) Platform I of Ag/TiO_2/N719/TiO_2. (right) Platform II of Au/TiO_2/DBDT/Al_2O_3.

Similar to platform I, DBDT was loaded by soaking the substrate with Au/TiO_2 NCs in 5 mM of DBDT THF solution for 1 hour. 10 nm of Al_2O_3 was finally deposited via ALD after thorough cleaning of the Au/TiO_2/DBDT NCs with THF to remove residue DBDT. The final configuration of the platform II with DBDT is illustrated in Figure 2.5 (right). On the other hand, Au NCs cross-linked by HEGDT (H) was loaded with DBDT (D) by co-addition or step-

by-step method (Figure 2.6) for the Raman study at Laser Spectroscopy Labs. In the co-addition method, 0.1 mL of 10 mM HEGDT aqueous solution, 0.02 mL of 5 mM DBDT THF solution, and 1.13 mL of H_2O were added to 0.75 mL of as-made Au NCs solution. Five droplets of the above solution containing both HEGDT and DBDT were dried on Si substrate minutes later then thoroughly washed by THF and H_2O. In the step-by-step method, 0.1 mL of 10 mM HEGDT aqueous solution, and 1.15 mL of H_2O was added to 0.75 mL of as-made Au NCs solution first. Five droplets of the above solution containing only HEGDT were dried on Si substrate after 5 minutes then washed by H_2O. The substrate was socked in 5 mM of DBDT THF solution for 30 minutes, followed by THF washing. Substrates from both methods were dried under vacuum for 30 minutes.

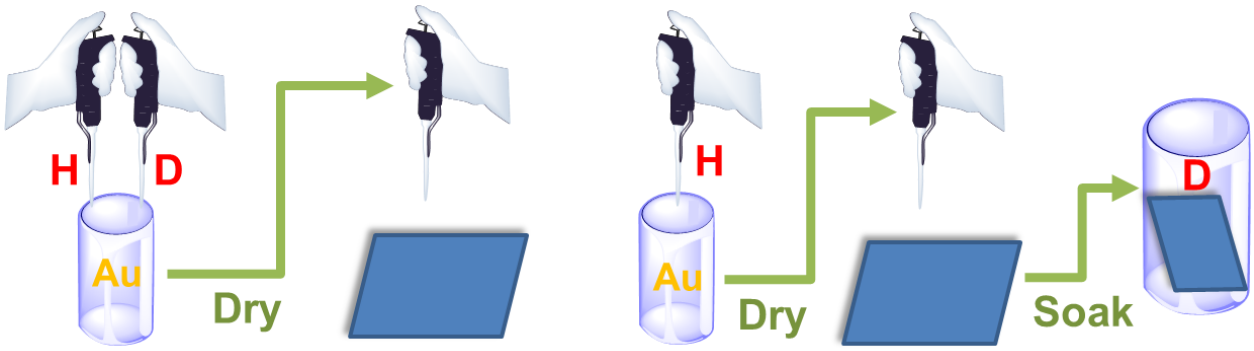

Figure 2.6 Scheme of loading DBDT on HEGDT cross-linked Au NCs.

(left) Co-addition method. (right) Step-by-step method.

2.3 Dithiol-mediated Aggregation

2.3.1 Alkane Dithiols

In a glass vial at room temperature, 1 mM of 1,3-propanedithiol (Pro), 1,4-butanedithiol (But), 1,5-pentanedithiol (Pen), and 1,6-hexanedithiol (Hex) ethanol stock solution were prepared and stored inside the N_2 glovebox to avoid disulfide formation. 150 μL of 1 mM alkane dithiol ethanol solution, 300 μL of Ag NCs ethanol solution, and 1050 μL of ethanol were mixed to initiate the aggregation (final [dithiol] = 100 μM). On the other hand, alkane dithiols were diluted with ethanol first to 1 mL at a concentration of 1000 μM, 200 μM, and 40 μM. Then the above 1 mL stock solution was added to 1 mL of commercial Au NCs aqueous solution from Sigma Aldrich.

2.3.2 Hexa(ethylene glycol) Dithiol and Other Dithiols

In a glass vial at room temperature, 1 mL of the as-made Au NCs suspension was diluted with 0-999 μL of water. Then, 1-1000 μL of a 10 mM aqueous solution of HEGDT was added to the vial to yield a total volume of 2 mL. Final [HEGDT]/[NC] ratios were 2,000 to 2,000,000. Similarly, 10 mM aqueous solution of 2,2'-(ethylenedioxy)diethanethiol (EDD), pentaerythritol tetrakis(3-mercaptopropionate) (PTM), or 10 mM ethanol solution of 1,6-hexanedithiol (Hex) were added to as-made Au NCs solution with final [thiol]/[NC] = 4,000.

To achieve [HEGDT]/[NC] < 2,000, regular 10 mM HEGDT stock solution was first diluted 100 times to make a 100 μM stock solution. Then, the 100 μM stock solution was further diluted to 10, 8, 6, 4, 2, 1 μM respectively. Finally, 1 mL of the diluted solution was added to

1 mL of as-made Au NCs. This method avoided using a small volume in each step, which gave much better control of the final [HEGDT].

2.4 Redispersion and Termination of the Aggregation

2.4.1 Ozone-mediated Redispersion

To redisperse the aggregated/precipitated NCs, the output of an ozone generator (Enaly Model 5000BF) fed with oxygen gas was bubbled at 0.2 L/min into an open glass vial with aggregated/precipitated NCs for 5 minutes under sonication (Branson Model 1510) at room temperature (unless otherwise noted). Steady-state ozone concentrations in the gas stream and solution were estimated to be at least 1 mM and 350 μM, respectively. The vial was then sparged with argon at 0.2 L/min for 1 minute to remove the residual ozone, capped, and stored in ambient light at room temperature (unless otherwise noted). Since ozonation of high concentrations of HEGDT (i.e., [HEGDT]/[NC] ≥ 1,000,000) lowers the pH enough to dissolve the NCs, 10 μL (20 μL) of a 1 M aqueous solution of NaOH was added to samples with [HEGDT]/[NC] = 1,000,000 (2,000,000) to adjust the pH to ~12 before ozonation.

2.4.2 Monothiol-mediated Redispersion

To attempt redispersion of the precipitated NCs by thiol self-exchange, a large excess of a monothiol ([monothiol]/[NC] = 4,000,000) was added to the supernatant of hard-crashed NC precipitates prepared as described above (using [HEGDT]/[NC] = 4,000). Monothiol additions were 200 μL of 100 mM of HEGMT in water, MPA in water, MUDA in ethanol, or

MHDA in ethanol. After adding the monothiol, the vial was tightly sealed and gently shaken for 1 minute, then stored for seven days at room temperature or sonicated for 12 hours at 75 °C. MHDA and MUDA formed emulsions in water, so these samples were passed through 0.2 μm PTFE syringe filters (28145-495, VWR) prior to acquiring optical extinction spectrum.

2.4.3 Monothiol-mediated Disulfurization

3-mercaptopropionic acid (MPA), 1-thioglycerol (TG), thioglycolic acid, (TGA), and 2-mercaptoethanol (ME) aqueous solution were chosen to react with HEGDT forming disulfide under NaI/H_2O_2 or I_2 catalyzing to terminate the aggregation process. First, 0.1 mL of 10 mM HEGDT aqueous solution was mixed with 1 mL of as-made Au NCs diluted by 699 μL of H_2O. Immediately, 0.1 mL of 10 mM monothiol, 1 μL of 10 mM NaI, and 0.1 mL of 10 mM H_2O_2 were added to the above solution. Similarly, 10 μL of 1 mM I_2 aqueous solution can be added instead of NaI/H_2O_2 mixture. The final ratio of reactant are [HEGDT] : [monothiol] : [NaI] : [H_2O_2] = 1 : 1 : 0.01 : 1 or [HEGDT] : [monothiol] : [I_2] = 1 : 1 : 0.01[239]. The effect of individual components (monothiol or catalyst) on the HEGDT mediated Au NCs aggregation reaction was studied as well following the ratio above. The total volume of the solution in the vial was 2 mL throughout the study by varying H_2O volume.

2.4.4 Thiol-ene Click Reaction

20 mM of aqueous stock solution of six types of maleimides (MI, MCA, HEMI, PEGMI350, PEGMI1k, PEGMI2k) and two types of acrylates (DEE, SAC) were made first and stored in the fridge. “X” is used to represent certain maleimides or acrylates in the following text. The

total volume of the solution was 2 mL adjusted by adding H_2O ([HEGDT] = 10 μM, pH = 6-7). The vial was kept at room temperature under normal room light. These conditions applied to all experiments during the study unless otherwise noted. The pH of the MCA stock solution was pre-adjusted to 6-7 to keep reaction condition consistent. First, the control experiments to test the compatibility of X with Au NCs solution were done by adding 1 mL of the above 10 mM stock solution to 1 mL of as-made Au NCs (without HEGDT). Next, three methods of mixing were employed to gain a comprehensive understanding of the click reaction between X and HEGDT in Au NCs solution. Method A mixed the diluted Au NCs solution with HEGDT first then X was added after 10 seconds. Method B mixed the diluted Au NCs solution with X first then HEGDT was added after 1 minute. Method C mixed X and HEGDT first then the diluted Au NCs solution was added after one day. In total, 480 experiments were designed to test eight types of X using three methods at four different [NC] (50%, 40%, 30%, and 20% of the as-made Au NCs) with five different [X] (10 μM, 20 μM, 200 μM, 2 mM, and 10 mM).

It was time-consuming to track the extinction spectrum at each condition. Thus, the following qualitative method which determined the effect of click reaction on the aggregation rate by comparing the color change of the (X + HEGDT + Au NCs) solution with a reference solution (HEGDT + Au NCs) after 30 minutes of the reaction was employed. Figure 2.7 provides an example. The red color was used to represent the reaction (top row, X + HEGDT + Au) that went faster than the reference (middle row, HEGDT + Au NCs). On the other hand, the blue color represented reaction that went slower (bottom row). Finally, the color was tabulated into Table 3 by different reaction conditions.

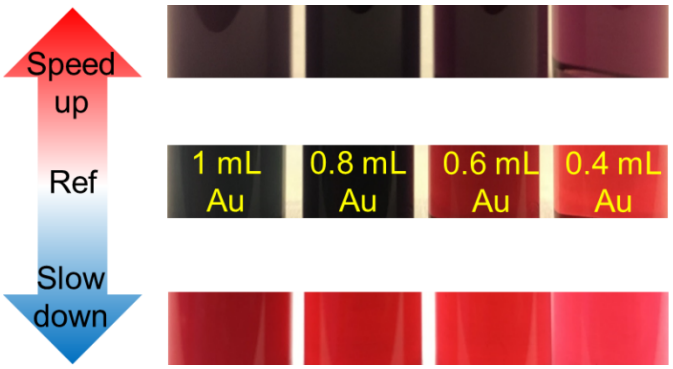

Figure 2.7 Example of the method used to track click reaction in Au NCs solution.

2.5 Morphological and Elemental Characterization

2.5.1 Scanning Electron Microscopy (SEM)

Scanning electron microscopy (SEM) was performed on FEI Magellan 400 XHR SEM or TESCAN GAIA-3 XMH operating at 10 keV and 50 pA. SEM samples were prepared by pipetting droplets of NC suspension onto lacey carbon copper grid (Ted Pella, 01824), silicon grid with silicon nitride support film (Ted Pella, 21569-10) or Si substrate, respectively. After 10 seconds, the droplet was blown off the grid/substrate with a stream of argon to avoid the artificial formation of NC clusters during slow drying. ALD of TiO_2 or Al_2O_3, as well as molecule loading, was performed directly on the TEM grid or Si substrate with NCs. Besides, Au NCs coated filamentous fungus was filtered and washed on filter paper (Whatman, 1001-125) with H_2O then dried under vacuum. The filter paper loaded with the fungus was then cut and clipped on the PELCO low profile SEMClip™ (Ted Pella, 16111-55) for imaging.

2.5.2 Transmission Electron Microscopy (TEM)

Conventional transmission electron microscopy (TEM) imaging was performed on JEOL 2800 or JEOL JEM-2100F at 200 keV, JEM-ARM300F at 300 or 80 keV with Gatan TEM Analytical Holders using Gatan GIF Quantum detector. Gatan Cooling In-Situ Holder (cooling-EM) was also used to image NCs at -170 °C monitored by Gatan Cold Stage Controller (SmartSet Model 900) to minimize beam induced particle merging. The sample preparation for regular and cooling-EM was similar to SEM except for Cryogenic Electron Microscopy (cryo-EM). Briefly, Quantifoil® TEM grid (Ted Pella, 657-200-CU) was first glow discharged in Low Vacuum Coater (Leica, EM ACE200) for 30 seconds to improve wetting. The grid was then quickly transferred to Automatic Plunge Freezer (Leica, EM GP) followed by injecting 3 μL of Au NCs aqueous solution. After blotting extra solution with filter paper (Whatman, 1001-125), the grid was inserted into liquid nitrogen cooled liquid propane (Bernzomatic). Finally, the sample was transferred to Gatan Cryo-Transfer Holder under liquid nitrogen. Low dose mode which separating the area being recoded and focused was used for cryo-EM imaging. The grid was retrieved after warming up the Cooling or Cryo holder in Turbo Pumping Station (Gatan Model 655). In general, small aperture, large spot size, and spread beam were preferred during imaging to reduce beam effect further.

2.5.3 Scanning Transmission Electron Microscopy (STEM)

Scanning transmission electron microscopy (STEM) dark field (DF), bright field (BF), and secondary electron (SE) imaging was performed on JEOL 2800 at 200 keV, and JEM-ARM300F at 300 or 80 keV with Gatan TEM Analytical Holders using Gatan or JEOL DF/BF/SE detector. Cooling or Cryo STEM were performed following the same sample

preparation procedure as TEM. All sample holders were cleaned by O_2/Ar plasma in the Advanced Plasma System (Gatan, Model 950) to remove hydrocarbon contaminants before loading sample grid.

2.5.4 Energy-Dispersive X-ray Spectroscopy (EDS)

Energy-dispersive X-ray spectroscopy (EDS) elemental mapping was done after STEM imaging on JEOL 2800 at 200 keV with dual large angle Silicon Drift Detectors (SDD). Spectrum fitting and mapping were performed using Pathfinder X-ray Microanalysis Software (Thermo Scientific). For sample preparation, Al_2O_3 was deposited on Au NCs via ALD directly on the silicon grid with silicon nitride support film.

2.5.5 Electron Energy Loss Spectroscopy (EELS)

Electron energy loss spectroscopy (EELS) elemental mapping and its corresponding high-angle annular dark-field imaging (HAADF) were done on FEI Image Corrected Titan3™ G2 60-300 S/TEM. Spectrum fitting and mapping were performed using Gatan Microscopy Suite® (GMS) software. Cleaned Ag NCs were dried on lacey carbon copper grid then shipped air free (Kurt J. Lesker, FN-0275S) to Nanjing University, China for EELS.

2.5.6 X-ray Photoelectron Spectroscopy (XPS)

X-ray photoelectron spectroscopy (XPS) data of the S 2p and Au 4f regions were acquired with a Kratos AXIS Supra spectrometer using monochromatic Al Kα radiation at an X-ray power of 225 W and 40 eV pass energy (5 sweeps, 0.05 eV step size, and 500 ms dwell time). Samples were prepared by drop casting NCs onto O_2 plasma-cleaned Si substrates

(Zepto, Diener Electronics), rinsing thoroughly with water, and drying under a stream of nitrogen. All spectrum were charge corrected using the Au 4f 7/2 peak at 84.0 eV. The S 2p region was fitted using CasaXPS (Casa Software Ltd) software with spin-orbit doublets at an intensity ratio of 2:1 (2p 3/2 : 2p 1/2), a binding energy difference of 1.2 eV, a single peak width, and Shirley background subtraction[240,241].

2.5.7 Ion Scattering Spectroscopy (ISS)

Ion scattering spectroscopy (ISS) was acquired after XPS on Kratos AXIS Supra using positive He ion beam. Surface atoms of the Ag NCs were probed according to the energy loss of the He ion due to the elastic collision. We identified C, O, Na, Cl, and Ag on the surface.

2.5.8 Inductively Coupled Plasma Mass Spectrometry (ICP-MS)

The Au NC concentration was determined by inductively coupled plasma mass spectrometry (ICP-MS). Known volumes of Au NC suspension were added to fresh aqua regia, diluted with double-distilled nitric acid as needed, and immediately measured on a Nu AttoM ES HR-ICP-MS spectrometer using the low-resolution peak jump method with 15 cycles of 500 sweeps and 500 μs dwells per peak. A noble metals standard (VHG Labs SM40-100) was used to construct a calibration curve, and an internal standard (VHG Labs LIS3-100) was used to correct for drift and matrix-related artifacts. Based on the measured Au concentration of 0.41 mg/L and the known size of the NCs (from TEM images), we find [NC] = 4.99 nM in the as-made Au NC suspension. Control experiments performed on the supernatant of centrifuged NC suspensions showed that the dissolved Au concentration

was below the ICP-MS detection limit, meaning that effectively all of the Au atoms are contained in the NCs, with negligible unreacted Au precursor in these samples.

2.6 Optical and Molecular Characterization

2.6.1 Ultraviolet-visible Spectroscopy (UV-Vis)

Optical extinction spectrum (λ = 400-800 nm) were acquired in quartz cuvettes (Spectrocell Model R-4010) on a PerkinElmer Lambda 950 spectrophotometer. The concentration of dissolved ozone was quantified using the X^1A_1 to $^1B_2$ transition at 260 nm (ε = 2992 M^{-1} cm^{-1})[242]. Reference beam attenuation was used in the UV-Vis to ensure the high absorbance (4-5) peak around 525 nm was measured accurately. This method sacrifices the accuracy and increases the noise level at the low absorbance (<0.5) area. Control experiments showed that the reference beam attenuation method did not change the spectrum shape or main figures. It only altered the noise level.

2.6.2 Fourier-transform Infrared Spectroscopy (FTIR)

Attenuated total reflectance (ATR) FTIR spectrum was acquired with a Nicolet 6700 FTIR spectrometer equipped with a GladiATR diamond ATR module (Pike Technologies) using 128 scans at a resolution of 4 cm^{-1}. Samples were prepared by centrifuging as-made Au NC suspensions, discarding the supernatant, cleaning the NCs four times in ethanol to remove free citrate and other species present in the reaction solution, and drying a droplet of the purified Au NC suspension on the ATR crystal (Figure 2.8). In situ HEGDT or citrate treatments were performed by flooding samples on the ATR crystal with 1 mL of 10 mM

aqueous HEGDT or 1 M aqueous trisodium citrate for 1 hour, wicking away the liquid, flooding with 1 mL of water for 30 minutes, and finally wicking away the water and drying the sample in a stream of nitrogen.

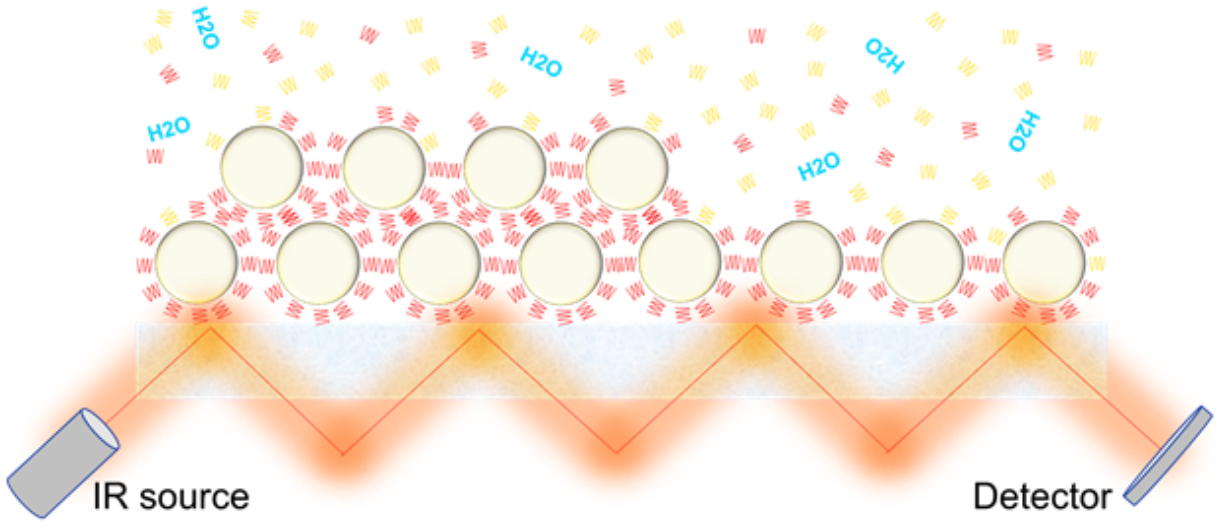

Figure 2.8 Scheme of HEGDT (yellow) replaces surface trisodium citrate (red) on ATR. The light coming from the IR source bounces multiple times at the interface between the diamond crystal and Au NCs. Evanescent wave extended into the Au NCs carries the information of molecular vibrational states to the detector.

2.6.3 Raman spectroscopy

Raman spectrum of $Ag/TiO_2/N719/TiO_2$ (platform I) was acquired in a backscattering geometry with 532 nm CW diode laser excitation (~70 $\mu W/\mu m^2$), 5-10 s exposure, and 5-10 accumulations. The sample was first imaged under SEM to determine the position of dimers, trimers, and clusters then overlapped with the map (left, Figure 2.9) captured under an inverted optical microscope (Olympus Model IX71, NA = 0.65) using backscattered light. The backscattered SERS signal was first separated from the Rayleigh

light with notch filters (Semrock, 1 : 106 extinction ratio) then dispersed and acquired on a CCD camera (Andor Model V401-BV)[243].

Raman spectrum of pure HEGDT, DBDT, and HEGDT cross-linked Au NCs were acquired on Renishaw inVia™ Confocal Raman Microscope with 532 nm continuous waveform (CW) excitation (10% power), 10 exposure per second, and 5 accumulations. Samples were prepared by drop casting HEGDT- or DBDT-treated NCs onto plasma-cleaned Si substrates, followed by rinsing with copious water or THF, respectively, and drying in a stream of nitrogen. Reference films of HEGDT and DBDT were prepared by drop casting 10 mM of HEGDT or 5 mM of DBDT solutions in water and THF, respectively.

During both Raman experiments, only signals from the substrates (Si_3N_4 or Si) was identified (no molecular lines) if the laser was moved away from the NCs.

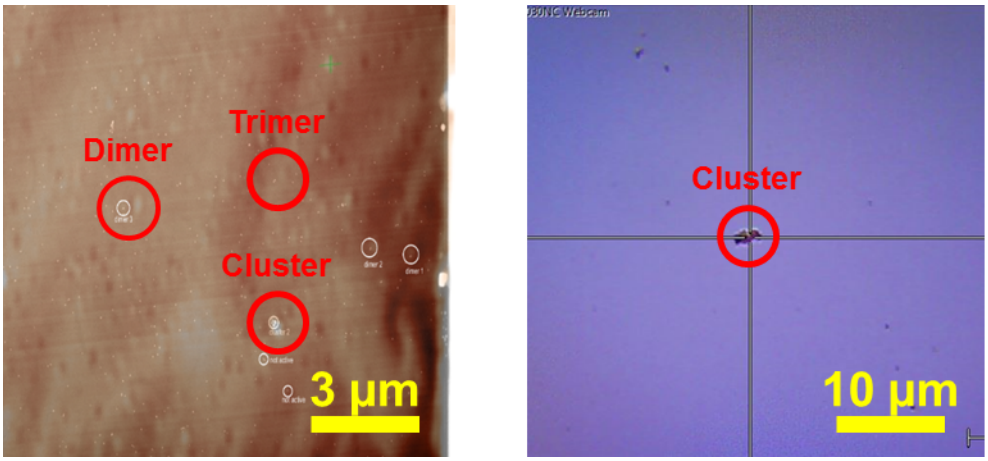

Figure 2.9 Photo of NC assembly under optical microscopes.

(left) Overlapping SEM image and backscattered light map of dimer, trimer, and cluster of Ag/TiO_2/719/TiO_2 on Si_3N_4 support film. (right) Bright field image of Au/HEGDT/DBDT cluster on Si substrate.

2.6.4 Nuclear Magnetic Resonance Spectroscopy (NMR)

^{1}H NMR data were collected in pure D_2O or a 1:1 H_2O/D_2O mixture in precision NMR tubes (Wilmad Model 528-PP-7) using a Bruker DRX500 spectrometer (500 MHz, BBO probe) with 16 scans at a delay time of 20 seconds. The absolute concentration of citrate was determined with an internal reference (DSS sodium salt). The pulsed field gradient technique was used to suppress the H_2O signal. NMR peak position was predicted using ChemDraw software from PerkinElmer. Peak position calibration, background subtraction, and phase correction were done using Mnova software from Mestrelab Research.

2.6.5 Mass Spectroscopy (MS)

Mass spectrometry data were acquired on a Waters LCT Premier TOF mass spectrometer using electrospray ionization and an MCP detector operating in positive ion mode. The 10 mM of HEGDT or HEGDS aqueous solution was diluted to 10 μM with methanol before injection. PEG served as the internal reference.

2.7 Particle Size and Surface Charge Analysis

2.7.1 Dynamic light scattering (DLS)

Dynamic light scattering (DLS) was performed on Malvern Zetasizer Nano to monitor the hydrodynamic diameter of Au NCs change over time after adding HEGDT. Similar to UV-Vis experiment, 10 uL of 10 mM HEGDT was added to diluted 10 nm Au NCs aqueous solution in a disposable cuvette (BRAND, 759071D). Measurement was done every 5 minutes with 10 runs (10 seconds per run) in the Zetasizer. The sample was taken out and gently shaken

immediately after the acquisition to ensure room temperature, and room light condition was maintained.

2.7.2 Nanoparticle Tracking Analysis (NTA)

Nanoparticle tracking analysis (NTA) was used as a complementary technique to verify the [NC] calculated using ICP-MS. As-made Au NCs solution was diluted 1,000 times and injected at 1 mL per 30 seconds flow rate into Malvern NanoSight NS300. Videos of NCs undergoing Browne motion and aggregation were captured for 60 seconds and automatically processed in the NTA software.

2.7.3 Small-angle X-ray Scattering (SAXS)

Solution small-angle X-ray scattering (SAXS) measurements of as-made and ozone-redispersed Au NC suspensions were performed at Beamline 7.3.3 of the Advanced Light Source (ALS) at Lawrence Berkeley National Laboratory using monochromatic X-rays (λ = 1.24 Å, 10 keV) with an energy bandwidth of 1%. Samples were measured in transmission geometry in 1 mm diameter quartz capillaries (Hampton Research). 2D SAXS patterns were collected on a Dectris Pilatus 2M detector at a sample-detector distance of 3504.75 mm as calibrated by a silver behenate standard in a quartz capillary. Signal was collected for 120 s. The Nika software package[244] in Igor Pro was used to integrate azimuthally (25-75°) the SAXS patterns. Particle size distribution fitting was performed with the IPG/TNNLS fitting routine in Irena assuming a spherical NC shape. Several measurements were conducted across the length of the capillary to verify sample uniformity.

2.7.4 pH Measurement

pH measurements were made on stirred samples every 3 seconds using a calibrated pH meter (Oakton Model PC2700) at room temperature. Buffer solutions of pH 7.00, 4.01, and 10.01 from Oakton were used for calibration. Data were acquired after the pH reading stable for more than 2 minutes.

2.7.5 Zeta Potential Measurement

Zeta potential and mobility of as made, cleaned, HEGDT cross-linked, and ozone redispersed Au NCs were measured in Malvern Zetasizer Nano. A special cuvette DTS1070 (Malvern) with electrode was flushed with ethanol then H_2O before filling the sample.

2.8 Finite-difference Time-domain (FDTD) simulations

The FDTD simulations were done using commercial software (Lumerical FDTD solutions). The total-field scattered field (TFSF) source was employed in the simulations of all the dimers, and the plane wave was injected from the top of the dimer. Inside FDTD software the gold dielectric constants were interpolated from Johnson and Christy[245].

Two detectors were used to detect scattered and absorbed light, one detector was placed outside the TFSF source to measure the scattering cross sections, and another placed inside the TFSF source to measure the absorption cross section. A perfectly matched layer (PML) was used as the boundaries to absorb the scattered light and reduce the probable interference with the reflected light off the boundaries.

3 ALD-Functionalized Plasmonic Nantennas

In this chapter, our effort to build platforms consist of plasmonic core-shell (metal-semiconductor) nantennas using colloidal synthesis and atomic layer deposition (ALD) is summarized. Platform I of Ag/TiO_2/N719/TiO_2 and platform II of Au/TiO_2/DBDT/Al_2O_3 were constructed by stochastic assemble and ALD. We verified the precise geometry and Raman activity of these structures using SEM/TEM and spectrometers, respectively. Our initial attempt to control the nantennas assemble via alkane dithiol is discussed as well.

3.1 Platform I - Ag/TiO_2/N719/TiO_2

3.1.1 Stochastic Assembly of Ag NCs

The synthesis[234] involving silver trifluoroacetate (Ag source), PVP (capping reagent), and HCl (etching reagent) yielded Ag NCs with an average diameter of 35 nm. The transparent yellow suspension (Figure 3.1 a) of Ag NCs washed and redispersed in ethanol was used for the following study. The extinction spectrum of the as-made Ag NCs (Figure 3.1 b) shows a distinct LSPR peak at 440.2 nm and two small shoulders at 350.0 and 378.2 nm, which agrees well with literature[246,247]. The small shoulders originate from the truncated cube, which enables two extra dipole resonance[246]. Drop casting the Ag NCs solution on the TEM grid or Si substrate resulted in the stochastic formation of dimers (Figure 3.1 d) with an undefined gap distance. 2 nm TiO_2 layer was then constructed via atomic layer deposition (ALD) followed by N719 sensitizing. We did not observe significant shape or size change in the TEM images (Figure 3.1 e) after any step of the process. Finally, 20 nm of TiO_2 (Figure

3.1 f) was coated via ALD to act as a heat sink and protect the structure from melting under laser illumination. The Ag NCs can be stochastically assembled and functionalized despite the presence of residue PVP capping layer. ALD of other oxides such as Al_2O_3 or sensitizing with other molecules such as DBDT following the above procedure were also successful done. The thickness of the oxide layer can be tuned easily by varying the number of ALD cycle comparing to the solution process[248].

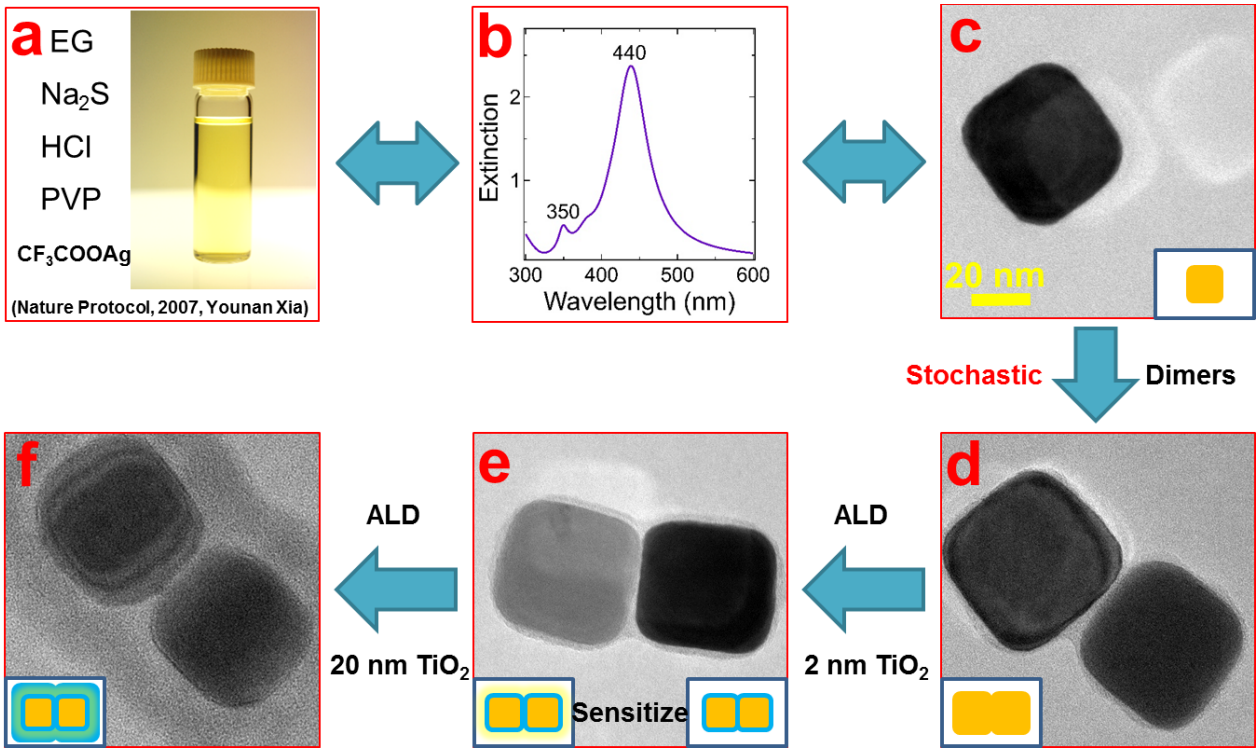

Figure 3.1 Procedure for assembling platform I - Ag/TiO_2/N719/TiO_2.

(a) The recipe[234] and photo of as-made Ag NCs ethanol solution. (b) Extinction spectrum and (c) TEM image of as-made Ag NCs. (d) Stochastically formed dimer by drying Ag NCs solution on a TEM grid. (e) Dimer after ALD of 2 nm TiO_2. (f) Dimer after sensitizing with N719 and ALD of 20 nm TiO_2.

3.1.2 Alkane Dithiol-mediated Assembly of Ag NCs

Dithiols have been widely used to link the plasmonic NCs for SERS study[249,250]. The simplest short chain alkane dithiols, including 1,3-propanedithiol (Pro), 1,4-butanedithiol (But), 1,5-pentanedithiol (Pen), and 1,6-hexanedithiol (Hex) were first selected to assemble the Ag NCs in our study. The assembling process was monitored using the extinction spectrum and scanning electron microscopy (SEM). Upon addition of alkane dithiol longer than three carbon chain, the main plasmon peak around 440 nm immediately decreased (Figure 3.2 b-d). Meanwhile, a broad shoulder started to rise at around 650 nm due to the development of new plasmon modes. The decrease in the main peak gradually slowed down in 60 minutes with the shoulder redshifted. SEM (Figure 3.2 b'-d') images show the Ag NCs fall entirely out of the solution and form large aggregates containing hundreds to thousands of NC monomer.

On the contrary, the spectrum of the shortest 1,3-propanedithiol treated Ag NCs does not show the significant change (Figure 3.2 a) in 60 minutes, which indicates the NCs are still well dispersed in the ethanol solution. Meanwhile, we only find monomers, dimers, and small clusters (less than 10 NCs together) in the SEM image (Figure 3.2 a') of sample made by drying the reaction solution after 60 minutes. The effective assemble of NCs using long chain alkane dithiol agrees with literature[251] while the unexpected result from the short chain dithiol indicates the length of the linker plays a vital role in the process. Later on, we attribute the length dependency to the surface capping reagent PVP. The simple alkane dithiols did not alter the shape or size of the Ag NCs while linking them together. The compatibility of alkane dithiols with Ag NCs make it a good candidate for the future study of controlled assembly.

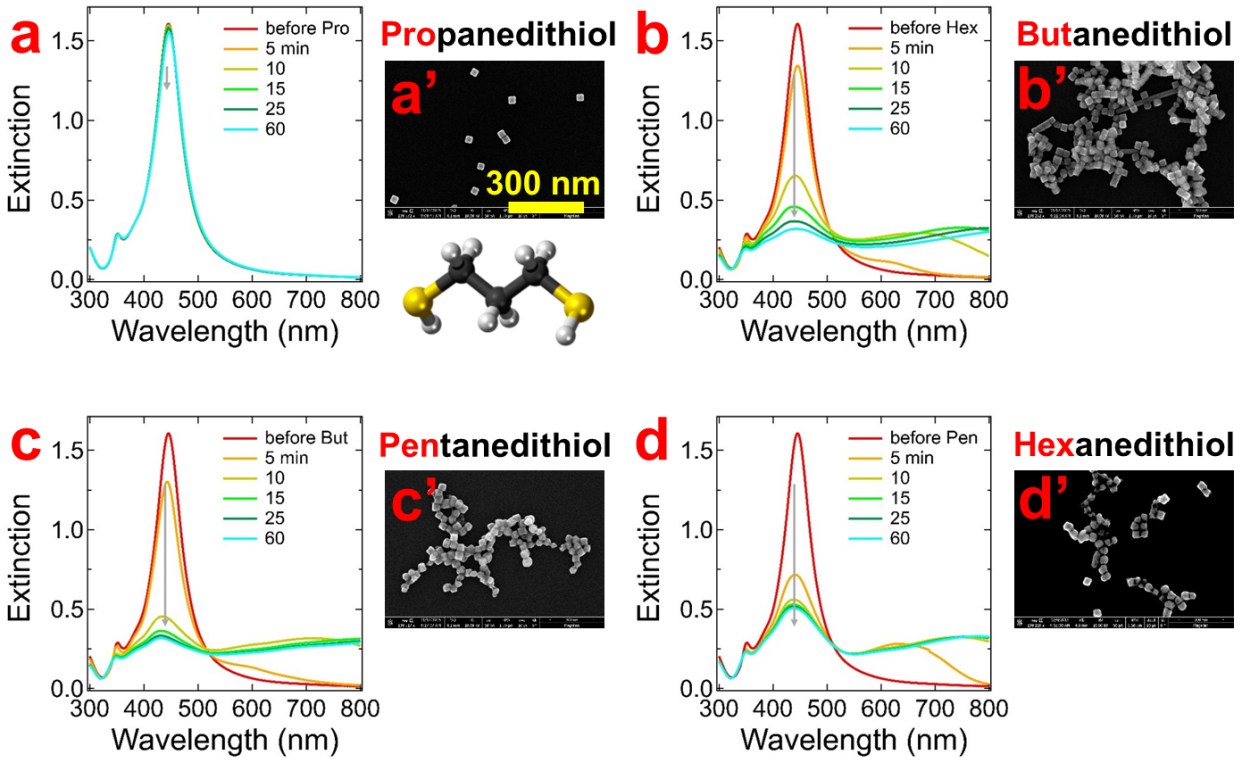

Figure 3.2 Alkane dithiol-mediated assembly of Ag NCs.

(a-d) Time series of optical extinction spectrum after adding alkane dithiol ethanol solution to the Ag NCs ethanol solution. (a'-d') Corresponding SEM images of the Ag NCs after alkane dithiol treatment. The molecular structure of 1,3-propanedithiolis is shown under (a').

3.1.3 Raman Activity of Platform I

We then compared the Raman activity of Platform I (made by stochastic assemble) with the bulk N719 using our home build spectrometer setup. The peak positions of bulk N719 in Figure 3.3 a agree with literature well[248,252,253]. Briefly, the three strongest resonance at 1473, 1540, and 1606 cm^{-1} are attributed to the C=N and C=C stretching on the bipyridine rings. In comparison, the two most intense peaks from N719 loaded on Ag/TiO_2 shifts to higher wave number, which may indicate the interaction between the excited N719 and

TiO_2. At relatively low excitation intensity (25 μW/μm^2), molecules experience the field intense enough such that the molecular signal losses within a few minutes (Figure 3.3 b) even with the 20 nm TiO_2 overcoating protection. The signal decay may cause by thermal induced changes to the nantenna structure, migration of the dye molecules out of the hot spot over the course of the experiment, or plasmon-driven decomposition of the dye molecules by the intense electric local field or high local temperature.

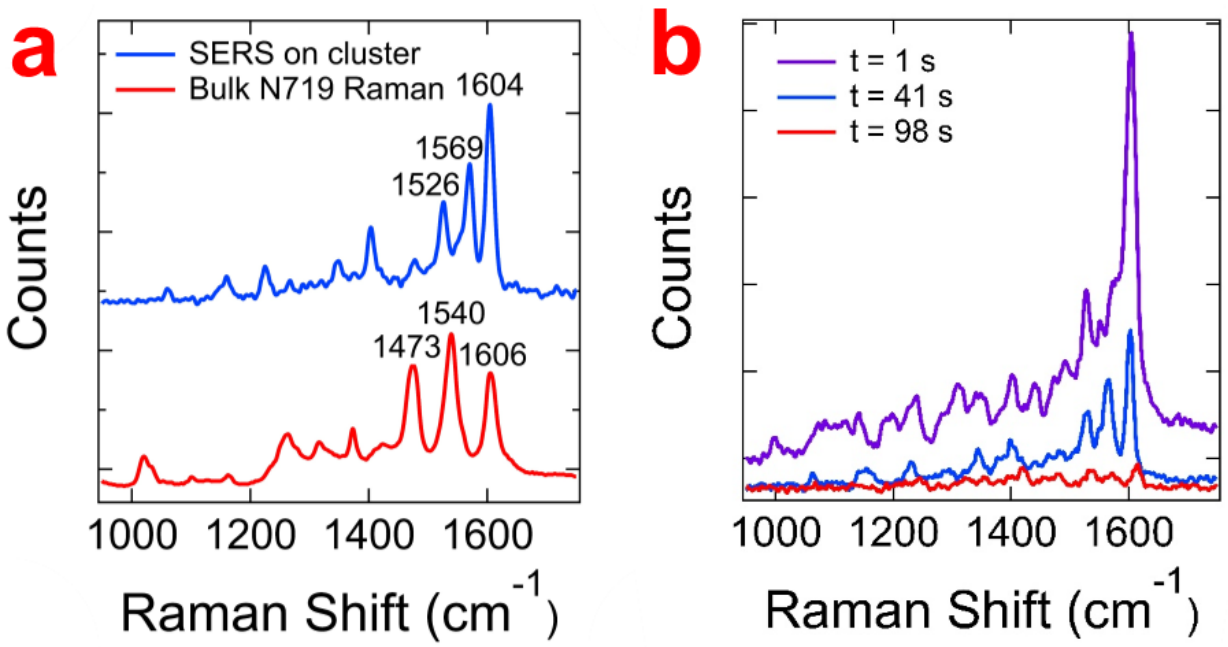

Figure 3.3 Raman spectrum of platform I cluster.

(a) Comparison of Raman response of bulk N719 and SERS response of Ag/TiO_2/N719/TiO_2. (b) Change of SERS signal of Ag/TiO_2/N719/TiO_2 over time.

3.1.4 Surface PVP Removal

Upon carefully checking the surface of the thoroughly washed Ag NCs via high-resolution TEM, we identified a 2-5 nm capping layer (Figure 3.4 a). This thin overcoat could explain why only long alkane dithiols cross-link Ag NCs effectively. Furthermore, it may prevent the direct attaching of the interesting molecules onto the Ag surface. Thus, we need to identify then remove this unwanted layer.

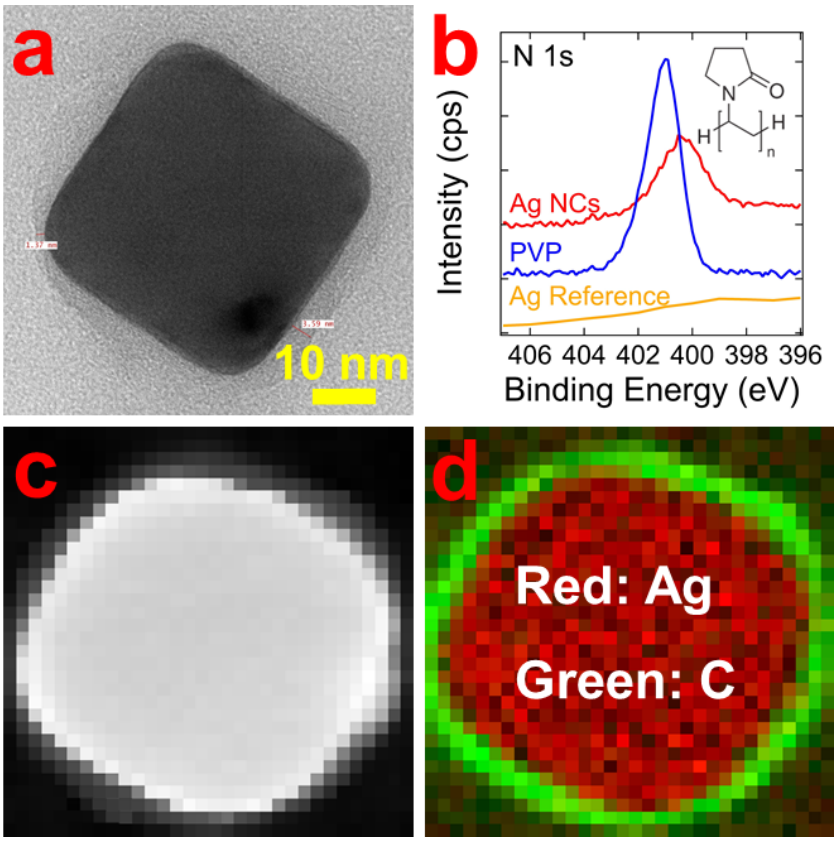

Figure 3.4 Identify the surface capping PVP layer on Ag NCs.

(a) The TEM image of the ~2 nm capping layer around Ag NCs after extensive washing. (b) Comparison of the N 1s region of the Ag NCs, PVP powder, and clean Ag thin film in XPS. (c) HADDF image and (d) EELS mapping of the same Ag NC show a Ag core with C rich shell.

The x-ray photoelectron spectroscopy (XPS) of high concentration Ag NCs dried on Si substrate shows an extra peak at 400.8 eV comparing to the pure Ag reference (Figure 3.4 b). This peak is close to the N 1s peak at 401.3 eV of the pure PVP powder sample. The slightly right shift of the peak might be due to the metal-ligand interaction. High-resolution electron energy loss spectroscopy (EELS) mapping (Figure 3.4 d) further reveals that the capping layer is carbon rich. Combining the evidence from XPS and EELS, we conclude that the PVP presents on the surface of Ag NCs.

Transition metal ions have shown a strong affinity to PVP to form small polymer-metal complexes[254] thus have the potential to "unzip" PVP from the Ag surface. We then evaluated the effect of high concentration transition metal chloride (Zn(II), Co(II), Mn(II), Fe(II), Cr(II), Ni(II), Cu(I, II)) ethanol solution treatment on the surface PVP. A series of SEM images in Figure 3.5 a show that Mn(II), Fe(II), Cr(II), Ni(II), and Cu(I, II) ions etch the Ag cubes in different degrees. This might occur due to the simple redox reaction between Ag^0 and metal cation based on the positive cell potential[255]. On the contrary, The cube structure maintained after Zn(II) and Co(II) treatment while the PVP layer was still existing upon checking the high-resolution TEM images. UV-Ozone treatment has been proved to be useful to remove the PVP layer on palladium nanocubes[256]. However, it significantly altered the shape of the Ag nanocubes immediately upon exposure (Figure 3.5 c). Other methods reported in the literature such as $NaBH_4$/tert-butylamine[257], or 4-aminothiophenol[258] treatment were tried, yet no successful removal of PVP has been found. The most promising way is the simple hot water washing of NCs at 80 °C (increase the solubility of PVP) on the filter paper. Upon intensive washing with at least 500 mL of water, the thickness of the PVP layer on some of the cubes was reduced down to 0.5 nm (Figure 3.5 b).

The stubborn residue PVP layer and low chemical resistance of the Ag NCs drive us to move on cleaner and robust Au NCs later on.

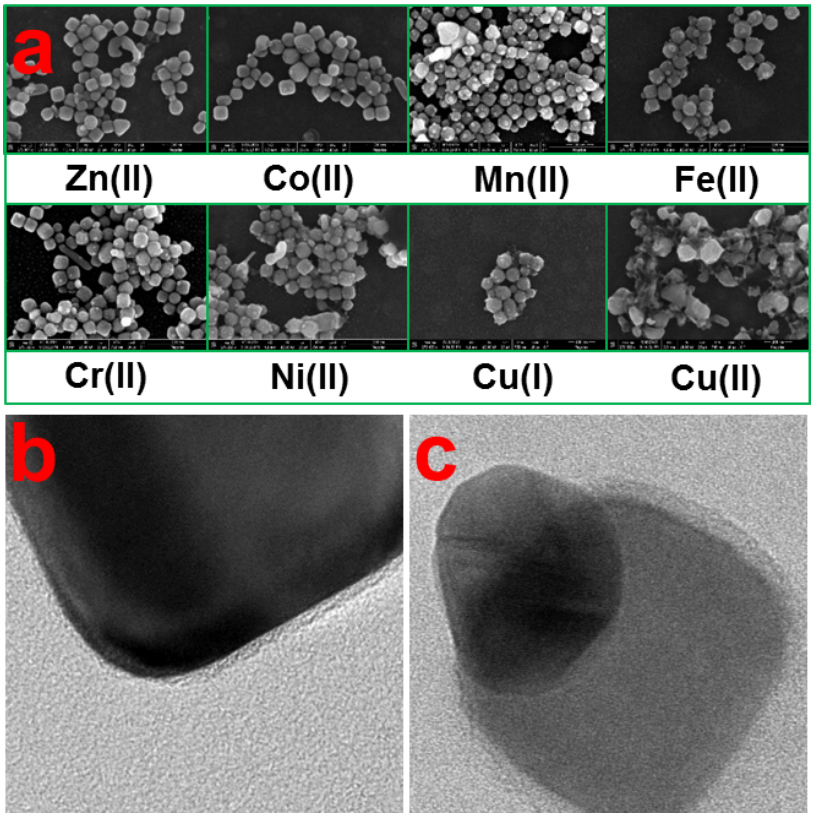

Figure 3.5 Efforts to remove PVP from Ag NCs surface.

(a) SEM image of Ag NCs treated with different transition metal ion ethanol solution. TEM images of Ag NCs after hot water wash (b) or UV-Ozone treatment (c).

3.2 Platform II - $Au/TiO_2/DBDT/Al_2O_3$

3.2.1 Stochastic Assembly of Au NCs

Commercially available citrated capped Au NCs were chosen as the second building block for Platform II. Although the SERS enhancement factor (EF) of Au NCs won't be as significant as the Ag nanocubes[259], the Au NCs with only citrate ligand on the surface

enables better control of the aggregation kinetics. The Au NCs from Sigma-Aldrich has a polydispersity index (PDI) less than 0.2, an average diameter of 35 nm, and an absorbance peak at 524.1 nm (Figure 3.6 b). The stochastic nantennas building procedure is similar to planform I except for the use of DBDT as the sensitizer and 10 nm of Al_2O_3 as the final protection layer. The bridge between Au NC dimer in Figure 3.6 d is induced by strong electron beam during imaging, which will be discussed in section 4.1.4.

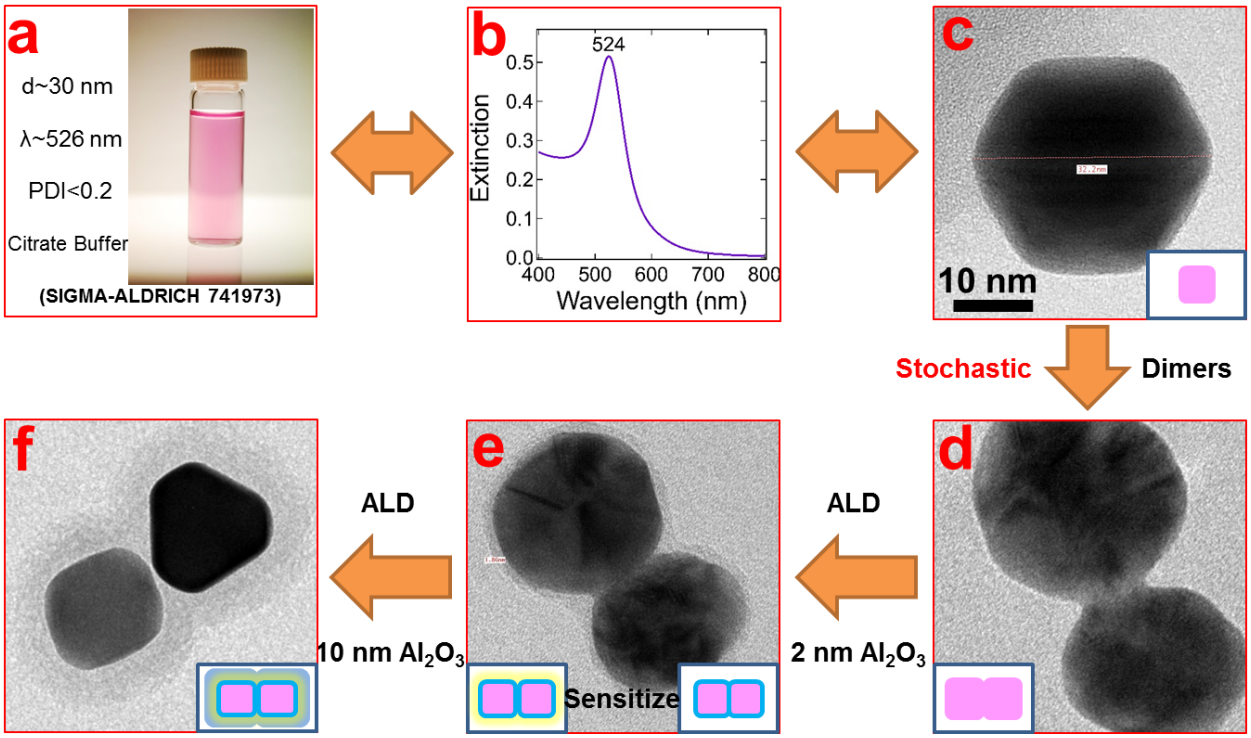

Figure 3.6 Procedure for assembling platform II - $Au/TiO_2/DBDT/Al_2O_3$.

(a) Photo and properties of Au NCs aqueous solution from Sigma Aldrich. (b) Extinction spectrum and (c) TEM image of Au NCs. (d) Stochastically formed dimer by drying Au NCs solution on a TEM grid. (e) Dimer after ALD of 2 nm TiO_2. (f) Dimer after sensitizing with DBDT and ALD of 10 nm Al_2O_3.

3.2.2 Alkane Dithiol-mediated Assembly of Au NCs

The yield of desiring structures (dimers, trimers, and mall clusters) in the randomly drop casted sample is less than ~3% without any control. For this project, a controllable way of assembling NCs is appreciated. With cleaner surface compare to the Ag NCs, chemical linkers which form a strong covalent bond with Au NCs can be applied similarly. In the past, Raman active dithiol molecules containing benzene rings were selected to act as both linker and reporter[260,261]. On the other hand, Raman silent linker is needed in this study to build a "silent platform" to serve the study of Raman active molecules in the future. Similar to the Ag NCs, simple alkane dithiols were chosen to start.

The optical extinction spectrum (Figure 3.7 a-d) of the Au NCs aqueous solution were monitored after adding different dithiols at different concentrations. Similar to the spectrum change of Ag NCs, a shoulder peak around 650 nm is developed in 1 hour with 100 and 500 μM of 1,5-pentanedithiol (Pen), and 1,6-hexanedithiol (Hex). We attribute this to the development of longitudinal plasmon mode due to the NC aggregation. The data shows a trend that the longer the carbon chain, the more effective the cross-linking.

However, the degree of aggregation is much lower than Ag NCs even at [dithiol] = 500 μM, which might occur due to the low [NC] (1.8×10^{11} NCs/mL). More importantly, the kinetics of the reaction was not reproducible. Multiple environmental factors that might influence the aggregation process (temperature, light, and atmosphere) have been carefully controlled while none of these factors show significant impact on the aggregation rate. We found that Sigma Aldrich added a proprietary surfactant in addition to the sodium citrate to further stabilize the Au NCs. To gain better control of the solution content, we decided to synthesize our own Au NCs.

On the other hand, the simple alkane dithiols are soluble in organic solvent only. This makes it hard to judge the actual concentration of dithiols in aqueous Au NCs solution. Also, the mixture of ethanol and H_2O further complicates the solvent system. Thus, a water-soluble dithiol HEGDT was chosen to continue the study.

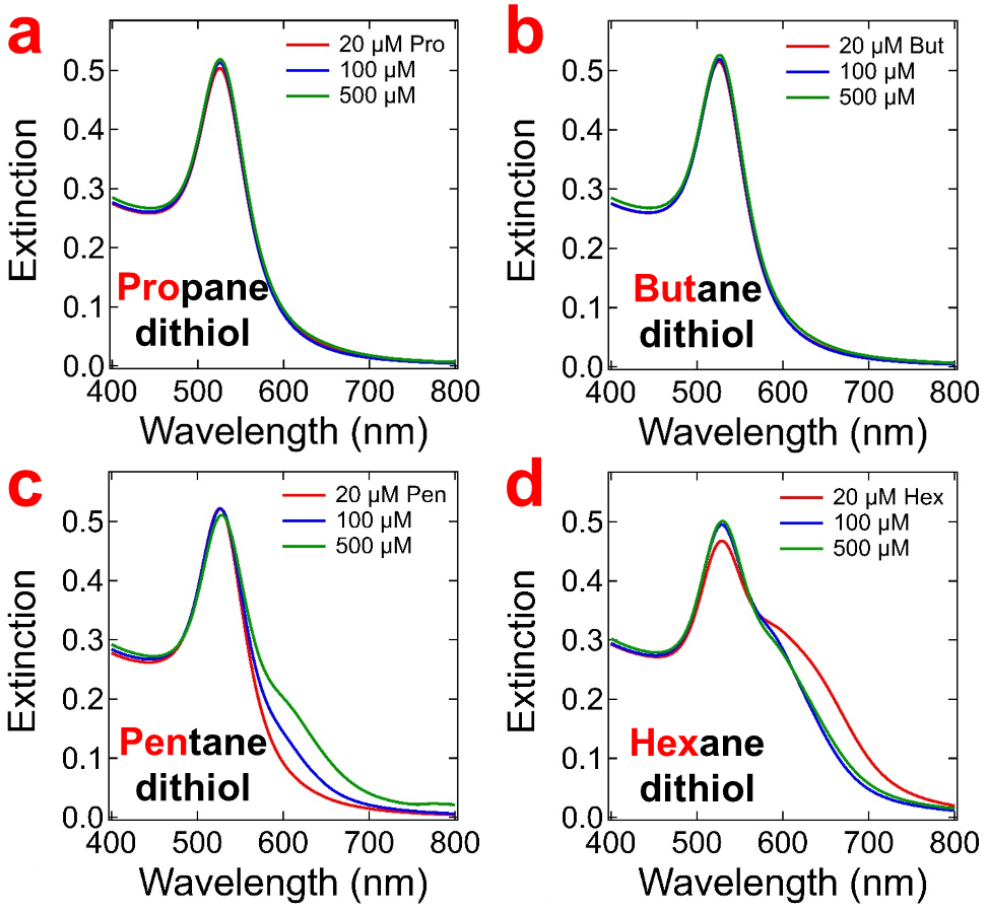

Figure 3.7 Alkane dithiol-mediated assembly of Au NCs.

(a-d) Time series of optical extinction spectrum of the commercial Au NCs aqueous solution after adding alkane dithiol ethanol solution. The final dithiol concentrations are 20, 100, and 500 μM.

3.2.3 Raman Activity of Platform II

The Raman activity of Platform II (made by stochastic assemble) versus bulk DBDT were determined with the same setup. The peak positions of bulk DBDT and DBDT on platform II (Figure 3.8) agree with literature well[260]. Briefly, the three strongest peaks at 1084, 1276, and 1591 cm^{-1} are attributed to the C-S, C-C, and C=C stretch coupled to C-C stretch. ~25 dimers were examined while no detectable SERS was observed, which might be due to the low coverage of DBDT within the junction limited by its affinity to TiO_2. The probability of finding the molecules residing in the hotspot increases with the total number of junctions. Thus NC clusters have a better chance to be SERS active.

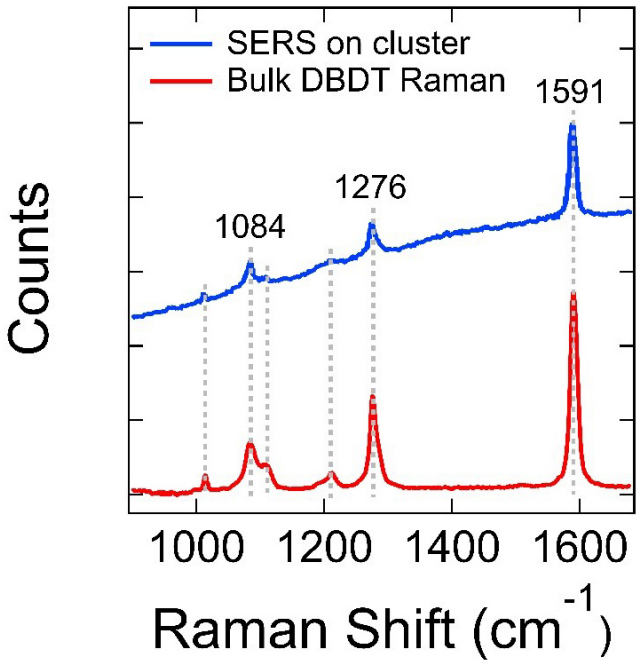

Figure 3.8 Raman spectrum of platform II cluster.

4 Reversible Aggregation of Au NCs

In the previous chapter, we have demonstrated the Ag and Au NCs can be effectively coated by ALD (TiO_2 or Al_2O_3). As a proof of concept, we build the platform I with randomly aggregated Ag NCs aiming to study the well-known photoinduced electron transfer from ruthenium dye N719 into TiO_2. Similarly, the Raman reporter DBDT has been loaded and tested on TiO_2 coated Au NCs to demonstrate the versatility of our platform. The initial study of controllable aggregation of Ag or Au NCs using alkane dithiols shows promising results with challenges.

In this chapter, our attempt to control the aggregation of Au NCs triggered by the addition of Raman-silent dithiol linkers is discussed. We select hexa(ethylene glycol) dithiol (HEGDT), a water-soluble dithiol with a weak Raman cross section. We then attempt to arrest the aggregation for yielding a suspension of colloidal aggregates with a relatively high percentage of dimers by rapidly oxidizing the free thiols with ozone (Figure 4.1). We found that ozone is very active on selectively oxidizing the dithiols to disulfonic acids, resulting in the destruction of the dithiol linkers and complete depolymerization of NC aggregates to re-form a stable colloidal solution of individual Au NCs. NMR and pH data confirms that disulfonate is the primary ozonation product of dithiol. This chapter summarizes our understanding of the aggregation-deaggregation cycle, which enable us to exert more control over the process.

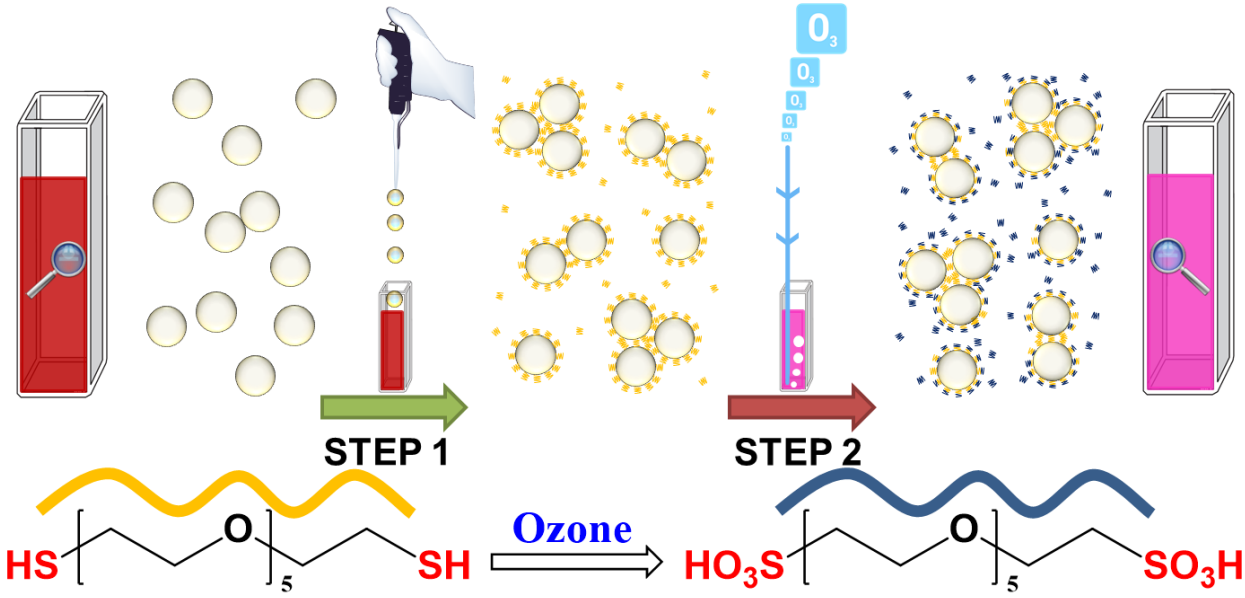

Figure 4.1 Scheme of controllable aggregation of Au NCs using HEGDT and ozone. Addition of excess dithiol triggers the large-scale cross-linking of colloidal Au NCs in water, resulting in rapid cross-linking of NC-dithiolate polymer. Subsequent ozone bubbling selectively oxidizes the free thiol and stop aggregation to yield a high percentage of dimers.

4.1 HEGDT-mediated Assemble of Au NCs

4.1.1 Formation of NC-dithiolate Polymer

We monitored the aggregation of the 10 nm as-made Au NCs after mixing with 50 μM HEGDT using optical extinction spectroscopy (UV-Vis) and dynamic light scattering (DLS). Figure 4.2 a shows the intensity of the plasmon peak at ~521 nm decreases while a broad peak grows at longer wavelength upon adding HEGDT. This behavior is a characteristic of the formation of colloidal NC aggregates. The growth of the hydrodynamic diameter of the NCs aggregates from ~16 to 560 nm over 120 minutes monitored by DLS (Figure 4.3 b)

agrees with the UV-Vis result. After ~150 minutes, the original ruby red NC solution turned colorless with a powdery black precipitate rested on the bottom and sides of the vial.

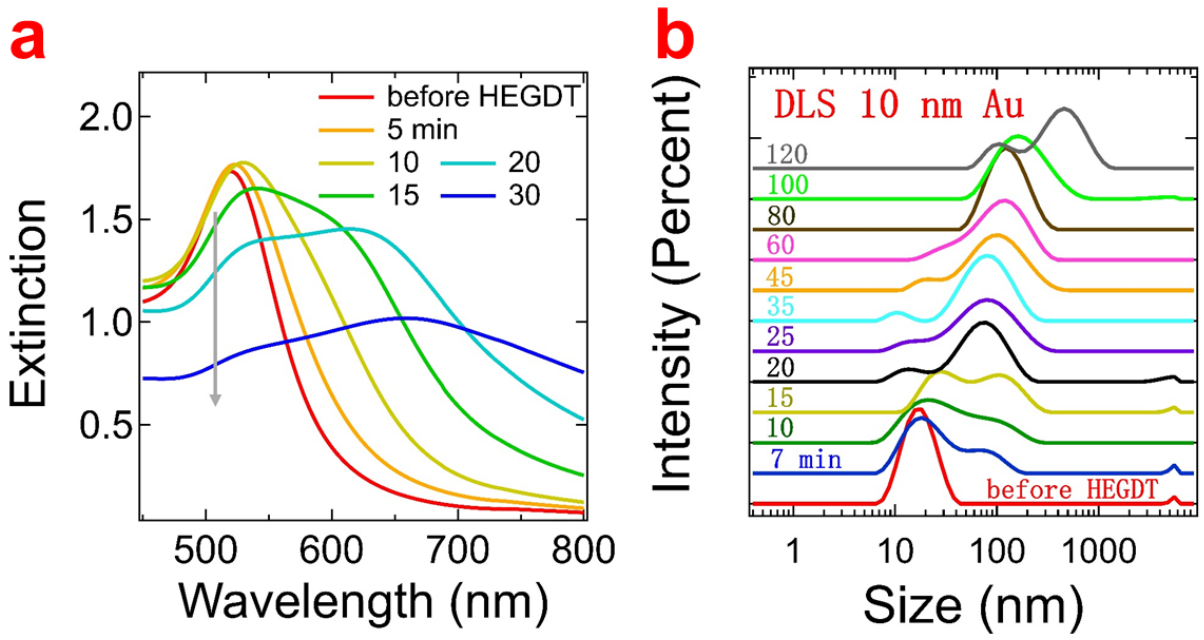

Figure 4.2 HEGDT-mediated aggregation of Au NCs.

Time series of optical extinction spectrum (a) and hydrodynamic diameter (b) of the 10 nm Au NCs after adding aqueous hexa(ethylene glycol) dithiol (HEGDT).

The effectiveness of HEGDT acting as a linker was first verified using 10 nm Au NCs. Later on, 23.8 ± 4.2 nm (diameter) citrate-capped Au NCs were synthesis and used throughout the study since it was easier to image larger particles in both SEM and optical microscopes (backscattered configuration). In addition to the NCs, the reaction solution contains 2.65 mM free citrate ion, 4.19 mM Cl^-, 9.81 mM Na^+, 0.29 mM acetone, 0.05 mM acetic acid, and probably various undetected organic and inorganic species, all at pH 6.0 (total ionic strength of ~14 mM). Details of determining the solution components can be found in section 4.9. The molar ratio of HEGDT to NCs in this experiment ([HEGDT]/[NC] =

4000) was large enough to quickly and completely precipitate the NCs (a “hard crash” of the NCs). The formation of larger clusters over time after adding HEGDT was confirmed by TEM images (Figure 4.3).

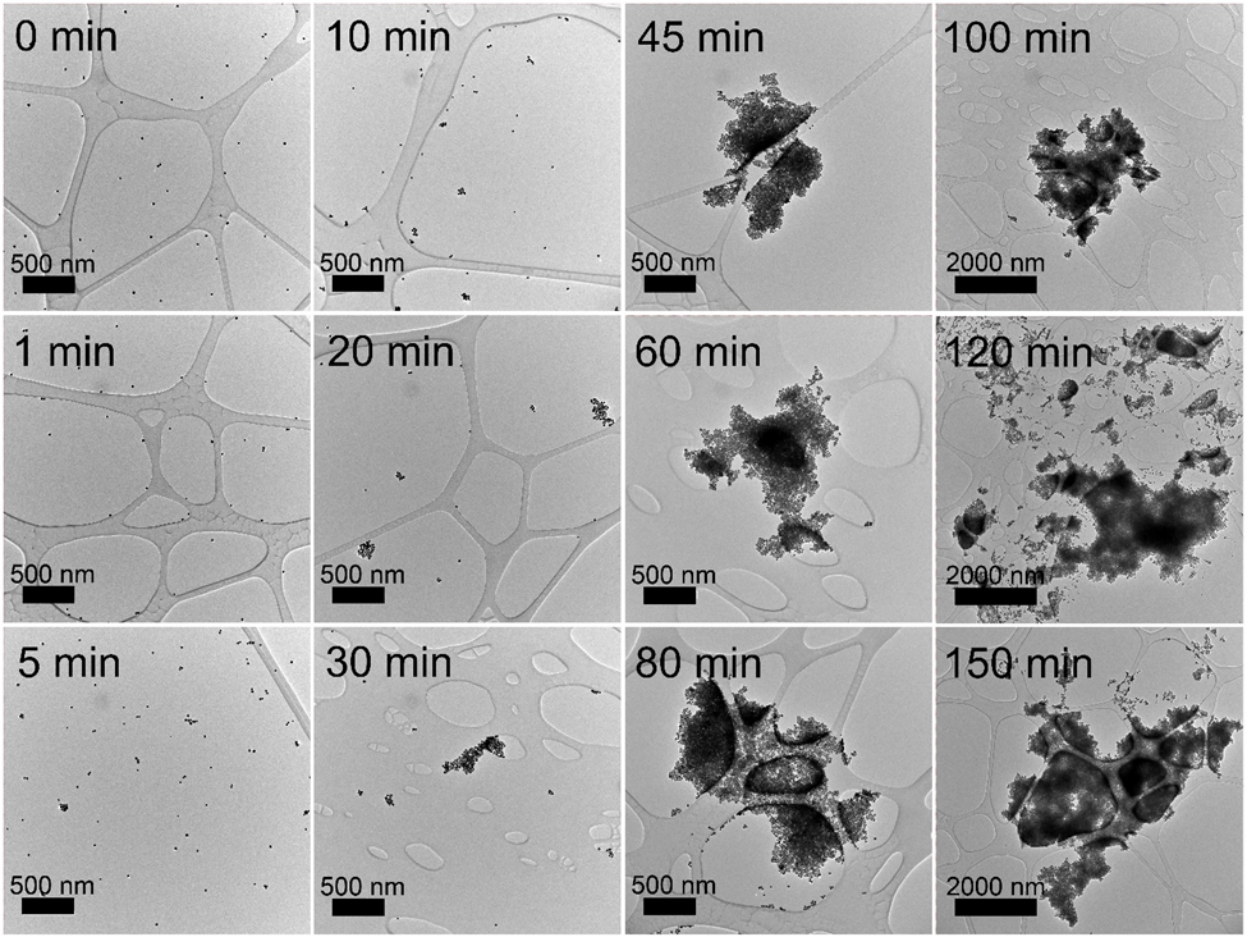

Figure 4.3 Time series of TEM images showing the aggregation process of 24 nm Au NCs. Labels indicate the time after HEGDT addition (0 min is the control sample without dithiol). The samples were prepared using a technique that minimizes the artificial formation of clusters during the drying of the solution on the TEM grid.

4.1.2 Raman Activity of the linked NCs

HEGDT was the main focus of this study because oligo ethylene glycol dithiols are water soluble, short, and have small Raman scattering cross sections compare to Raman active molecule like biphenyl-4,4'-dithiol (DBDT) (Figure 4.4 a), making them suitable Raman-silent linkers for the fabrication of high-performance SERS dimer nantenna. Addition of HEGDT to a suspension of Au NCs results in rapid precipitation of a NC-dithiolate polymer. This polymer shows a nearly featureless Raman spectrum. In comparison, samples prepared in the presence of Raman reporter molecules such as DBDT exhibits strong peaks in SERS spectrum, indicating that reporter molecules readily find adsorption sites within the hot spots (Figure 4.4 b). Thus, these HEGDT-linked Au NCs are promising for single-molecule SERS studies.

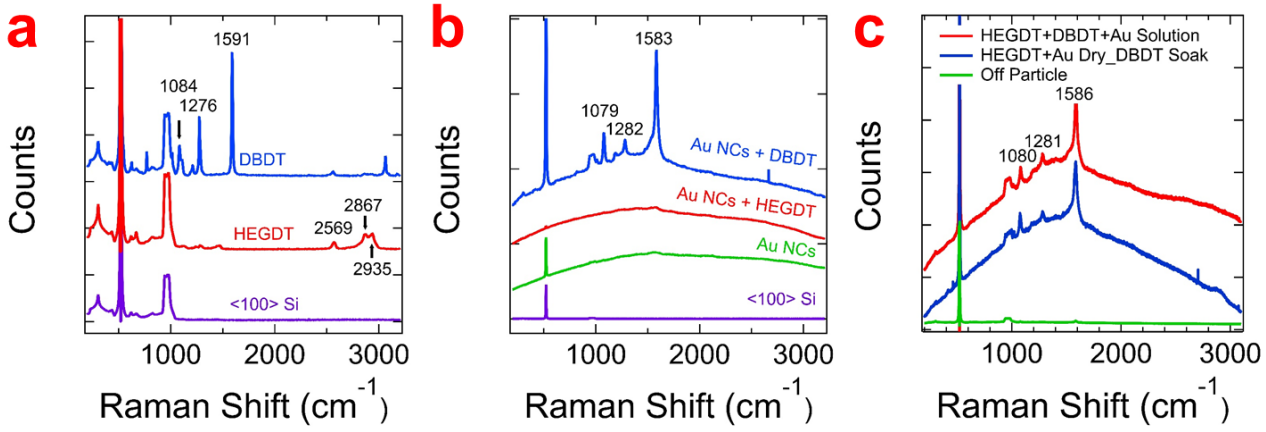

Figure 4.4 Comparison of Raman and SER activity of HEGDT and DBDT.

Raman spectrum of (a) HEGDT or DBDT molecules and (b) as-made Au NCs cross-linked by HEGDT or DBDT on the Si substrate. (c) Au NCs are cross-linked by HEGDT first then load with DBDT using co-absorption or step-by-step methods.

Furthermore, the NC-dithiolate polymer soaked in DBDT solution (step-by-step method) or HEGDT/DBDT co-treated (co-absorption method) Au NCs exhibit the same strong SERS signal (Figure 4.4 c). This indicates the existence of available binding sites for reporter molecules after HEGDT cross-linking. Upon thorough washing after loading NC-dithiolate polymer with DBDT, no Raman signal (Figure 4.4 c, green line) from either HEGDT or DBDT can be found when moving the laser away from the NC clusters. Besides, the ratio between the three most intense peaks of the bulk DBDT (see the assignment in section 3.2.3) changes compare to the DBDT loaded on Au NCs. Both pieces of evidence indicate the Raman signal comes from the molecule bonded to Au NCs, not the free molecule. Note, forming a chemical bond with NCs is not necessary for the nantennas to work. 10% of laser power was selected when acquiring the spectrum to avoid damaging the structure or molecule. At 15% laser power, signal loss becomes evident during the acquisition.

4.1.3 ALD compatibility of the linked NCs

The HEGDT cross-linked NCs were dried on Si_3N_4 TEM grid then loaded into ALD chamber. We tested alumina deposition at relatively low temperature (35 °C) to protect the structure. EDS mapping of the coated NCs (Figure 4.5) show Al and O rich shell with Au and S rich core. This confirms the compatibility of the HEGDT linked/covered NCs with the ALD process. Meanwhile, the low-temperature deposition preserves the HEGDT on the NC surface. Thus, the nantennas built by HEGDT cross-linking should exhibit similar Raman activity after ALD coating compares to platform I and II.

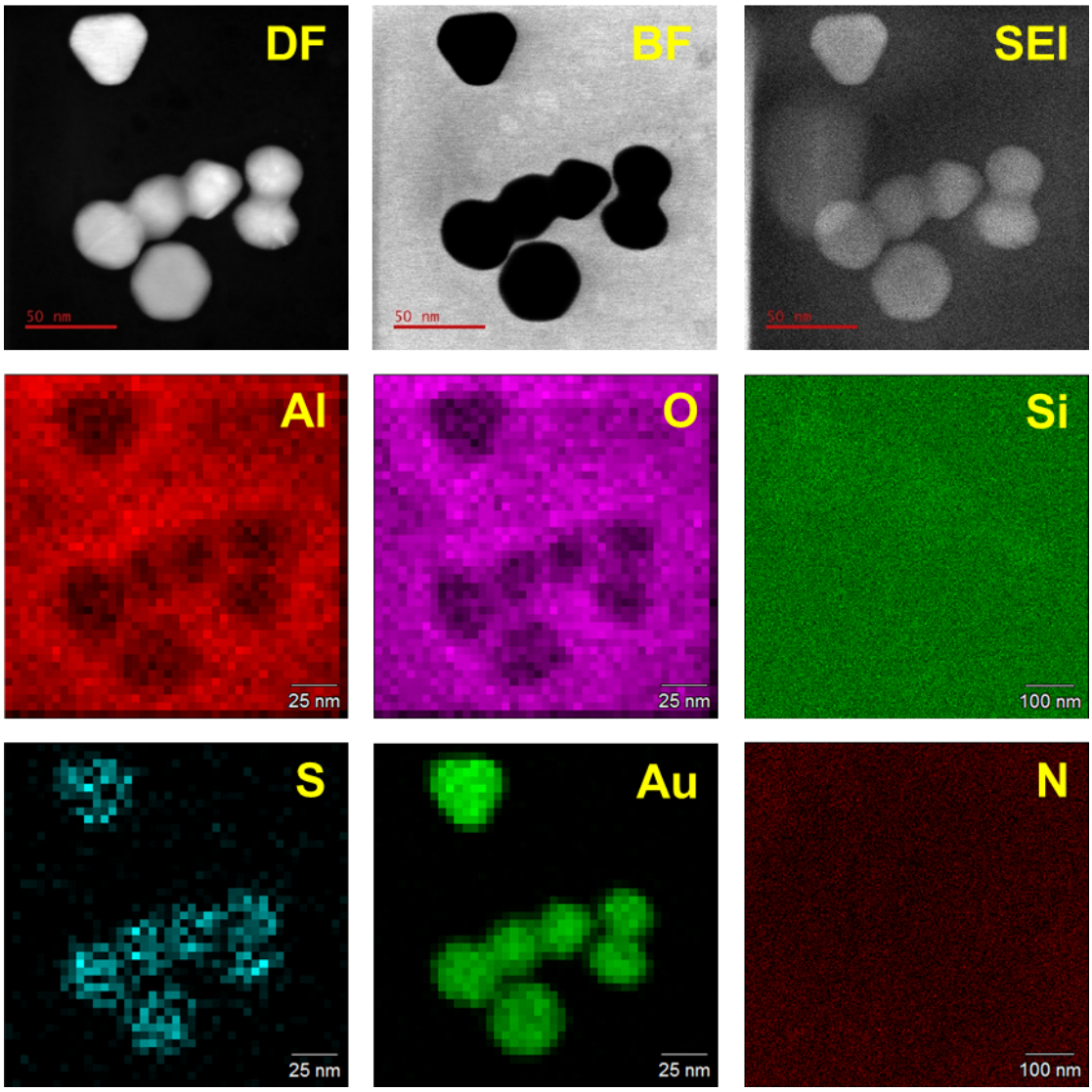

Figure 4.5 EDS mapping of HEGDT cross-linked Au NCs with Al_2O_3 ALD coating.

4.1.4 Gap Distance Measurement

Distance between the NCs significantly changes the Raman enhancement factor[262,263]. Thus, rational tuning of the distance using molecular linkers with different lengths is critical. More importantly, measuring the gap distance accurately is vital prior to tune it as the difference in molecule lengths fall into sub-nm scale. However, the inter-NC spacing cannot be measured accurately due to the e-beam induced expanding/merging under

normal operation condition. Figure 4.6 top series and Figure 3.6 d are examples of gap fusion (in less than 10 seconds) when operating the electron microscope at 200 keV and room temperature. We employed cryo/cooling-TEM with low keV condition to image dimers and other plasmonic assemblies with minimal beam-induced sample damage (Figure 4.6 bottom series). Combining small CL aperture, large spot size, LN_2 cooling, low keV, and imaging at low magnification, we determined the inter-NC spacing of HEGDT linked NCs to be 5.5 ± 1 Å. The short distance implies a tilt angle of 75-80 degrees between HEGDT and NC as the S-S distance of HEGDT is 19.8 Å. In other words, the molecules are almost lying flat on the Au surface.

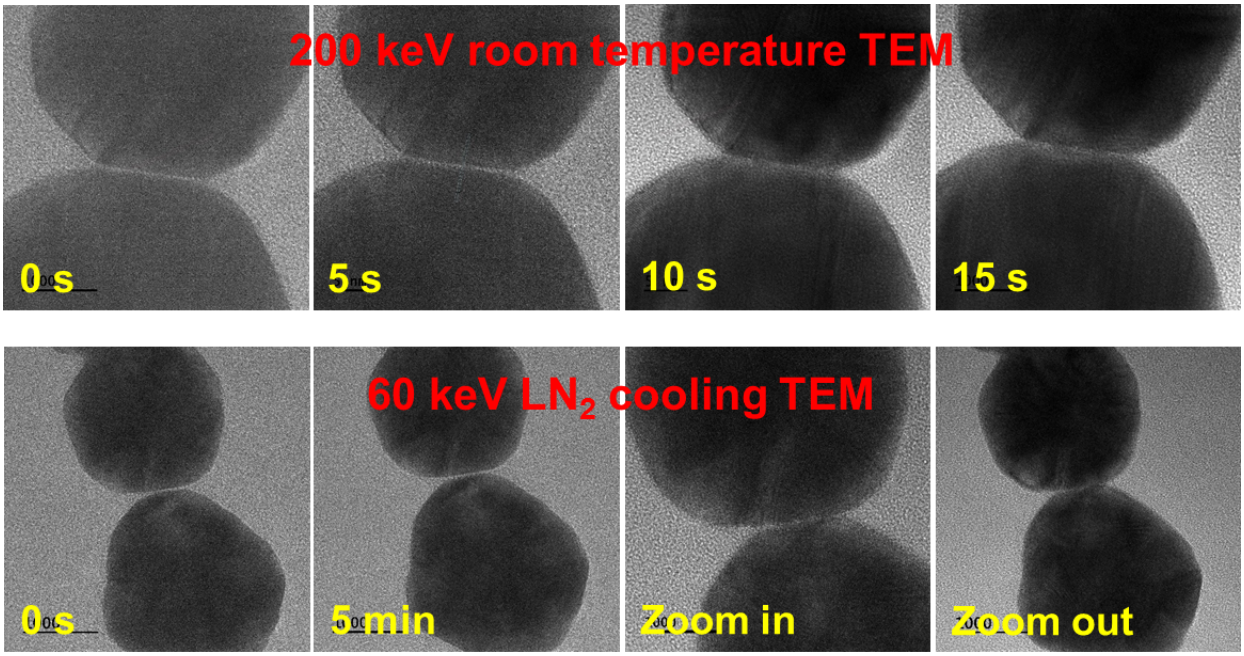

Figure 4.6 Beam effect on NC dimer.

(Top series) gap fusion in less than 10 seconds at 200 keV normal imaging mode. (Bottom series) Gap "stable" at 60 keV with LN_2 cooling for 5 minutes. However, the dimer fuses when further zoom in.

4.2 Ozone-mediated Redispersion of Au NCs

The water-soluble HEGDT can effectively start the cross-linking of Au NCs while an inhibitor is needed to stop the aggregation to yield a high percentage of dimers. Ozone was introduced in our study to selective oxidize the active dithiol linker and "quench" the reaction to produce stable colloidal dimer solution. Surprisingly, we found that ozone oxidized not only the free dithiol but also the linker dithiolate between NCs, which resulted in nearly complete dissociation the NC-dithiolate polymer (Figure 4.7 a).

The Au NC precipitates slowly redispersed after brief exposure to ozone (Figure 4.7 c). Samples were bubbled with an ozone/oxygen mixture under sonication for five minutes, sparged with argon without sonication for one minute to remove the ozone and allowed to stand in ambient conditions at room temperature (see more details in section 2.4.1). Within a minute of adding ozone, all of the black solids was consumed, and the colorless solution turned dark blue, then gradually deep ruby red over several days (Figure 4.7 c). After ~7 days, the solution spectrum (peak position 528.5 ± 0.04 nm, peak width 53.2 meV) closely matched the spectrum of the original NC dispersion (peak position 526.9 ± 0.05 nm, peak width 49.3 meV) before the addition of HEGDT. This is strong evidence that ozonation completely redisperses the precipitates to form a sol of individual Au NCs with only a small fraction of dimers and larger aggregates.

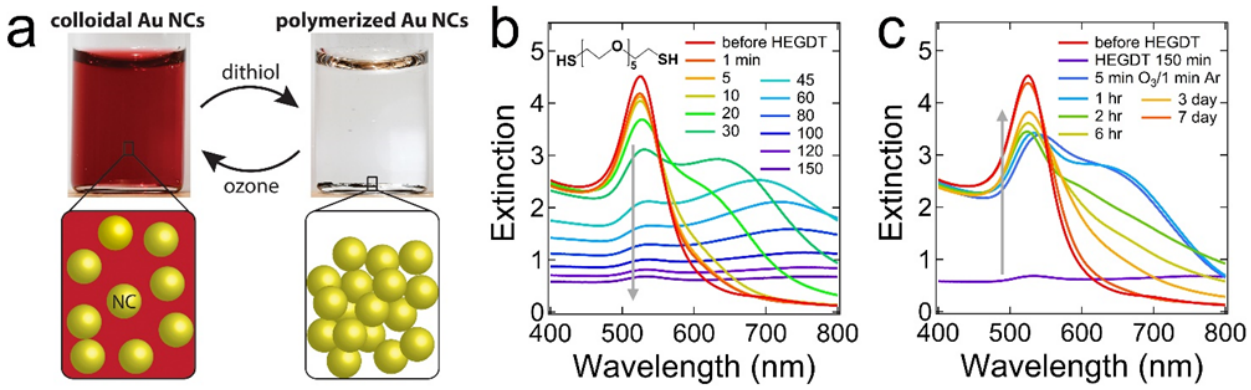

Figure 4.7 Redispersion of dithiol linked Au NC precipitates with ozone.

(a) The reaction scheme explored in this paper. Addition of excess dithiol triggers the large-scale cross-linking of colloidal Au NCs in water, resulting in rapid precipitation of a NC-dithiolate polymer. Subsequent ozone bubbling depolymerizes and completely redisperses the NCs. (b) Time series of optical extinction spectrum after adding aqueous hexa(ethylene glycol) dithiol (HEGDT) to the NC suspension ([HEGDT]/[NC] = 4000). The molecular structure of HEGDT is shown in the inset. (c) Spectral time series upon ozonation of the precipitated NC-HEGDT polymer using 5 min of ozone bubbling with sonication followed by a 1 min argon sparge at room temperature.

4.2.1 NC Size and Morphology

TEM images confirmed the redispersion of the NC precipitates (Figure 4.8 a). Size histograms compiled from the TEM images (>500 NCs were measured) of samples before the addition of HEGDT and seven days after ozonation show that the average NC diameter and diameter distribution increased slightly from 23.8 ± 4.2 nm to 24.7 ± 7.4 nm. Solution small-angle X-ray scattering (SAXS) measurements gave very similar results (21.6 ± 3.9 nm and 22.7 ± 4.9 nm; see Figure 4.8 d).

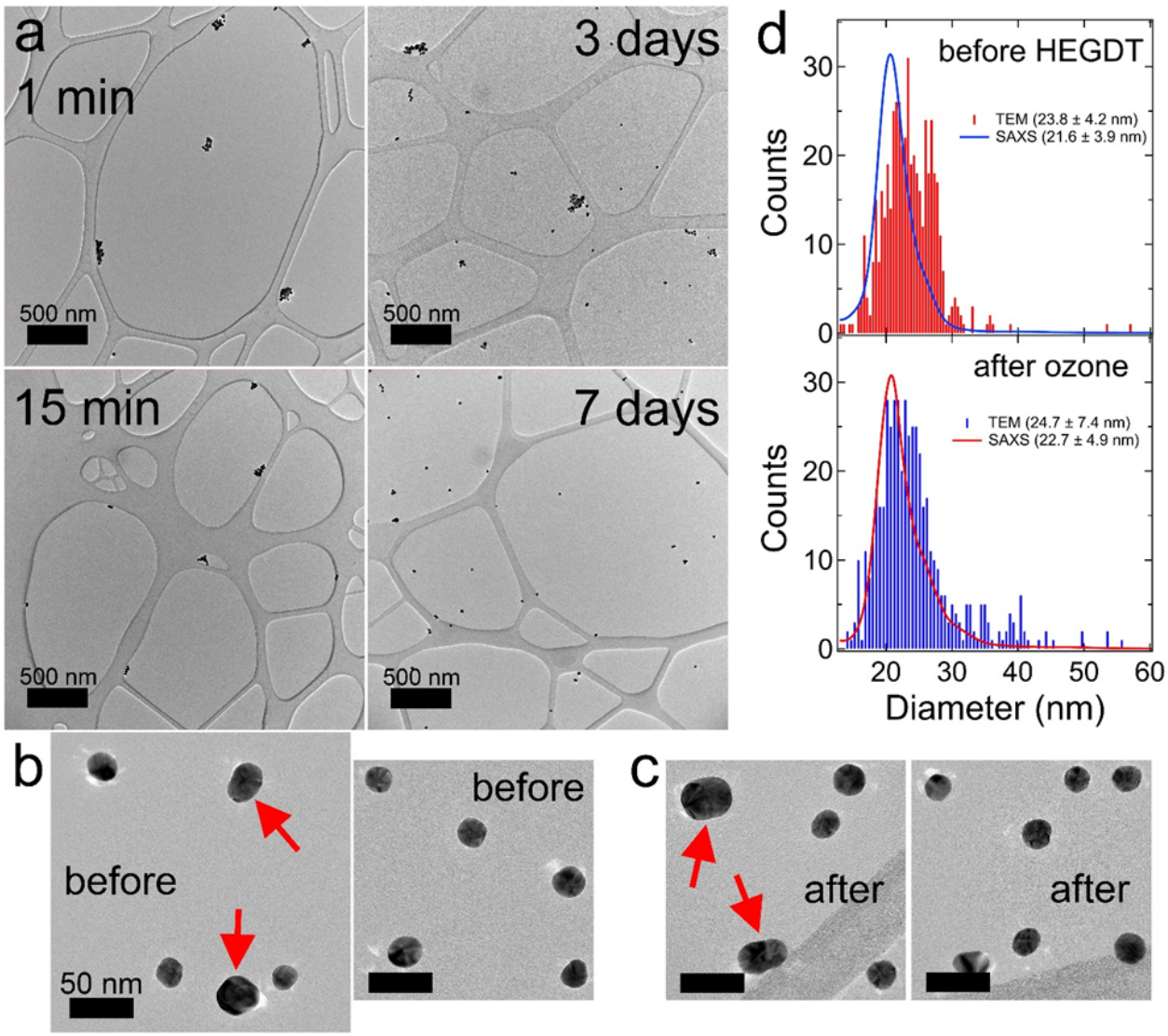

Figure 4.8 NC size change during and after ozone-mediate redispersion.

(a) A time series of TEM images showing the redispersion process upon ozonation of NC-HEGDT precipitates. Labels indicate the time after ozonation. (b-c) Typical higher-magnification images of the NCs (b) before the addition of HEGDT and (c) 7 days after ozonation. (d) Size histograms of the NCs before the addition of HEGDT and 7 days after ozonation, as determined by TEM (>500 NCs) and colloidal small-angle X-ray scattering (SAXS).

The images and histograms show that the size and shape of most of the NCs are nearly unchanged after one precipitation-redispersion cycle. The average diameter and standard deviation are listed. However, a small number of NCs does grow in size (visible as a tail in the size distributions), probably as a result of the occasional metallic fusion of neighboring NCs within the precipitates (Figure 4.8 b-c). The red arrows highlight several larger NCs in each type of sample. Most of these large NCs appear to be strongly fused dimers of the smaller NCs. Our finding of insignificant etching and oxidation of Au NCs by brief ozone treatment is consistent with previous reports[264,265]. The NC sols are indefinitely stable after ozonation and showed minimal additional spectral changes after more than one year of storage in ambient light at room temperature. All samples were prepared using a technique that minimizes the artificial formation of clusters during drying of the solution on the TEM grid (see section 2.5.1 for details).

4.2.2 [HEGDT] to [NC] ratio

We next evaluated the effect of different [HEGDT]-to-[NC] ratio surface coverages on the NC polymerization and depolymerization reactions. We tested [HEGDT]-to-[NC] ratios of 2000k, 1000k, 500k, 250k, 125k, 50k, 25k, 10k, 4000, 2000, 1600, 1200, 800, 400, and 200 for comparison. The [HEGDT]/[NC] ratio has a large effect on the extent and speed of NC aggregation and redispersion. Very low ratios (<1000) cause no measurable aggregation (insignificant spectral changes even days after mixing). Ratios of ~1000-2800 resulted in the increasingly large aggregation but no precipitation. Ozonation of these samples one day after HEGDT treatment caused an immediate redshift of the plasmon peak from 524 nm to 533 nm and slow recovery to the original, pre-HEGDT spectrum in ~3 hours, indicating

complete redispersion of the colloidal aggregates into individual NCs. Control experiments show that this fast redshift and slow recovery are caused by adsorption and desorption of ozone on the surface of the NCs[264,265,266,267,268] rather than the redispersion itself. The redispersion is probably quite fast (minutes or less) because the aggregates are small and have relatively low coverage of HEGDT linkers at this low [HEGDT]/[NC] ratio.

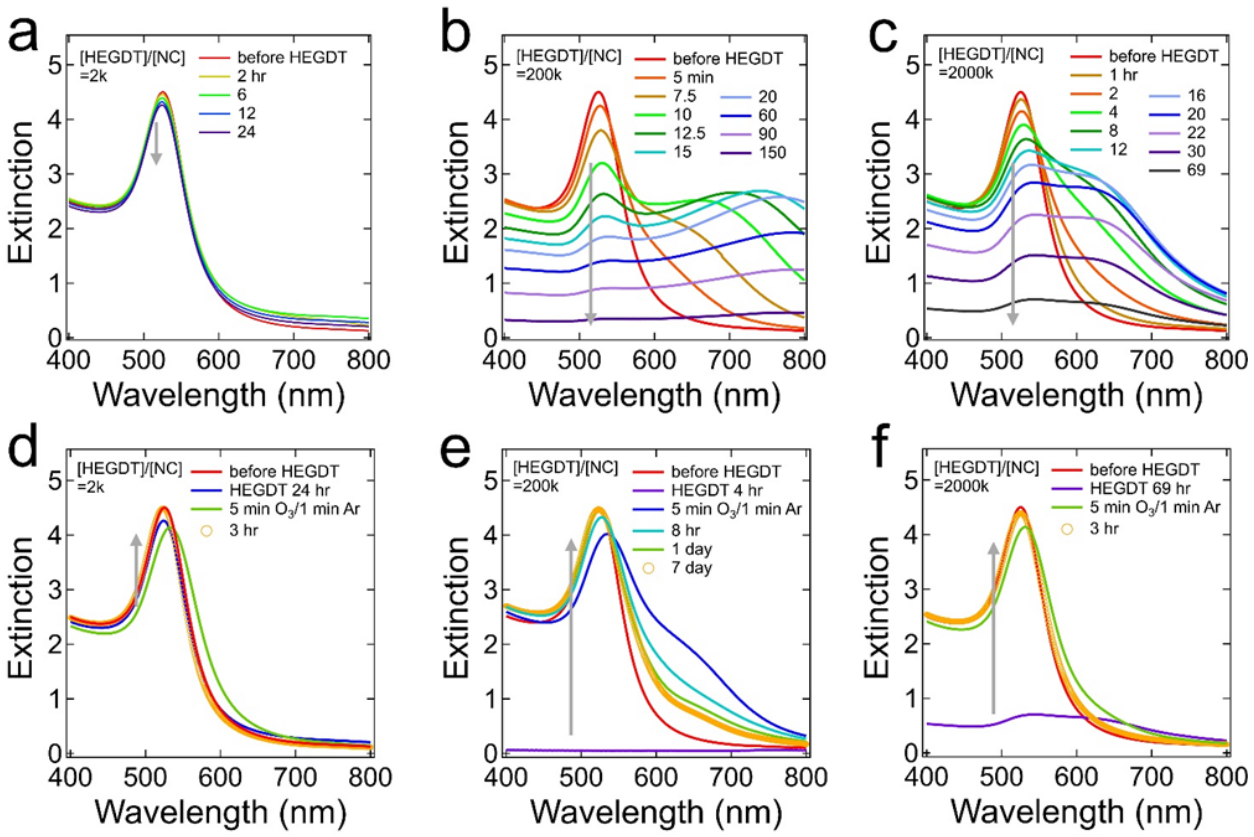

Figure 4.9 Aggregation and redispersion of different [HEGDT]-to-[NC] ratio.

(a-c) Time series of optical extinction spectrum after adding aqueous hexa(ethylene glycol) dithiol (HEGDT) to the NC suspension ([HEGDT]/[NC] = 2k, 200k, 2000k). (d-f) Spectral time series upon ozonation of the precipitated NC-dithiolate polymer with 5 min of ozone bubbling followed by a 1 min argon sparge and with sonication at room temperature.

Figure 4.9 shows three sets of the representative extinction spectrums. Only small aggregates were formed at [HEGDT]/[NC] = 2,000 from TEM (not shown here) which resulted in small change of the spectrum (Figure 4.9 a).

Complete polymerization (aggregation) was achieved when [HEGDT]/[NC] ≥ 4k (Figure 4.7 b, Figure 4.9 b-c). We reason that (1) dithiols absorb to NCs and (2) NCs link to each other are the two steps for polymerization. The driving force for the first step should be very large due to the large S-Au binding energy, whereas the second step is the rate-limiting step. The linking probability is related to HEGDT surface coverage. The NCs are less "sticky" when the surface coverage is very high (2000k) due to the limited number of active binding sites (bare Au atoms plus free thiol) which results in slow polymerization over three days (Figure 4.9 c) rather than hours (Figure 4.7 b, Figure 4.9 b). The slower polymerization at higher HEGDT concentration also rules out the cross-linking mechanism by forming disulfide between NCs. Lesser binding sites also lead to a lower density of cross-links, which results in full redispersion of the aggregates (Figure 2d, 2f) within 5 minutes. pH adjustment was needed before ozonation for 2000k sample to neutralize the high concentration hexa(ethylene glycol) disulfonic acid (HEGDS) formed during ozonation. Rapid redispersion can still be achieved by ozonation of 2000k precipitates washed by ultrapure water at pH ~ 12. The slow redispersion at 4k to 200k after removing ozone suggests that the rate of redispersion is not only limited to the density of cross-links holding the NC polymer together. Efforts have been made to determine the redispersion mechanism and control the redispersion rate in section 4.9. Figure 4.10 illustrates the dependence of the rates of NC aggregation and redispersion on [HEGDT]/[NC].

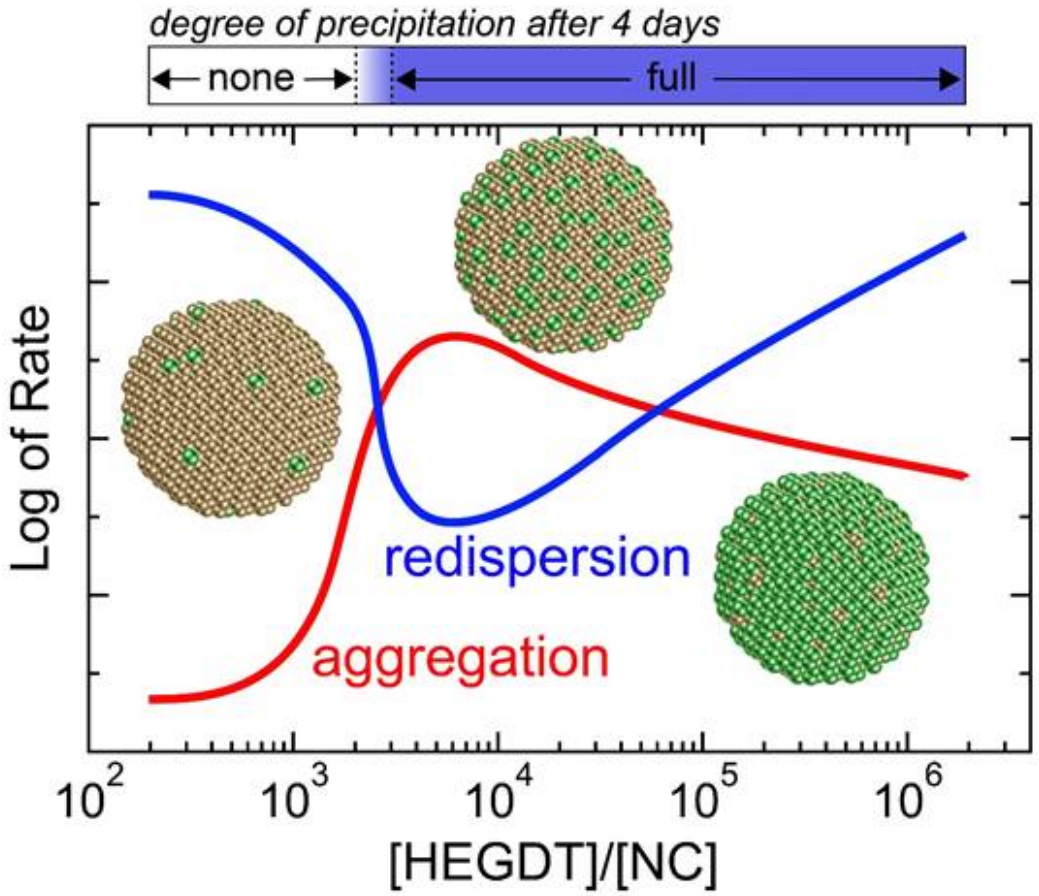

Figure 4.10 [HEGDT]/[NC] impact on the NC aggregation and redispersion rate.

Trends are deduced from the extinction spectrum. At both small and large ratios, aggregation is slow and redispersion is fast because the NCs have either a little coverage of linkers (at small ratios) or empty binding sites (at large ratios) and can form only a low density of cross-links. In contrast, aggregation is fast and redispersion is slow at intermediate ratios where more equal coverages of HEGDT and empty binding sites promote a high cross-link density. Inset are models of three Au NCs with increasing HEGDT coverage (green spheres) at higher values of [HEGDT]/[NC]. The blue color bar above the graph shows the amount of NC precipitation versus [HEGDT]/[NC] four days after HEGDT addition.

4.3 Aggregation Mechanism

4.3.1 Surface Ligand Displacement

We used attenuated total reflectance FTIR spectroscopy to determine whether HEGDT displaces citrate from the surface of our Au NCs. While thiols are generally believed to adsorb more strongly than citrate to colloidal Au NCs in water, the thiol-citrate surface exchange equilibrium constant is unknown, making it difficult to estimate the relative surface coverage of thiol and citrate during their competitive adsorption under different experimental conditions. We note that our observation of facile desorption of citrate in pure water is at odds with Park and Shumaker-Parry[269,270], who found significant retention of adsorbed citrate after rinsing Au NCs with water at pH ~10. Citrate is quite insoluble in ethanol, whereas it is extremely soluble in water. Our use of water as solvent (enabled by the high water solubility of HEGDT) should favor citrate displacement by thiols (i.e., ligand exchange rather than co-adsorption). Indeed, the ATR-FTIR data show that adsorbed citrate is easily removed by a brief rinse in pure water or treatment with aqueous HEGDT (Figure 4.11 a). Once adsorbed, HEGDT is firmly bound to the NCs and cannot be removed by prolonged rinsing in water or citrate solution (Figure 4.11 b-c). We conclude that HEGDT easily displaces citrate from the surface of Au NCs in water and the associated equilibrium constant is probably very large. The strong peak in the HEGDT spectrum at 1100 cm^{-1} is from C-O (ether) stretching. This adsorbed HEGDT can be removed by rinsing the sample in ozone-saturated water, leaving a flat and featureless FTIR spectrum (not shown). This latter result also indicates that HEGDS (the main product of HEGDT ozonolysis) is only weakly bound to the NCs and easily washed away by water.

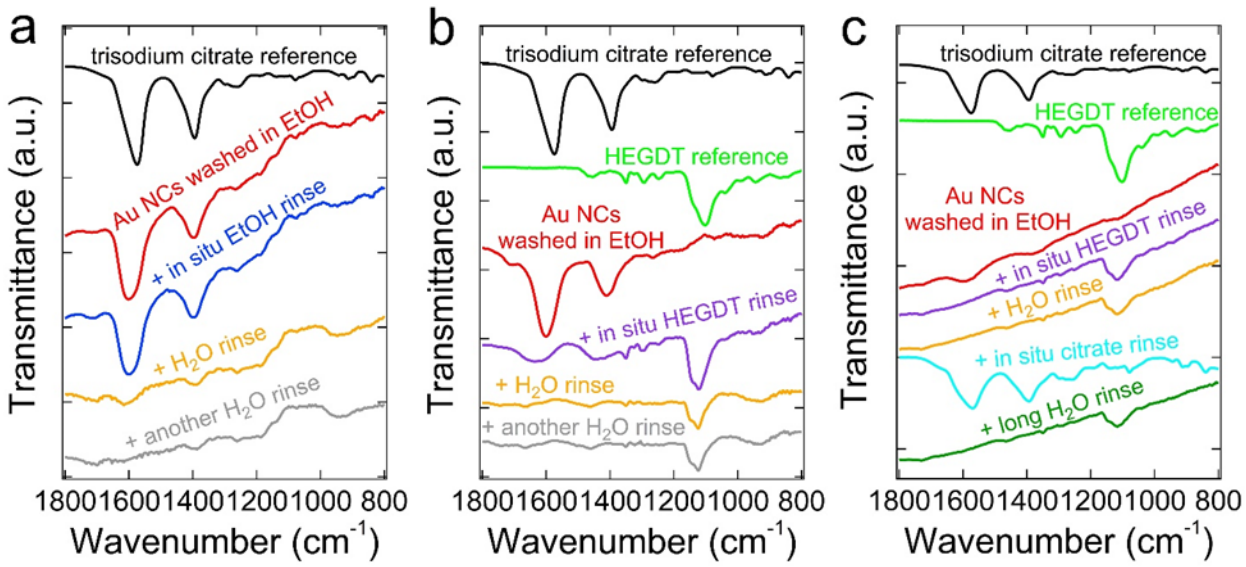

Figure 4.11 HEGDT displacement of citrate on Au NCs.

(a) The attenuated total reflectance FTIR spectrum of citrate-capped Au NCs cleaned by four cycles of centrifugation and washing in pure ethanol then deposited onto the ATR crystal from a concentrated aqueous suspension. (red trace) The NCs dried on the ATR crystal. (blue trace) The same NC sample after rinsing with 1 mL ultrapure ethanol on the ATR crystal. (orange trace) The same sample after rinsing with 1 mL of ultrapure water. The citrate is mostly removed. (gray trace) The sample after a second water rinse. The citrate is totally removed. (black trace) A trisodium citrate reference spectrum. (b) ATR-FTIR data for the same type of NC sample as in (a) after drying on the ATR crystal (red trace), rinsing with 1 mL of 10 mM aqueous HEGDT (purple trace), and subsequently rinsing with ultrapure water once (orange trace) and twice (gray trace). (c) ATR-FTIR data for the same type of NC sample as in (b) after drying on the ATR crystal (red trace) , rinsing with 1 mL of 10 mM aqueous HEGDT (purple trace), rinsing with 1 mL of ultrapure water (orange trace), rinsing with 1 mL of 1 M trisodium citrate aqueous solution (cyan trace), and subsequently rinsing with ultrapure water for 30 minutes twice (dark green trace).

4.3.2 Surface Bonded to Unbonded Thiol Ratio

Despite the importance of the surface coverage of HEGDT, the exact percentage is hard to estimate due to the unknown mole fractions of bridging, dangling, and looped or flat HEGDT molecules within the NC polymer. XPS studies of the S 2p region with different [HEGDT]/[NC] (Figure 4.12 a, Table S1) show the unbonded thiol concentration increases with [HEGDT]. The unbonded thiol is over 50% at [HEGDT]/[NC] = 2000k, which indicates the presence of free HEGDT molecule on the NC surface.

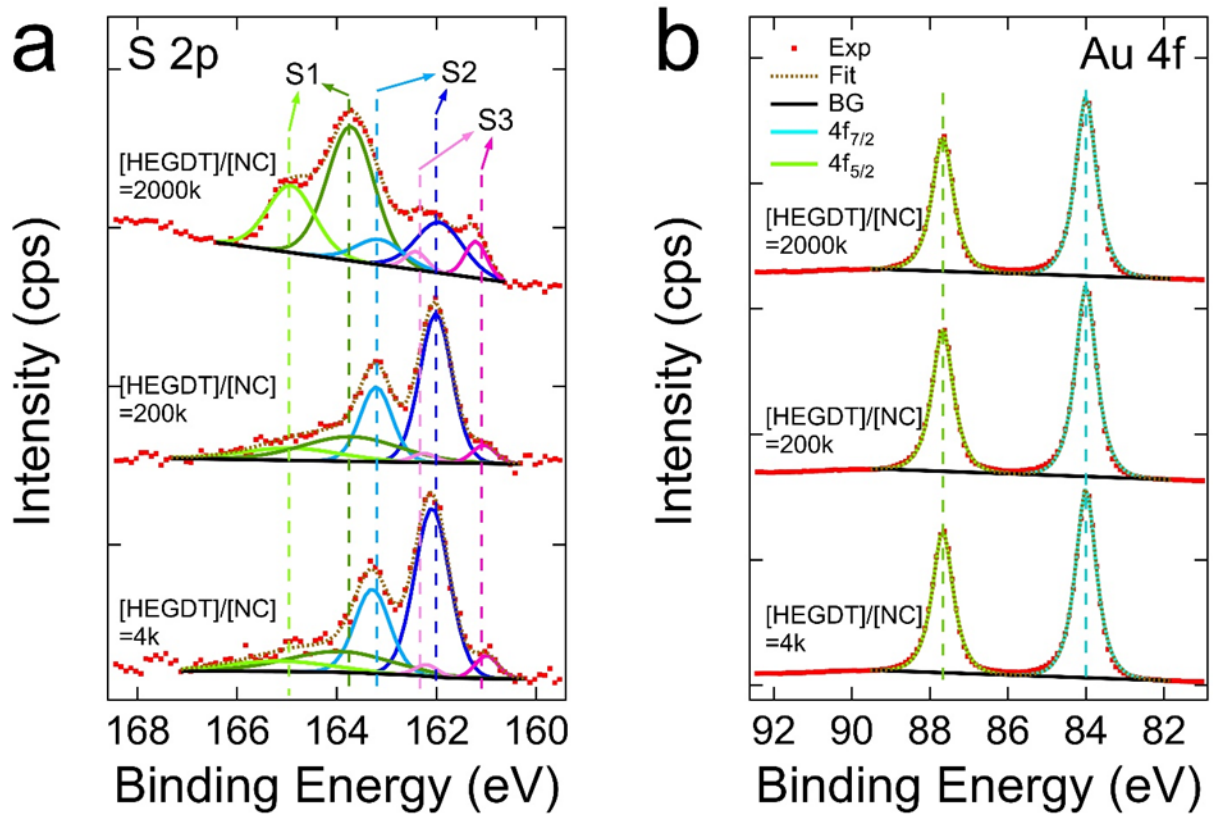

Figure 4.12 Surface bonded to unbonded thiol Ratio.

XPS of NC-HEGDT precipitates ([HEGDT]/[NC] = 2k, 200k, 2000k) (a) S 2p region and (b) Au 4f region. See section 2.5.6 for peak fitting method.

Table 1 S 2p region fitting and quantification results.

[HEGDT]/[NC]		Unbonded Thiol		Bonded Thiol		Bonded Thiol	
		S1		S2		S3	
4k	eV	165.14	163.94	163.29	162.09	162.20	161.00
	Area %	25.23		68.61		6.17	
200k	eV	164.92	163.72	163.21	162.01	162.25	161.05
	Area %	31.30		63.06		5.64	
2000k	eV	164.92	163.72	163.14	161.94	162.41	161.21
	Area %	66.51		25.12		8.36	

4.3.3 HEGMT Control Experiment

Control experiments with hexa(ethylene glycol) monothiol (HEGMT), which only contain one thiol (active linking group) were conducted to confirm the linking mechanism of Au-S bond formation further. Figure 4.13 of adding HEGDT to Au NCs solution at [HEGMT]/[NC] of 2000, 4000, 40k, and 400k shows little NC aggregation and no precipitation even three days after mixing. This suggests that HEGDT-induced aggregation results mainly from covalent cross-linking of the NCs rather than changes in NC surface charge, ligand hydrophobicity, or other factors. Note, the spectrum started to have a noticeable difference after seven days. The NCs began to precipitate over one month may be due to the esterification between -OH on the HEGMT and -COOH on citrate[271].

Due to strong covalent cross-linking by HEGDT, these NC precipitates could not be redispersed by any combination of prolonged sonication and heating (up to 100°C) in water (at any pH) or common organic solvents. However, the precipitates can be redispersed to some degree when adding monothiol to the supernatant due to the thiol self-exchange reaction (discussed in section 4.8).

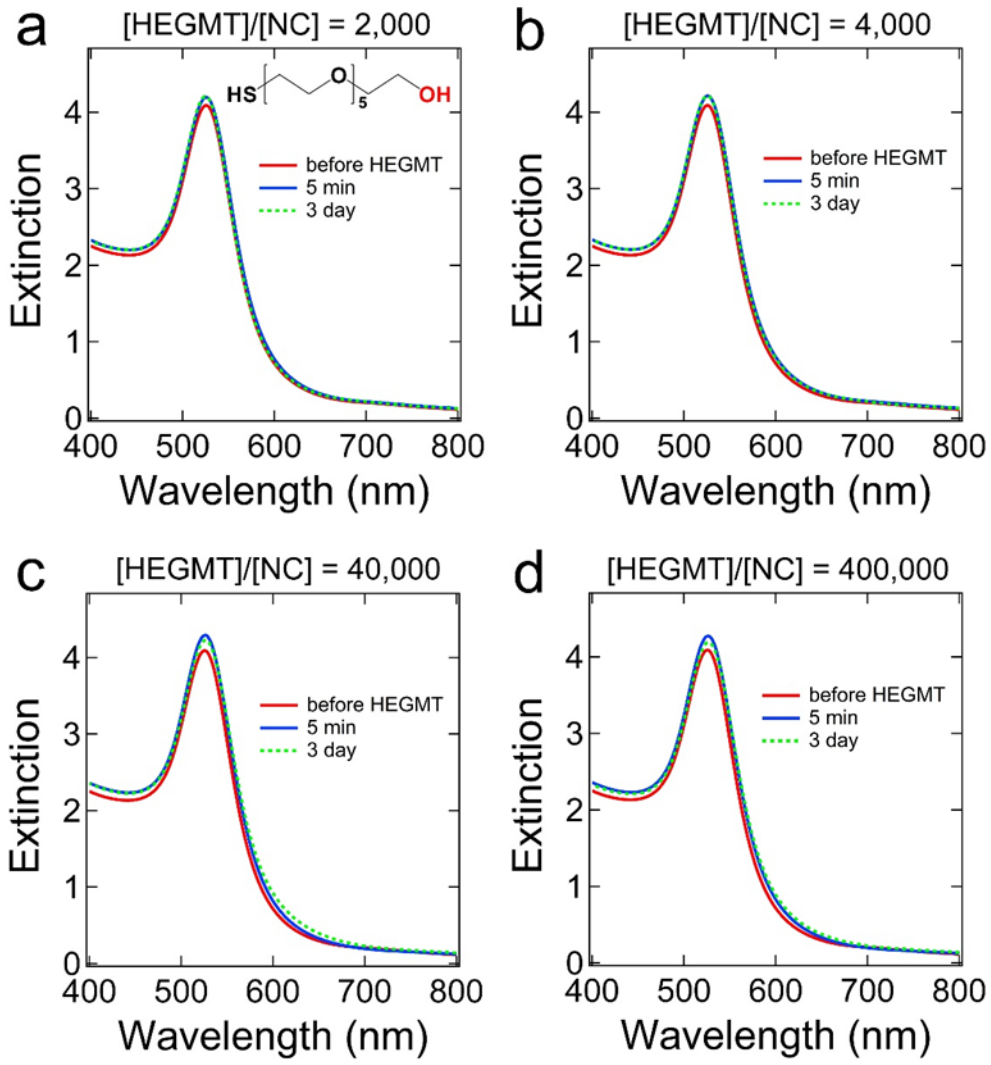

Figure 4.13 Optical extinction spectrum of Au NC before and after adding HEGMT. The structure of HEGMT is shown in the inset. The NCs remain in suspension and show no signs of aggregation over three days.

4.4 Redispersion Mechanism

4.4.1 Oxidation Product of HEGDT

Nuclear magnetic resonance (NMR), mass spectrometry, and pH measurements were used to determine the basic chemistry of the ozone-mediated depolymerization of HEGDT-linked NC precipitates. Given that ozone is a strong oxidant ($E° = 2.08$ V[255]), we reasoned that our brief ozone treatment would quickly oxidize the thiol/thiolate functional groups to sulfonic acids (RSO_3H). Since sulfonates have much weaker binding than thiols to gold[272,273], we expected the NC polymer should lose its cross-linking and fall apart. However, redispersion of the resulting NC monomers and oligomers might require some means of promoting their colloidal stability in water. We presumed that the NCs would be charge stabilized by citrate ions that survived the ozone treatment (discussed in section 4.4.2 and 4.9). In principle, adsorption of disulfonate ions could also assist NC redispersion.

We used NMR and mass spectrometry to determine the products of HEGDT ozonolysis. The ^{1}H NMR spectrum of HEGDT in D_2O (Figure 4.14 a) shows the expected α-methylene triplet at 2.72 ppm, the β-methylene triplet at 3.67 ppm, and the ethylene glycol backbone at 3.69 ppm, in good agreement with the reference spectrum.[274] Ozonation of this solution converts HEGDT to products with a very similar NMR spectrum. The corresponding electrospray ionization mass spectrum (Figure 4.15) exhibits the expected peaks for hexa(ethylene glycol) disulfonic acid (with $[6+H]^+$ at m/z 411, $[6+Na]^+$ at m/z 433, and $[6+K]^+$ at m/z 449) and various further oxidation product (Figure 4.15 molecule 1-5) from breaking the backbone or end group[275,276].

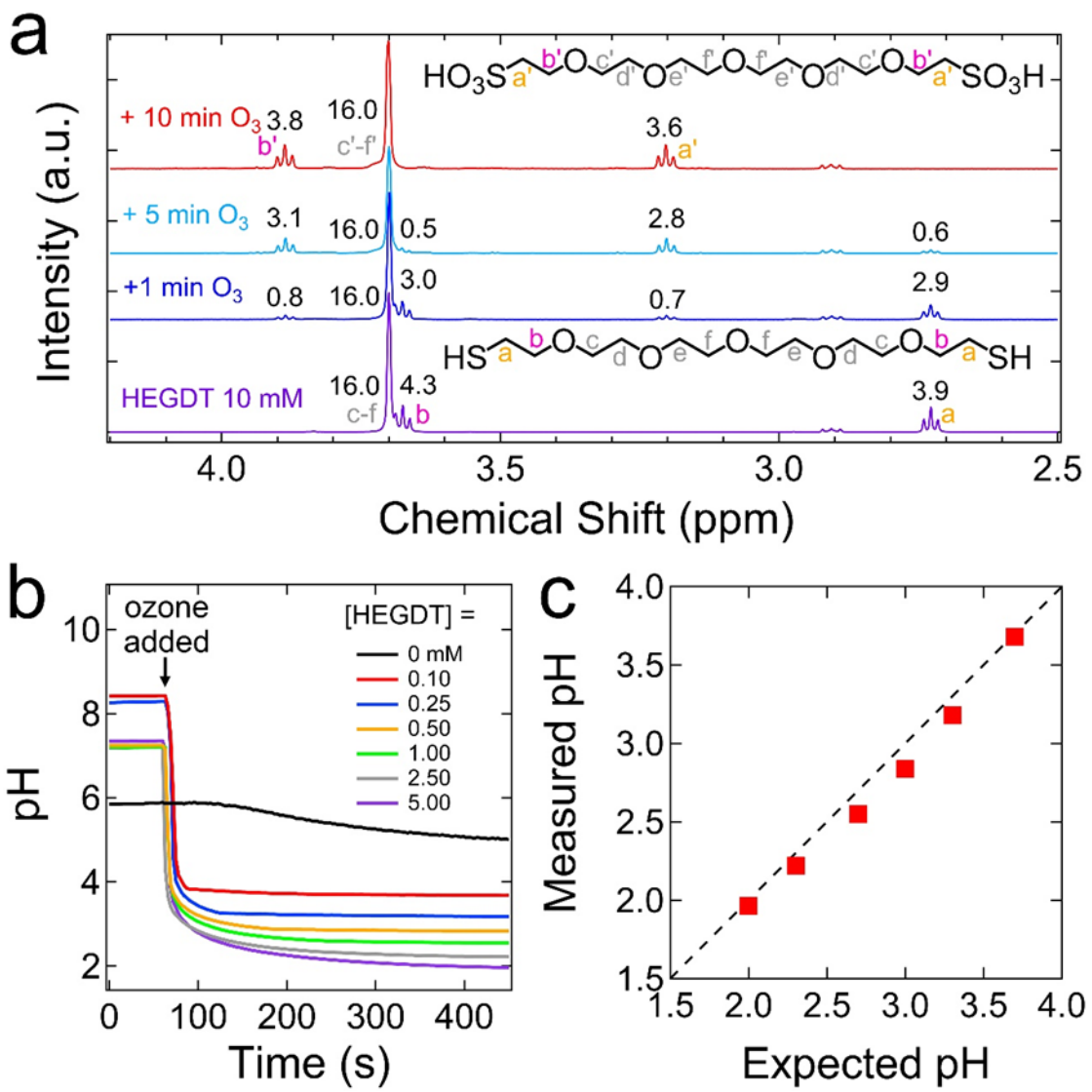

Figure 4.14 Determination of the products of HEGDT oxidation by ozone.

(a) 1H NMR spectra of a 10 mM solution of HEGDT in D_2O after 1, 5, and 10 minutes of ozonation. All peaks agree with HEGDT (before ozonation) or hexa(ethylene glycol) disulfonic acid (after ozonation). Structures of both molecules are inset in the figure. (b) pH versus time during ozonation of various concentrations of HEGDT in water. (c) Measured pH after 10 minutes of ozonation versus the pH expected if ozone oxidizes HEGDT to two equivalents of a strong acid (e.g., HEGDS). The dashed line is a guide to the eye.

Other organic oxidation products such as sulfinic acids (RSO_2H), sulfenic acids (RSOH), or disulfides were not found. Therefore, we assign the main ozonation product to be hexa(ethylene glycol) disulfonic acid (HEGDS) in the NMR spectrum, as labeled in Figure 4.14 a. Quantitative NMR showed a 9% decrease in the ethylene glycol backbone peak area. The α-methylene and β-methylene triplet peak shifted downfield, and the area with respect to the backbone decreased over 10 min ozonation. These observations are in good agreement with the mass spectrum. Qualitative tests with barium ion revealed that sulfate is one of the minor final oxidation products of thiol.

Further evidence for the formation of disulfonic acid comes from pH measurements of ozonated solutions of HEGDT in pure water (Figure 4.14 b-c). The pH change during ozonation is useful for distinguishing between possible dithiol oxidation products because aliphatic sulfonic acids are strong acids in water ($pK_a < 0$)[277,278], whereas sulfinic and sulfenic acids are weak acids (typical pK_a values of ~2 and 10-12, respectively)[279,280] and other possible products (e.g., the cyclic bis(disulfide) and bis(thiosulfonate) dimers) are nonacidic. Sulfinic and sulfenic acids tend to be unstable oxidation intermediates and therefore unlikely final products of ozonation. Immediately upon adding ozone to the solution, we observed a rapid decrease in pH to the value expected if HEGDT was converted to two equivalents of a strong acid (Figure 4.14 b-c). Control experiments without HEGDT showed only a small and slow pH drop might be due to the dissolving of CO_2 in the atmosphere. These data confirm that the primary product of HEGDT ozonation is HEGDS.

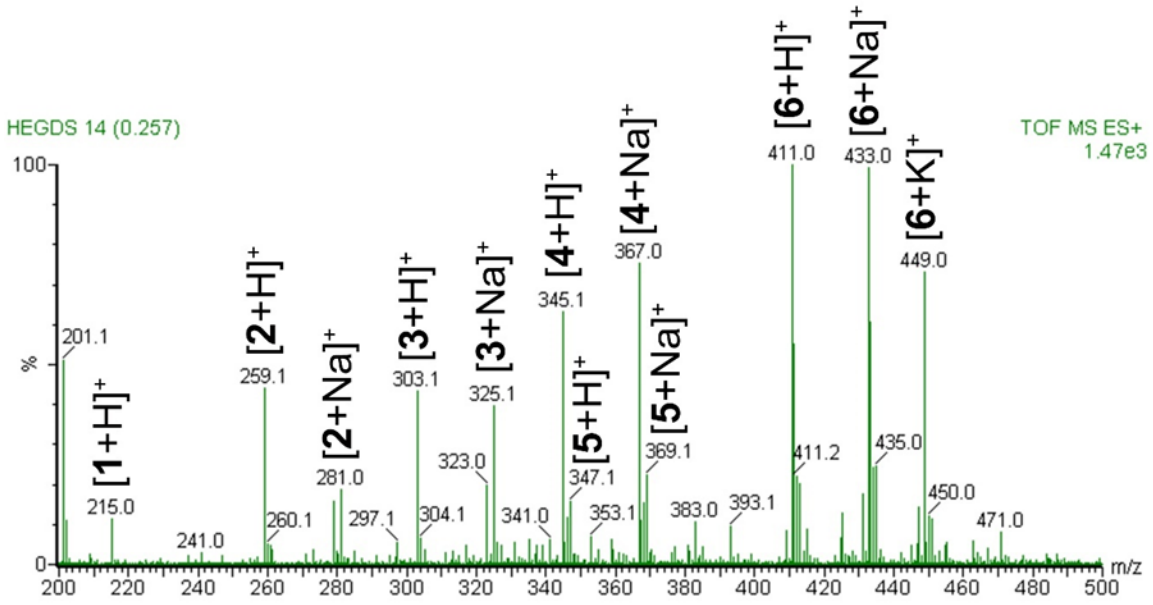

1

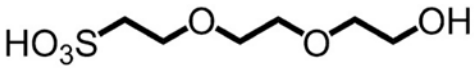

Molecular Weight = 214.23

2

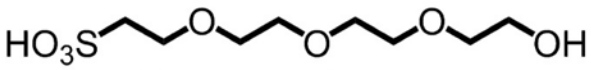

Molecular Weight = 258.29

3

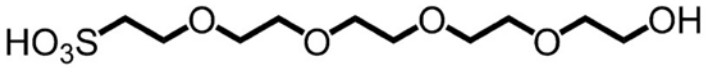

Molecular Weight = 302.34

4

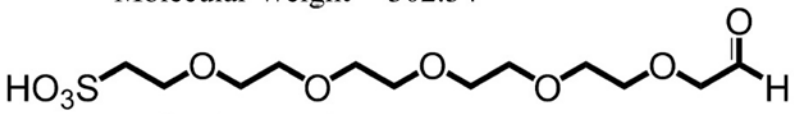

Molecular Weight = 344.38

5

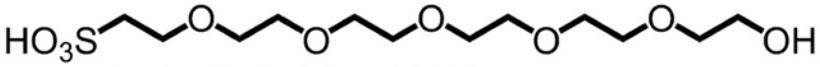

Molecular Weight = 346.39

6

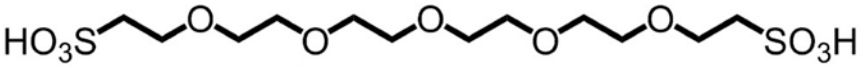

Molecular Weight = 410.45

Figure 4.15 Mass spectrum assignment of HEGDT after 10 minutes of ozonation.

4.4.2 Survival Citrate Concentration

We next determined that the depolymerized NCs redisperse because they are charge stabilized by citrate ions. Quantitative NMR[281] using an internal standard (DSS sodium salt) shows that >98.8% of the free citrate initially present in the solution survives the 5 min ozone treatment to facilitate NC redispersion (Figure 4.16). The quantitative NMR method was first verified by plotting determined [citrate] versus known [citrate]. Linear fits of the data (dashed lines) in Figure 4.16 shows that the citrate concentration decreases by about 1.2% per minute of O_3 bubbling at these conditions. Zeta potential of the redispersed Au NCs (-38.4 mV) was 1.3 mV lower than the as-made Au NCs (-37.1 mV). This indicates the RSO_3^- may also help to stabilize the NCs.

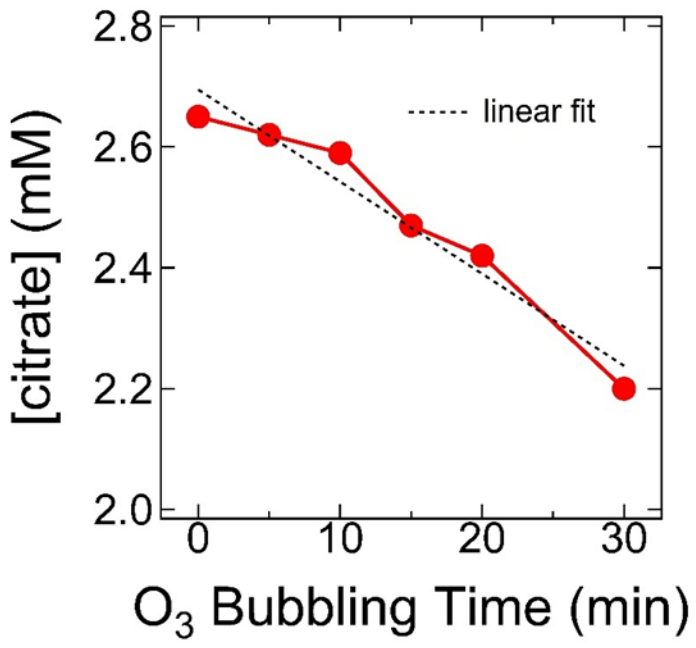

Figure 4.16 The [citrate] in the redispersed Au NCs as a function of ozonation time.

4.4.3 Solution Ozone Concentration

The ozone concentration is determined from the maximum intensity of the Hartley Band[242] at 260 nm, assuming ε_{260} = 2992 M^{-1} cm^{-1}. The ozone concentration reaches 340-360 μM with or without Au NCs after 5 minutes bubbling. The continuous pumping of gaseous ozone (>1 mM in the gas phase, estimated using manufacturer test result) ensured the dissolved ozone was enough to oxidize HEGDT completely at any concentration. The argon sparge is effective at flushing the dissolved ozone out of the solution in less than 1 minute. Thus, we assume the dissolved gas composition of the solution remains unchanged after argon purging.

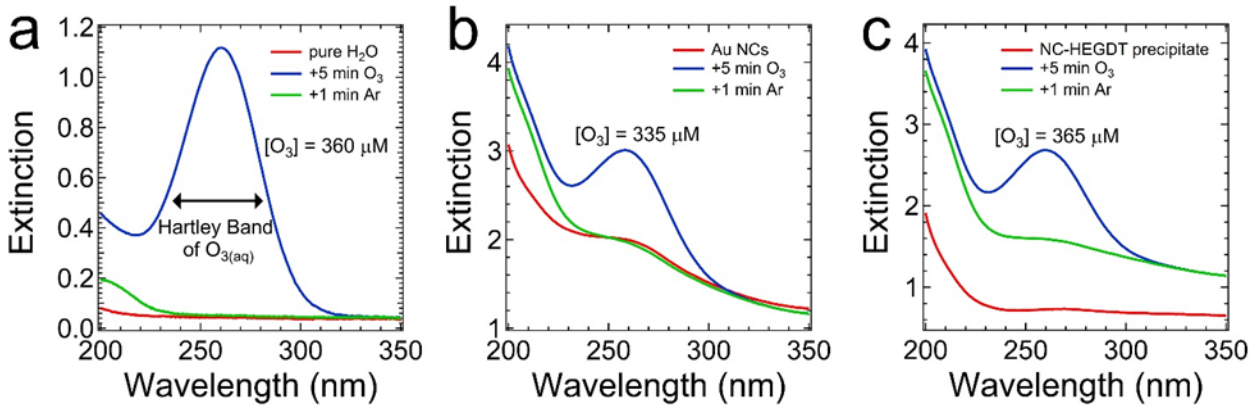

Figure 4.17 Determine the dissolved ozone concentration.

UV optical extinction spectra (200-350 nm) of (a) ultrapure water, (b) Au NCs, and (c) NC-HEGDT precipitates before adding ozone (red curves), immediately after 5 minutes of ozone bubbling (blue curves), and after 5 minutes of ozone and then 1 minute of argon bubbling (green curves).

4.5 Repeatability of the Reversible Aggregation

The aggregation-deaggregation cycle can be repeated multiple times by adding new dithiol to the redispersed NCs to trigger a new round of aggregation. However, more NCs grew (Figure 4.18 b-c) due to the occasional metallic fusion of neighboring NCs over more cycles, which lead to a significant decrease and broaden of the LSPR (Figure 4.18 a).

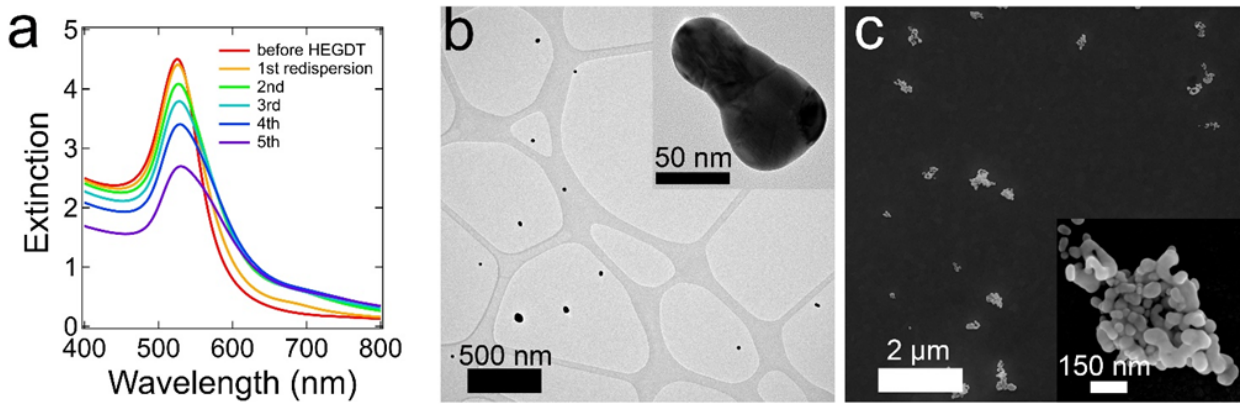

Figure 4.18 Repeatability of the NC aggregation-redispersion cycle.

(a) Extinction spectra for a sample subjected to five cycles of HEGDT-induced precipitation ("hard crashes") and ozone-induced redispersion. Each spectrum was taken 7 days after ozonation. [HEGDT]/[NC] = 4k. (b) A typical TEM image of the NCs suspension after the 5th redispersion. (b) A Typical SEM image of the NCs precipitates after the 5th redispersion. Zoom-in image of fused NCs is shown in the inset.

4.6 Other Dithiols Redispersion

Ozone-mediated redispersion works well with a wide variety of dithiol linkers. HEGDT was the main focus of this study because oligo ethylene glycol dithiols are water soluble, short, and have small Raman scattering cross sections compare to Raman active molecule like biphenyl-4,4'-dithiol (DBDT) (Figure 4.4), making them suitable Raman-silent linkers for the fabrication of high-performance SERS dimer nanoantenna (discussed in section 4.1.2). Our use of HEGDT was inspired by early papers showing that monothiolated glycols yield stable water-soluble Au NCs[282,283,284,285]. However, all other dithiols that we tested worked just as well to some degree as HEGDT, including tetra(ethylene glycol) dithiol, 2,2'-(ethylenedioxy)diethanethiol, pentaerythritol tetrakis(3-mercaptopropionate), and 1,6-hexanedithiol (Figure 4.19). We anticipate that in addition to the small molecule dithiols explored here, ozone will also remove thiolated (bio)polymers from the surface of Au NCs.

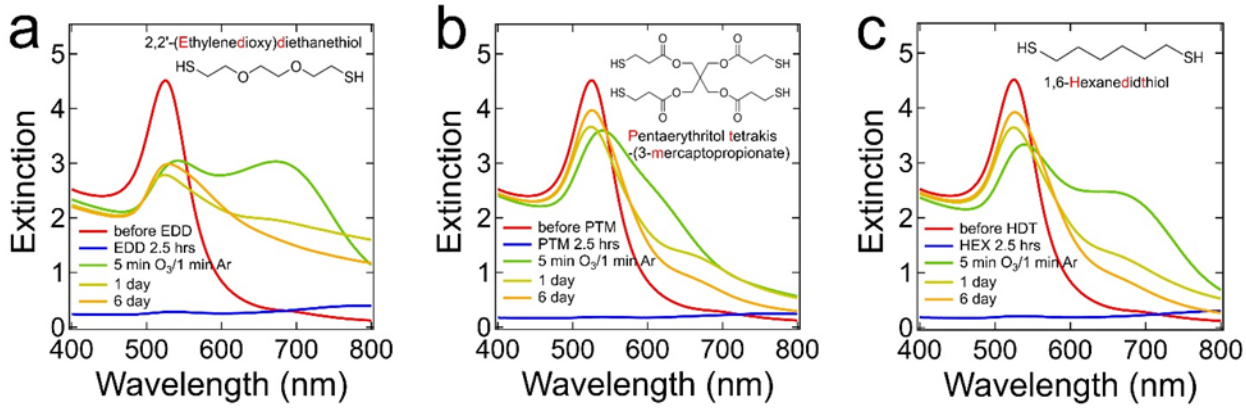

Figure 4.19 Ozone-mediated redispersion of other di/tetra thiols cross-linked Au NCs. Extinction spectra 5 minutes, 1 day, and 67 days after ozonation of NC precipitates made by (a) 2,2'-(ethylenedioxy)diethanethiol, (b) pentaerythritol tetrakis(3-mercaptopropionate), and (c) 1,6-hexanedithiol. In all experiments, [di/tetrathiol]/[Au] = 4000.

4.7 Sterilization of Au NC solution by Ozone

While monitoring the stability of the as made and ozone redispersed NCs solution over several months at room temperature under room light, we observed the growth of a filamentous fungus[286] in the as made Au NCs solution which lead to the precipitation of NCs after 2 months. On the contrary, ozone redispersed or treated as made NCs show no growth of such fungus over at least two years when sealed properly. Some gravitational stratification of the NCs has occurred, but they remain fully suspended – mild shaking of the vial results in complete homogenization of the suspension.

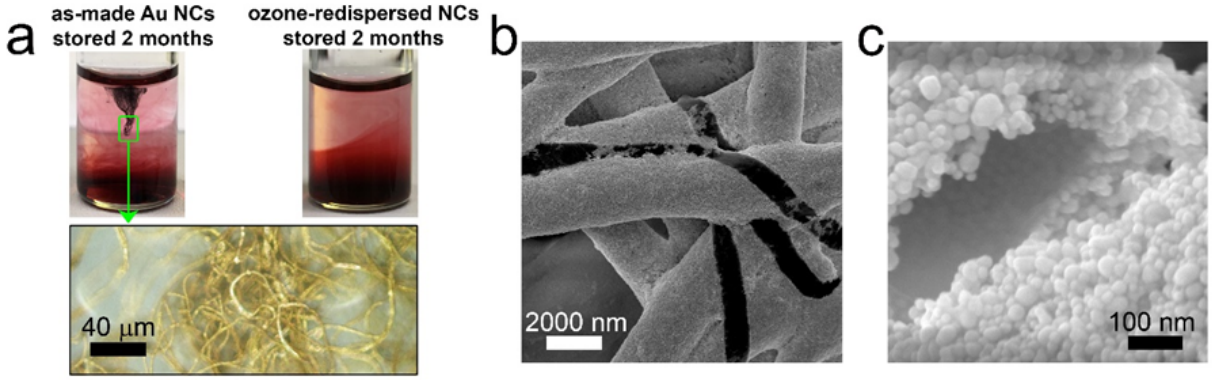

Figure 4.20 Ozone sterilization prevents the growth of fungus in the Au NC suspension. (a) (upper left) Optical image of a suspension of as-made Au NCs stored in ambient conditions for two months. A raft of filamentous fungus is visible floating in the liquid. (bottom) An optical microscope image shows that the filaments are coated in shells of gold. (upper right) Optical image of a suspension of ozonated Au NCs stored in ambient conditions for two months. No fungus is visible. (b) SEM image of the filaments. (c) High-magnification SEM image of a cracked filament, showing a thick coating of Au NCs surrounding an organic or hollow core.

4.8 Monothiol-mediated Redispersion of Au NCs

We evaluated an alternative, ozone-free approach to depolymerizing dithiolate-linked metal NCs by exchanging the dithiols with monothiols. We reasoned that it should be possible to unzip the NC polymers simply by displacing HEGDT with a large excess of an appropriate monothiol[287,288]. NC precipitates made with [HEGDT]/[NC] = 4000 were incubated in solutions of monothiol with [monothiol]/[NC] ratios up to 7.3×10^5.

The best results were obtained using high concentrations (1.8 mM) of aqueous hexa(ethylene glycol) monothiol ($HOCH_2CH_2(OCH_2CH_2)_5SH$), which gave stable red solutions with ~80% NC redispersion after 12 hours sonication at 75 °C (Figure 4.21). Water-ethanol mixtures containing 11-mercaptoundecanoic acid (MUDA) or 16-mercaptohexadecanoic acid (MHDA) dissolved smaller amounts of the precipitate to yield pink solutions. Note that MHDA and MUDA were dissolved in ethanol and formed an emulsion upon injection into the aqueous supernatant, so the MHDA- and MUDA-treated samples were passed through 250 nm pore size syringe filter to minimize light scattering prior to measurement. An unknown number of large NC aggregates were removed from these samples as a result of the filtering. Therefore, the spectra of the MHDA and MUDA samples have an artificially small low-energy absorption tail and actually contain more NC aggregates than the data suggest. Incubation in aqueous 3-mercaptopropionic acid gave no NC redispersion.

We verified that citrate-capped NCs treated with a large excess of any of these monothiols ([monothiol]/[NC] = 7.3×10^5) remained stable in water, suggesting that the poor degree of redispersion is due to an inability of the monothiol to infiltrate and

dissociate the precipitates rather than to peptize the liberated NCs. Although our monothiol trials are by no means exhaustive, it seems that ozonation is a more effective and general method for completely reversing the assembly of covalently cross-linked Au NC precipitates.

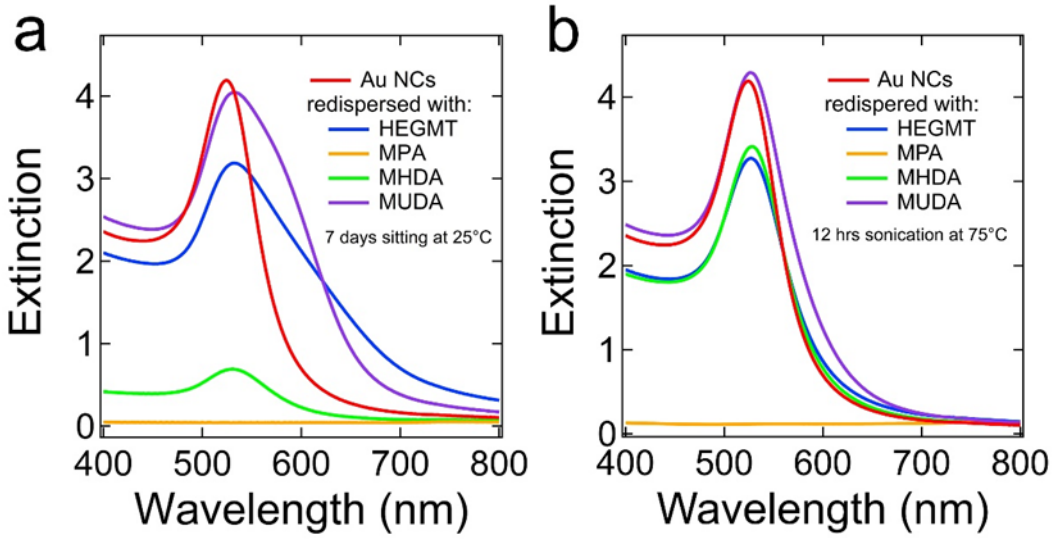

Figure 4.21 Redispersion of NC-HEGDT precipitates using the monothiol exchange.

(a) Typical extinction spectra after adding 9.1 mM HEGMT, mercaptopropionic acid (MPA), 16-mercaptohexadecanoic acid (MHDA), or 11-mercaptoundecanoic acid (MUDA) to the supernatant of a NC-HEGDT precipitate, sonicating for 5 minutes, sparging with argon for 1 minute, and storing unstirred for 7 days at room temperature (all without ozone). The temperature and time mimic the conditions used for ozone-induced redispersion. (b) Spectra after addition of the various monothiols and sonication for 12 hours at 75°C (no ozone). These temperature and sonication conditions are much more extreme than the conditions used for ozonation. In all experiments, [monothiol]/[HEGDT] = 1000.

4.9 Tuning the Redispersion Speed

The ozone-induced redispersion process was proved to be significantly more complicated than anticipated. We found that the redispersion is surprisingly slow (6-7 days) at middle [HEGDT]/[NC], whereas we expected the NCs to redisperse very quickly (seconds to minutes) once the dithiol linkers were oxidized while this is only true at low and high [HEGDT]/[NC]. Temperature, sonication, vortexing, stirring, ozonation time, light, ionic strength, and pH had minimal effect on the rate of redispersion. We also found that the process was equally slow regardless of the stage of aggregation at which the ozonation was performed. This is counterintuitive given that it should be easier to depolymerize small colloidal oligomers formed at the early stage of aggregation than macroscopic polymers precipitate formed in the end.

We then evaluated redispersion in different solutions by thoroughly rinsing batches of NC-HEGDT precipitates ([HEGDT]/[NC] = 4k) with pure water, followed by adding a supernatant of known composition and bubbling ozone in the normal way to find out which component (Table 2) in the solution could be responsible for the slow redispersion. We found that the NCs incompletely redisperse in pure water and 0.1-10 mM solutions of NaCl to form deep blue, stable suspensions of NC aggregates (Figure 4.22 a-b) immediately upon ozonation. However, these NCs redisperse better to stable suspensions of NCs with a minimum number of small clusters upon addition of mM levels of trisodium citrate to the solutions. We observed similarly good NC redispersion in mM solutions of citrate and even better redispersion in solutions containing both mM citrate and salt (Figure 4.22 c-d). However, the redispersion speed went down significantly when both citrate and NaCl

presented comparing to citrate alone. We generally find that complete redispersion of ozonated NC precipitates occurs when the citrate-to-NC molar ratio is higher than ~103.

Table 2 Composition of the redispersion solution.

The speciation of citrate (A^{3-}, AH^{2-}, AH_2^-, and AH_3) is calculated using HySS software[289]. [Cl^-] and [Na^+] are determined according to the precursors added during the Au NCs synthesis. SO_4^{2-} is identified by adding $BaCl_2$ to form $BaSO_4$ precipitates. The [NC] determined by ICP-MS has been checked by nanoparticle tracking analysis (NTA).

Au NCs	Citrate	A^{3-}	AH^{2-}	AH_2^-	AH_3	Cl^-	Na^+
2.5 nM	2.65 mM	0.51 mM	1.97 mM	0.17 mM	0.36 µM	4.19 mM	9.80 mM
ICP-MS	NMR	Calc[289]	Calc[289]	Calc[289]	Calc[289]	Calc	Calc
H^+	SO_4^{2-}	HEGDS	HEGDT	Ozone	Acetone	Acetic acid	Formic acid
1 µM	pM - nM	<10 µM	0 µM	0 µM	0.29 mM	55.5 µM	<0.36 µM
pH	$BaCl_2$	NMR	NMR	UV-Vis	NMR	NMR	NMR

Interestingly, no redispersion occurred at all in mM solutions of HEGDS (adjusted to pH 6), suggesting that the disulfonate actively prevents separation of the NCs (Figure 4.22 f). Possibly HEGDS provides strong enough cross-linking to hold the NCs together in the absence of better ligands such as citrate. Our results show that citrate is the primary peptizing agent in this system and that co-adsorption of chloride probably enhances the dispersibility and stability of the NCs.

Other than redispersing the clean NC-HEGDT precipitates, we also carried out the aggregation-redispersion cycle with the cleaned as made Au NCs (see section 2.2.2 for the cleaning method). Increasing the ionic strength of the cleaned Au NCs solution (decreasing the Debye length of NCs) by adding NaCl was needed to initiate the aggregation mediated

by HEGDT. On the other hand, we studied morphology and linker density differences between the NC-HEGDT precipitates formed at different [HEGDT]/[NC] using TEM and differential scanning calorimetry (DSC). Results of these experiments are still under debate.

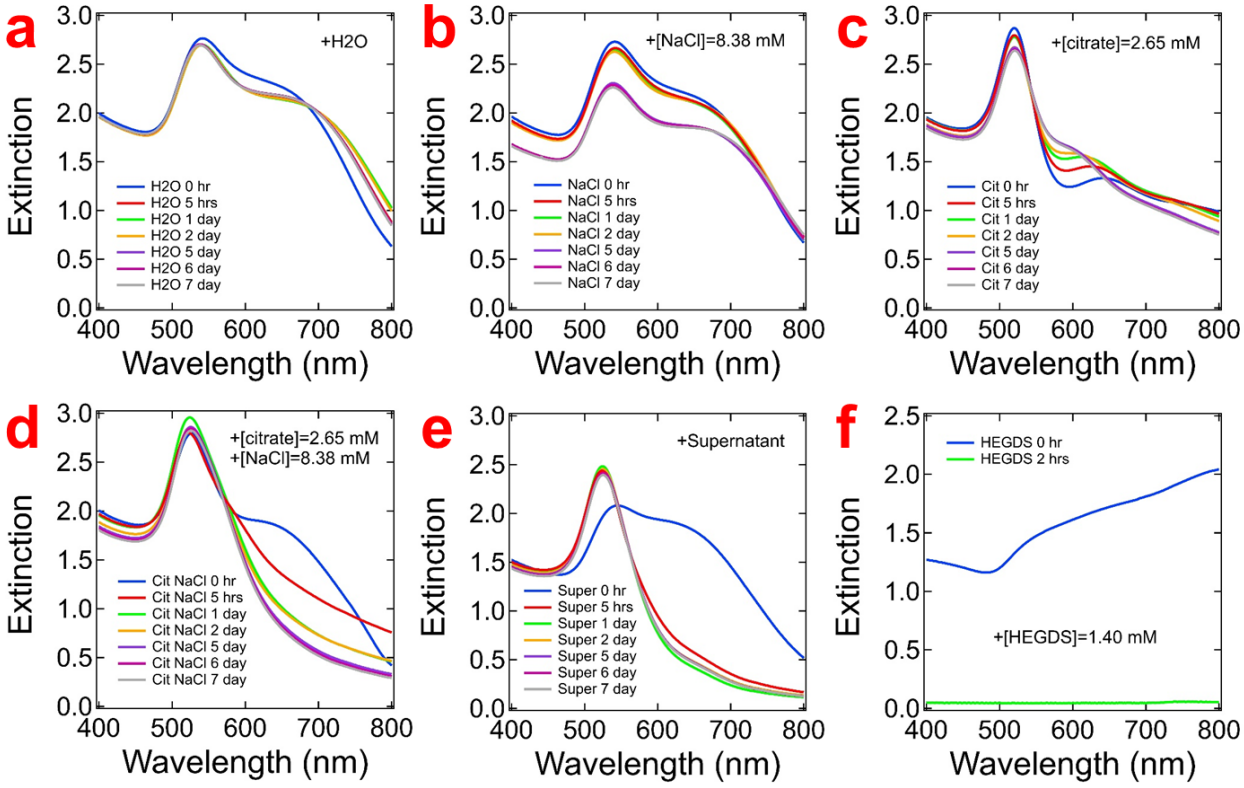

Figure 4.22 Clean NC-HEGDT precipitates redispersion.

Time series of optical extinction spectrum after ozonation of cleaned NC-HEGDT precipitates with (a) H_2O, (b) 8.38 mM NaCl, (c) 2.65 mM Citrate, (d) 8.38 mM NaCl + 2.65 mM Citrate, (e) supernatant of as-made Au NCs, and (f) 1.4 mM HEGDS as the supernatant.

5 Controllable Aggregation towards 100% Dimer

HEGDT has been proved as an excellent linker to initiate the Au NCs aggregation. We attempted to arrest the aggregation process for yielding suspensions of colloidal aggregates with a relatively high percentage of dimers by rapidly oxidizing free thiols using a chemical trigger. Our attempt using ozone nearly completely dissociate the precipitates or small clusters. Controlled dosing of the chemical trigger is needed to avoid the unwanted linker oxidation. Addition of ozone saturated H_2O or using an alternative oxidant H_2O_2 was explored while both ozone and H_2O_2 decomposed over time, which made it hard to determine the exact dosage. In addition, we explored the possibility to use disulfide formation between HEGDT and monothiol (catalyzed by sodium iodide/H_2O_2 or iodine) to stop the aggregation. Our target is to achieve a 3-5% of dimers as higher dimer fractions are unlikely given the statistical nature of this chemistry. We may then isolate and purify these stable dimers using gel electrophoresis to make stable solutions of pure dimers.

The arrested precipitation approach described above is a significant advance in the rational fabrication of colloidal dimers, but this approach results unavoidably in a distribution of NC oligomers. Purification to isolate dimers wastes more than 95% monomers and other clusters in the solution. We reasoned that it should be possible to use the unique plasmonic properties of dimers to convert suspensions of pure monomers to suspensions of pure dimers in a one-pot reaction. In this chapter, our latest efforts on selective plasmonic heating of dimers to trigger passivating surface reaction towards 100% yield of dimers is summarized.

5.1 Plasmon-driven NC dimerization

Current methods to achieve a high percentage of the dimer in solution were reviewed in section 1.4.1. The actual yield of the dimer is usually less than 5% considering the starting number of monomers in these methods though the final solution contains 100% dimer. Differential centrifugation and gel electrophoresis are the two most commonly used methods to separate dimers based on their mass, volume, or charge. On the contrary, we aim to use its optical (plasmonic) property to synthesize dimer in one step with a higher yield (>95%) in the original monomer solution rather than physically separating them. FDTD simulation of two 24 nm Au NCs with a 5 Å gap in water shows its distinct extinction cross section (Figure 5.1) comparing to the monomer. Both monomer and dimer absorb around 525 nm while only dimer absorbs at 640 nm strongly (~150x to monomer) due to its longitudinal plasmon mode under unpolarized light illumination.

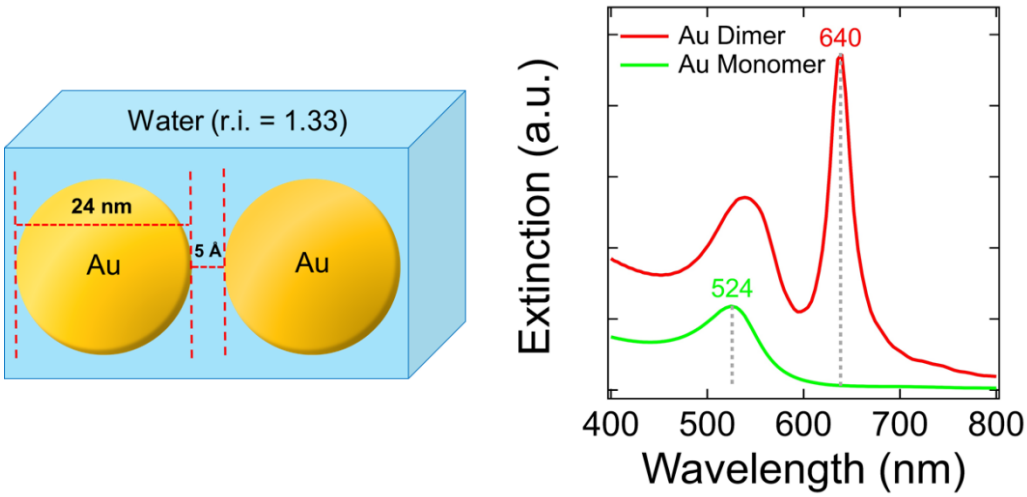

Figure 5.1 Extinction cross section of NC dimer versus monomer by FDTD simulation.

When illuminating the Au NCs solution with a red laser (640 nm), only dimers formed by HEGDT cross-linking could absorb the light strongly by exciting the longitudinal LSPR[290]. Subsequently, the excited plasmon loss energy through various scattering processes and eventually transferring its energy to the local environment in 100 ps to 10 ns[291], which causes significant local heating around the dimer. The HEGDT cross-linking reaction should then yield only dimers if the passivating surface reaction can be triggered by the local heating to prevent further aggregation (Figure 5.2). The efficient and straightforward thiol-ene reaction is selected to passivate the active free thiols on the dimer surface in the following study. We would first prove the principle in the dark by identifying thiol-ene reactions that stop the NC aggregation and keep the NCs indefinitely suspended. Then the reaction rate (temperature dependence) will be determined and adapted to meet a condition such that the reaction is very slow in the dark and only occur around dimers excited by a laser. At last, we will run the process under laser excitation of the longitudinal mode of the NC dimer to achieve quantitative production of dimers.

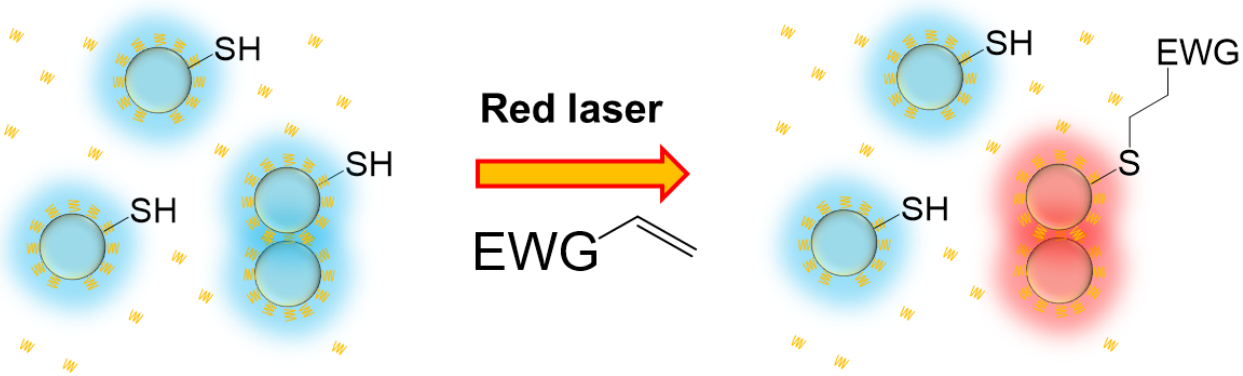

Figure 5.2 Scheme of the plasmon-driven NC dimerization.

5.2 Thiol-ene Click Reactions

Inspired by the well-studied bioconjugation reaction [292] "thiol-maleimide click chemistry[293]", we selected maleimides and acrylates to passivate the surface thiol activated by plasmonic heating on the dimer. Thiol-ene click reaction through thiol-Michael addition pathway is a reaction between thiol and alkene to produce thioether. This reaction is widely used in the molecule and material synthesis[294] (Figure 5.3) given its high yield, high rate, and high selectivity character due to the strong thermodynamic driving force[295].

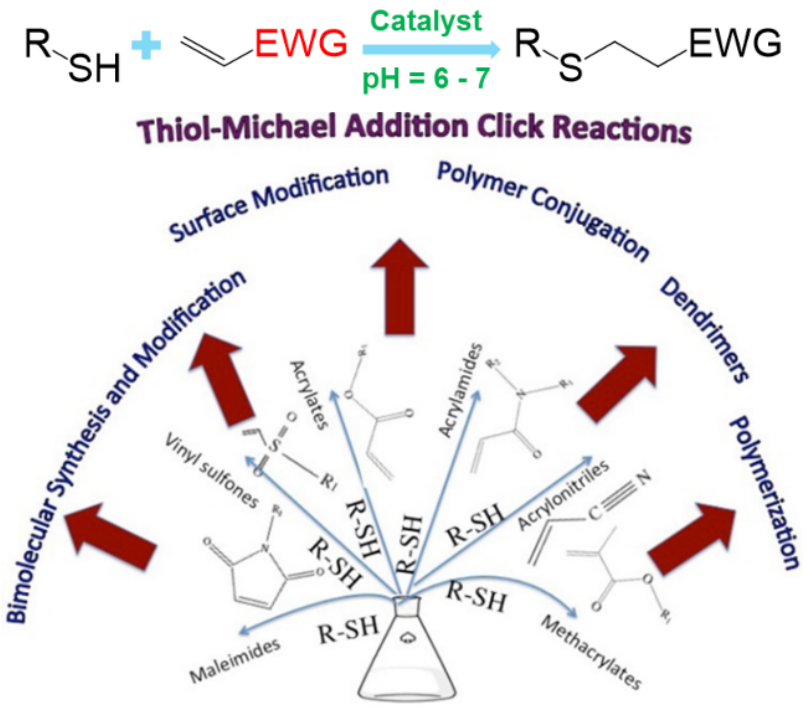

Figure 5.3 Scheme and application of thiol-ene (thiol-Michael addition) reaction. Reprinted with permission from ref 296. © 2014 American Chemical Society.

The scheme and applications of the thiol-Michael addition reaction are presented in Figure 5.3. The reaction mechanism is as follow. Briefly, a basic catalyst B deprotonates the RSH to generate BH^+ and RS^- first. Then the nucleophilic thiolate anion RS^- attacks the electrophilic β-carbon (due to the electron withdrawing group -EWG) on the C=C bond. Finally, the basic intermediate anion extracts a proton from the BH^+ and yields the thiol-Michael addition product along with the regeneration of base catalyst B.

5.2.1 Selection of Enes

Only certain enes that fulfill the all requirements have the potential to passivate thiols considering the reaction environment and condition. First, the molecule must be soluble in water. Second, it cannot facilitate the aggregation of Au NCs by altering the pH/ionic strength of the solution or having an active functional group that binds to Au strongly. Third, the reaction rate needs to be slow enough in the dark, and fast enough when promoted by the local heat. In principle, the more electron deficient the C=C bond (the stronger the -EWG), the more reactive the enes towards thiol-ene reaction[296]. Thus, maleimide reacts the fastest, followed by fumarate, maleate, acrylate/acrylamide, acrylonitrile, crotonate, cinnamate, and methacrylate/methacrylamide[296]. Maleimide (MI), 6-maleimidohexanoic acid (MCA), n-(2-hydroxyethyl)maleimide (HEMI), mPEG-Mal350 (PEGMI350), mPEG-Mal1K (PEGMI1k), mPEG-Mal2K (PEGMI2k), di(ethylene glycol) ethyl ether acrylate (DEE), and 3-sulfopropyl acrylate potassium salt (SAC) were selected for the initial study (Figure 5.4) based on the above rules.

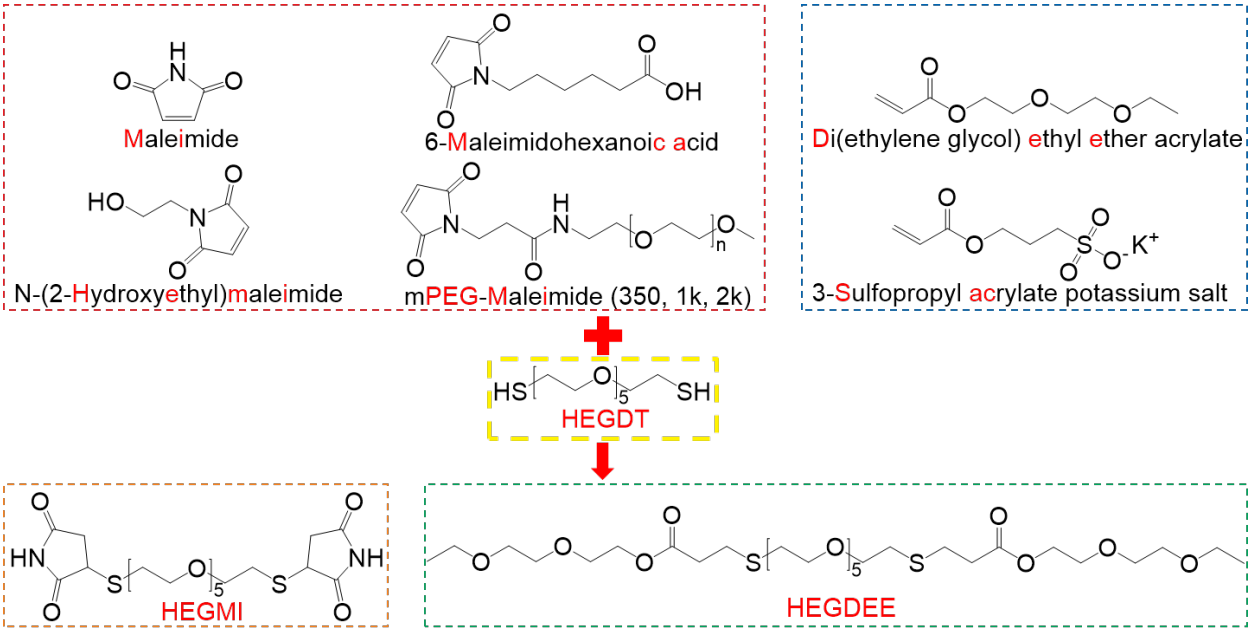

Figure 5.4 Molecular structure and abbreviation of the selected enes and thiol-enes.

5.2.2 Determine Reaction Kinetics

The click reactions between HEGDT and maleimides/acrylates ("X" will be used to represent all enes in the following text) were verified by quantitative NMR. Figure 5.6 gives examples of HEGDT reacting with MI or DEE at a 1 : 2 molar ratio to produce HEGMI or HEGDEE. The dramatic shift and decrease of the peaks representing protons (colored H in Figure 5.6) on the C=C bond were used as evidence to confirm the click reactions. In all cases, we ran NMR ~30 minutes after mixing 20 mM of X and 10 mM of HEGDT. Thus, the reaction rate of different X and HEGDT at room temperature can be qualitatively compared. MI, HEMI, and MCA react fastest with HEGDT followed by PEGMI350, PEGMI1k, DEE, SAC, and PEGMI2k. This result is consistent with the reactivity prediction based on the electron deficiency of the C=C in section 5.2.1. We also find out that the longer the carbon/EG chain,

the slower the reaction. More quantitative NMR studies are needed to determine the rate constant and activation energy of X + HEGDT reaction in the future.

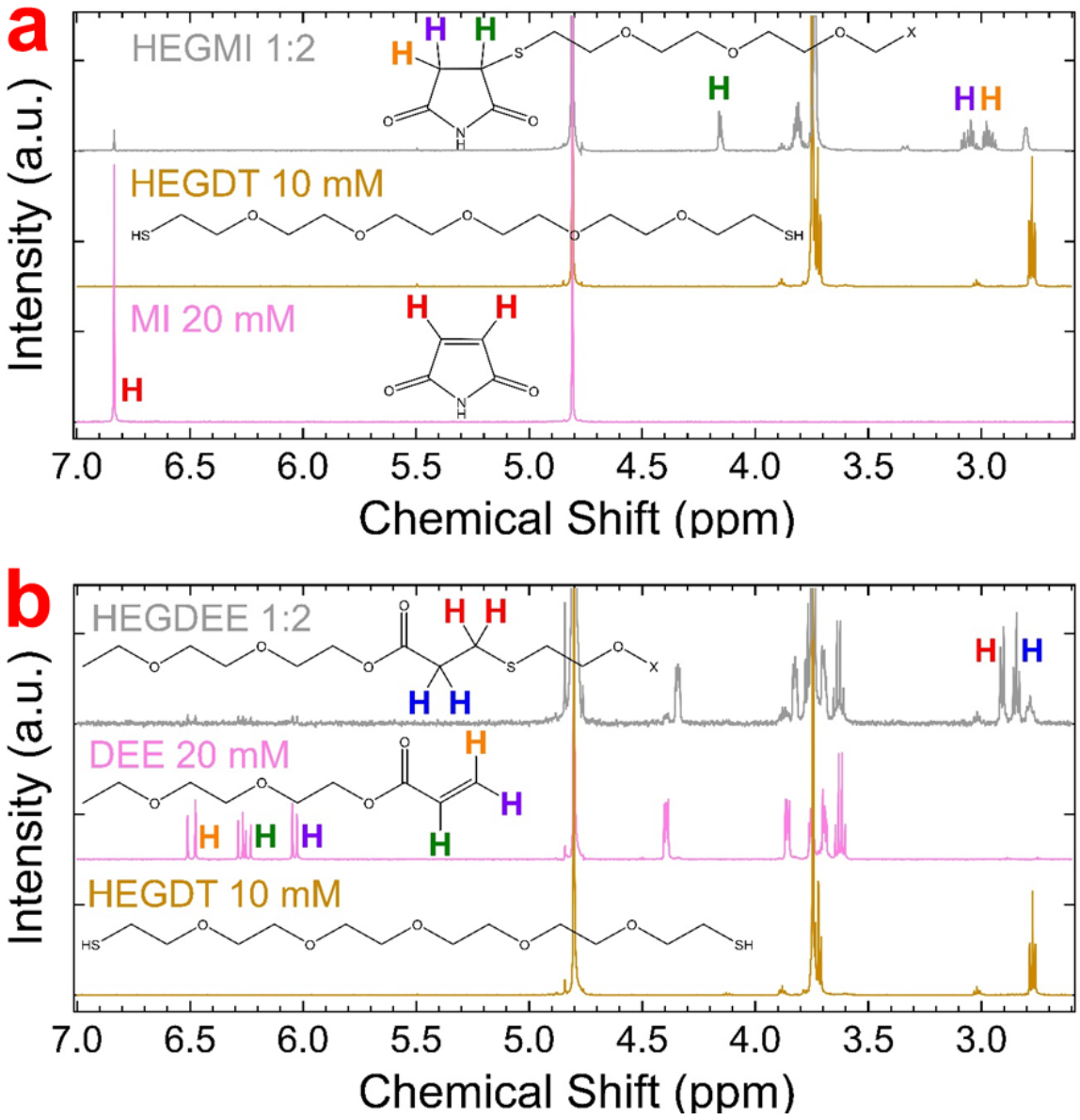

Figure 5.5 Quantitative NMR study of thiol-ene click reaction.

1H NMR spectrum of 10 mM HEGDT, 20 mM of (a) MI or (b) DEE in D_2O, a mixture of HEGDT with MI or DEE after 30 minutes. Structure of the molecule is inserted in the figure. Protons shift the most during thiol-ene click reaction are marked with color.

5.2.3 Thiol-ene Reaction in Au NCs solution

X and HEGDT were added to the Au NCs solution to test the effect of thiol-ene reaction on the aggregation process. Four variables were tested, including the type of X, [NC], and [X] using three methods (discussed in section 2.4.4). All other conditions, including the total volume of the solution, [HEGDT], pH, and temperature are kept the same. Any concentration (μM to mM) of X alone did not change the Au NCs in the solution. In Table 3, red color means adding X speed up the aggregation of Au NCs. On the other hand, blue color means adding X slow down the aggregation, and white color means the X does not impact the aggregation speed. Ideally, the most active maleimides should stop aggregation effectively. However, only long-chain maleimides can slow down the HEGDT cross-linking under certain conditions (blue color). This indicates the N in the maleimides might be able to link NCs as well. Thus, a long "tail" is needed to isolate the N to reduce its activity.

We can choose the conditions that have white (no impact) or blue color (slow down) for the future study involving laser illumination. In summary, none of the X stops aggregation completely when adding after HEGDT (method A). PEGMI350, PEGMI1k, PEGMI2k, HEMI, and SAC stop aggregation almost completely when adding to NC solution before HEGDT (method B) or mixing with HEGDT before adding to NC solution (method C). More importantly, long chain maleimides and acrylates slow down or show no impact on the aggregation rate using method A, thus promising for the following study. After all, X should stop the aggregation only under local plasmonic heating, not at room temperature. However, it should at least not facilitate the aggregation.

Table 3 Summary of thiol-ene reaction in Au NC solution.

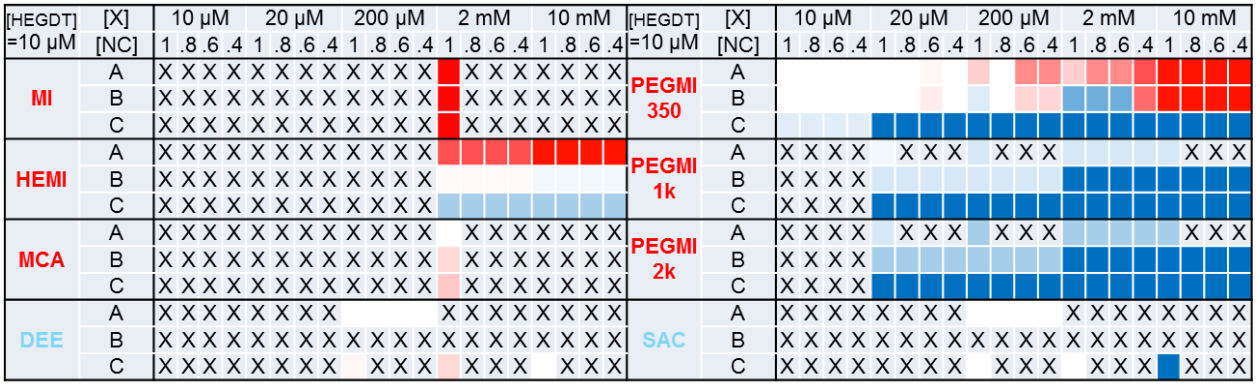

5.3 Future Experiment Setup

We machined a cuvette holder and assembled the setup (Figure 5.6 b) for the following study involving laser illumination. The setup consists of the cuvette holder with water supply, mini stir plate (Thermo Scientific, Cimarec-i), chiller (Grant Instruments, LT ecocool 150), epoxy tip thermocouple (OMEGA, 5TC-PVC-E-24-180), temperature controller (J-KEM Scientific, The Quad), broadband LED light source (Thorlabs, MBB1L3), and fiber spectrometer (Ocean Optics, USB4000-UV-VIS). The incoming laser was spread (Figure 5.6 a) through a lens (Thorlabs, LA1951-D-N-BK7) to illuminate the whole front window of the cuvette containing the Au NCs solution.

To test the setup and our hypothesis of plasmonic heating, we illuminated the as-made NCs solution at two different wavelengths in the cuvette. We propose that dimers absorb ~150x stronger than monomers at its longitudinal plasmon peak based on the FDTD simulation in section 5.1. While we cannot prove it directly by pumping the longitudinal plasmon mode of pure dimers versus monomers and monitoring the solution temperature

since we don't have a solution containing 100% dimer. On the other hand, we can test this idea by pumping the monomers at its LSPR peak versus where it absorbs weakly.

Thus, we pumped the as-made Au NCs solution at 530 nm (peak ~527 nm) or 650 nm (where dimers absorb not monomers) for 1 hour at 2 mW/cm^2 average laser power (200 fs per pulse, 80 MHz rep rate). Later, the temperature of the solution pumped at 530 nm raised from 19 °C to 50 °C while the 650 nm remained unchanged. In addition, the extinction spectrum of Au NCs before and after illumination remained unchanged at both wavelengths. The result of the preliminary experiment shows the wavelength-dependent on the plasmonic heating.

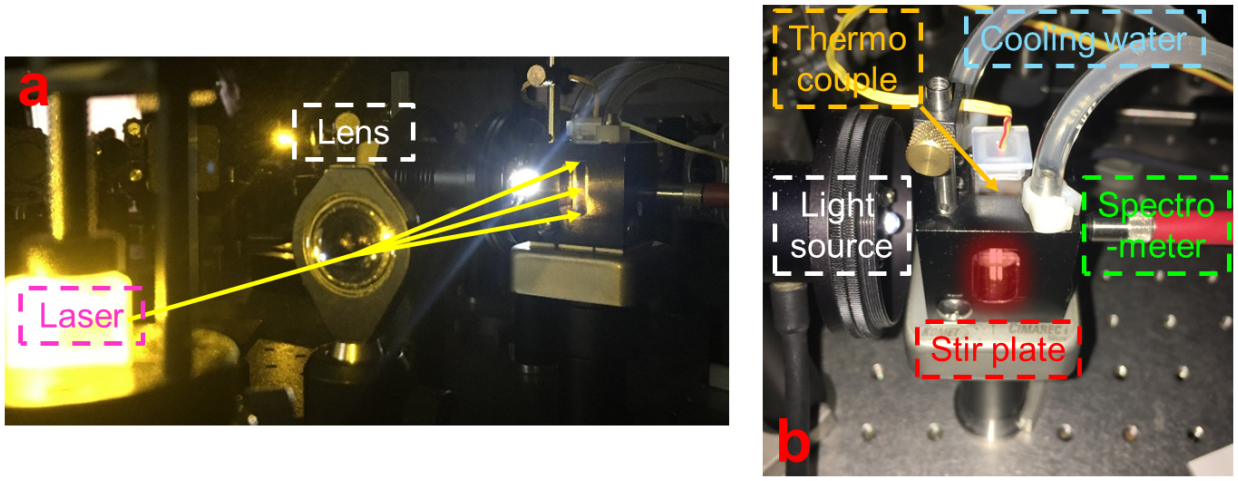

Figure 5.6 Experiment setup with laser illumination.

(a) Front view of the setup shows the expanded laser illuminating the front window of the cuvette holder. (b) Top view of the cuvette holder with temperature control, solution temperature monitor, stir, and in-situ real-time extinction spectrum monitor functions.

6 Summary and Conclusions

In this study, we developed two nantennas platforms by stochastically assembly of NCs and atomic layer deposition (ALD) towards steady-state and time-resolved SERS study of important chemical transformation and charge injection in photocatalysis processes. Homemade Ag NCs followed the well-established procedure[234,] and commercial Au NCs were selected as the building block of the nantennas. We built the platform I of $Ag/TiO_2/N719/TiO_2$ to perform a proof-of-concept study of charge transfer from dye molecules to semiconductor metal oxide. Preliminary steady-state SERS spectra of N719 adsorbed onto ~2 nm thick TiO_2 coatings on unlinked "dimers" (formed stochastically during drying rather than deliberately via chemical linkage) showed an electronic Raman continuum, suggesting enhanced Raman scattering by the LSPR. Similarly, platform II of $Au/TiO_2/DBDT/Al_2O_3$ was built and verified by steady-state SERS to show the versatility of our core/shell/molecule platform.

Use of the chemically linked NC dimers will significantly increase the throughput of the spectroscopy, which is necessary to perform the desired time-resolved studies of charge injection at the single-molecule level. The initial attempt of controllable dimerization using simple alkane dithiols revealed the importance of the solubility/length/concentration of the dithiol and surface cleanness/chemical resistance of the NCs. We attempted to remove the PVP on Ag NCs using various chemical treatment and physical methods while could not eliminate it completely. The proprietary surfactant found on the commercial Au NCs drove us to synthesize the "simple" citrate-capped Au NCs in our lab for the following controllable aggregation study.

The first stage of the "controllable" effort was made to select the right chemical linker to trigger the aggregation process. HEGDT, which has been selected for the entire study, exhibits excellence water solubility and relatively low Raman response. The redshift of the surface plasmon peak of Au NCs was observed immediately upon addition of HEGDT followed by the formation of NC-dithiolate polymer. Micron-scale NC-HEGDT precipitates with more than thousands of particles stacked together were observed at the bottom of the vial and confirmed via TEM after 3 hrs. This NC-dithiolate polymer showed a nearly featureless Raman spectrum and compatible with Al_2O_3 ALD process. On the other hand, samples prepared in the presence of Raman reporter molecules such as biphenyl-4-4'-dithiol (DBDT) exhibited strong SERS spectra, indicating that reporter molecules readily found adsorption sites within the hot spots. Thus, these HEGDT-linked Au NCs are promising for single-molecule SERS studies. We have developed cryo/cooling-TEM as a method to image dimers and other plasmonic assemblies with minimal beam-induced sample damage. Commonly seen electron beam effect (local heat) make accurate gap distance measurement impossible as the particles expand and merge with each other (gap fusion) upon illumination. Our method involves cooling/cryo holder combining with large spot size, and small condenser lens aperture can resolve the problem, which allows accurate measurement of inter-NC spacing (5.5 ± 1 Å for the HEGDT linked dimers).

The second stage of the project requires a stopping reagent which pauses the aggregation process when the yield of dimers is the highest. After exploring disulfide formation with iodine and NaI/H_2O_2 catalysts, we found that ozone was very effective at selectively oxidizing the dithiols to disulfonic acids resulting in the destruction of the dithiol linkers and complete redispersion of the Au NCs to back to monomers in the

solution. We have studied the aggregation and redispersion process with optical absorption spectroscopy, FT-IR, DLS, SAXS, XPS, TEM, NMR, mass spectrometry, zeta potential, and pH measurements to prove our hypothesis and establish the chemistry. The goal is to oxidize only the free thiol groups while preserving the bound thiolates, thereby stop the polymerization reaction and yielding a stable solution of dimers (and other small oligomers) that can be cast onto surfaces to serve as SERS nantenna.

NMR and pH data proved that disulfonate is the major product of ozonation. TEM showed that the NC size and shape were nearly unaffected by ozonation. [HEGDT] to [NC] ratio was proved to govern the aggregation and redispersion speed by changing the effective linking sites. Redispersion occurs as long as the concentration of the peptizing agent (citrate in this case) is sufficiently high. The aggregation-deaggregation cycle worked with all of the dithiol linkers tested and can be repeated multiple times while the loss of NCs or alteration of NC size or shape were observed over more cycles. Redispersion by the exchange of dithiols with monothiols proved to be less effective and less clean than ozonation. Selective linker oxidation is a general way to reverse the aggregation of covalently linked Au NCs. However, redispersion became fast (seconds) albeit incomplete when carried out in pure water or solutions of trisodium citrate without NaCl, instead of the original NC reaction solution. Due to the complex composition of the reaction solution, we have not yet determined why the clean NC-HEGDT precipitates redispersion is either slow and complete or fast and incomplete. This mystery illustrates the “simple” ozone-mediated redispersion of the NC-HEGDT precipitates needs more in-depth investigations.

Finally, we explored the possibility of synthesis dimers at 100% yield in one step by selectively triggering the surface passivating reaction under local plasmonic heating. The

PEGylated maleimides and acrylates were identified as the most active species to slow down or stop dithiol-induced aggregation possibly via the thiol-ene click reaction. Pumping the Au NCs at 530 nm increased the temperature to 50°C due to plasmonic heating while no temperature increased at 650 nm. Combining the targeted laser illumination of only dimers and rational tuning of the aggregation based on the rate constants determined by NMR, we are moving towards synthesizing 100% dimers in the near future.

Bibliography

[1] Bohm, D., & Pines, D. (1953). A collective description of electron interactions: III. Coulomb interactions in a degenerate electron gas. *Physical Review*, *92*(3), 609.

[2] Maier, S. A. (2007). *Plasmonics: fundamentals and applications*. Springer Science & Business Media.

[3] Chen, F. F. (2012). *Introduction to plasma physics*. Springer Science & Business Media.

[4] Thompson, W. B. (2013). *An introduction to plasma physics*. Elsevier.

[5] Paudel, H. P., Safaei, A., & Leuenberger, M. N. (2017). *Nanoplasmonics in Metallic Nanostructures and Dirac Systems*. InTech.

[6] Barnes, W. L., Dereux, A., & Ebbesen, T. W. (2003). Surface plasmon subwavelength optics. *nature*, *424*(6950), 824.

[7] Biagioni, P., Huang, J. S., & Hecht, B. (2012). Nanoantennas for visible and infrared radiation. *Reports on Progress in Physics*, *75*(2), 024402.

[8] Giannini, V., Fernández-Domínguez, A. I., Heck, S. C., & Maier, S. A. (2011). Plasmonic nanoantennas: fundamentals and their use in controlling the radiative properties of nanoemitters. *Chemical reviews*, *111*(6), 3888-3912.

[9] Zuloaga, J., & Nordlander, P. (2011). On the energy shift between near-field and far-field peak intensities in localized plasmon systems. *Nano letters*, *11*(3), 1280-1283.

[10] Kats, M. A., Yu, N., Genevet, P., Gaburro, Z., & Capasso, F. (2011). Effect of radiation damping on the spectral response of plasmonic components. *Optics express*, *19*(22), 21748-21753.

[11] Alabastri, A., Tuccio, S., Giugni, A., Toma, A., Liberale, C., Das, G., ... & Zaccaria, R. (2013). Molding of plasmonic resonances in metallic nanostructures: Dependence of the non-linear electric permittivity on system size and temperature. *Materials*, *6*(11), 4879-4910.

[12] Mie, G. (1908). Beiträge zur Optik trüber Medien, speziell kolloidaler Metallösungen. *Annalen der physik*, *330*(3), 377-445.

[13] Bohren, C. F., & Huffman, D. R. (2008). *Absorption and scattering of light by small particles*. John Wiley & Sons.

[14] Mayer, K. M., & Hafner, J. H. (2011). Localized surface plasmon resonance sensors. *Chemical reviews*, *111*(6), 3828-3857.

[15] Fröhlich, H., & Sack, R. (1944). Dielectric properties of dipolar substances. *Proceedings of the Royal Society of London. Series A. Mathematical and Physical Sciences*, *182*(991), 388-403.

[16] Kreibig, U., & Vollmer, M. (2013). *Optical properties of metal clusters* (Vol. 25). Springer Science & Business Media.

[17] Semenenko, V., Schuler, S., Centeno, A., Zurutuza, A., Mueller, T., & Perebeinos, V. (2018). Plasmon–Plasmon Interactions and Radiative Damping of Graphene Plasmons. *ACS Photonics*, *5*(9), 3459-3465.

[18] Sönnichsen, C., Franzl, T., Wilk, T. V., von Plessen, G., Feldmann, J., Wilson, O. V., & Mulvaney, P. (2002). Drastic reduction of plasmon damping in gold nanorods. *Physical review letters*, *88*(7), 077402.

[19] Brown, A. M., Sundararaman, R., Narang, P., Goddard III, W. A., & Atwater, H. A. (2015). Nonradiative plasmon decay and hot carrier dynamics: effects of phonons, surfaces, and geometry. *Acs Nano*, *10*(1), 957-966.

[20] Sundararaman, R., Narang, P., Jermyn, A. S., Goddard III, W. A., & Atwater, H. A. (2014). Theoretical predictions for hot-carrier generation from surface plasmon decay. *Nature communications*, *5*, 5788.

[21] Voisin, C., Del Fatti, N., Christofilos, D., & Vallée, F. (2001). Ultrafast electron dynamics and optical nonlinearities in metal nanoparticles.

[22] Sarhan, R. M., Koopman, W., Schuetz, R., Schmid, T., Liebig, F., Koetz, J., & Bargheer, M. (2019). The importance of plasmonic heating for the plasmon-driven photodimerization of 4-nitrothiophenol. *Scientific reports*, *9*(1), 3060.

[23] Yu, Y., Williams, J. D., & Willets, K. A. (2018). Quantifying photothermal heating at plasmonic nanoparticles by scanning electrochemical microscopy. *Faraday discussions*, *210*, 29-39.

[24] Khosravi Khorashad, L., Besteiro, L. V., Wang, Z., Valentine, J., & Govorov, A. O. (2016). Localization of excess temperature using plasmonic hot spots in metal nanostructures: combining nano-optical antennas with the fano effect. *The Journal of Physical Chemistry C*, *120*(24), 13215-13226.

[25] Amendola, V., Pilot, R., Frasconi, M., Marago, O. M., & Iati, M. A. (2017). Surface plasmon resonance in gold nanoparticles: a review. *Journal of Physics: Condensed Matter*, *29*(20), 203002.

[26] Blaber, M. G., Arnold, M. D., & Ford, M. J. (2010). A review of the optical properties of alloys and intermetallics for plasmonics. *Journal of Physics: Condensed Matter*, *22*(14), 143201.

[27] Gans, R. V. (1912). Über die form ultramikroskopischer goldteilchen. *Annalen der Physik*, *342*(5), 881-900.

[28] Mahmoud, M. A., Chamanzar, M., Adibi, A., & El-Sayed, M. A. (2012). Effect of the dielectric constant of the surrounding medium and the substrate on the surface plasmon resonance spectrum and sensitivity factors of highly symmetric systems: silver nanocubes. *Journal of the American Chemical Society*, *134*(14), 6434-6442.

[29] Fofang, N. T., Park, T. H., Neumann, O., Mirin, N. A., Nordlander, P., & Halas, N. J. (2008). Plexcitonic nanoparticles: plasmon− exciton coupling in nanoshell− J-aggregate complexes. *Nano letters*, *8*(10), 3481-3487.

[30] Aruda, K. O., Tagliazucchi, M., Sweeney, C. M., Hannah, D. C., Schatz, G. C., & Weiss, E. A. (2013). Identification of parameters through which surface chemistry determines the lifetimes of hot electrons in small Au nanoparticles. *Proceedings of the National Academy of Sciences*, *110*(11), 4212-4217.

[31] Link, S., & El-Sayed, M. A. (1999). Size and temperature dependence of the plasmon absorption of colloidal gold nanoparticles. *The Journal of Physical Chemistry B*, *103*(21), 4212-4217.

[32] Scholl, J. A., Koh, A. L., & Dionne, J. A. (2012). Quantum plasmon resonances of individual metallic nanoparticles. *Nature*, *483*(7390), 421.

[33] Jain, P. K., & El-Sayed, M. A. (2010). Plasmonic coupling in noble metal nanostructures. *Chemical Physics Letters*, *487*(4-6), 153-164.

[34] Dhawan, A., Norton, S. J., Gerhold, M. D., & Vo-Dinh, T. (2009). Comparison of FDTD numerical computations and analytical multipole expansion method for plasmonics-active nanosphere dimers. *Optics express*, *17*(12), 9688-9703.

[35] Yang, Z., Li, Q., Ruan, F., Li, Z., Ren, B., Xu, H., & Tian, Z. (2010). FDTD for plasmonics: Applications in enhanced Raman spectroscopy. *Chinese Science Bulletin*, *55*(24), 2635-2642.

[36] Vial, A., Laroche, T., Dridi, M., & Le Cunff, L. (2011). A new model of dispersion for metals leading to a more accurate modeling of plasmonic structures using the FDTD method. *Applied Physics A*, *103*(3), 849-853.

[37] Yang, W. H., Schatz, G. C., & Van Duyne, R. P. (1995). Discrete dipole approximation for calculating extinction and Raman intensities for small particles with arbitrary shapes. *The Journal of chemical physics*, *103*(3), 869-875.

[38] Jain, P. K., Eustis, S., & El-Sayed, M. A. (2006). Plasmon coupling in nanorod assemblies: optical absorption, discrete dipole approximation simulation, and exciton-coupling model. *The Journal of Physical Chemistry B*, *110*(37), 18243-18253.

[39] Amendola, V., Bakr, O. M., & Stellacci, F. (2010). A study of the surface plasmon resonance of silver nanoparticles by the discrete dipole approximation method: effect of shape, size, structure, and assembly. *Plasmonics*, *5*(1), 85-97.

[40] Coggon, J. H. (1971). Electromagnetic and electrical modeling by the finite element method. *Geophysics*, *36*(1), 132-155.

[41] McMahon, J. M., Henry, A. I., Wustholz, K. L., Natan, M. J., Freeman, R. G., Van Duyne, R. P., & Schatz, G. C. (2009). Gold nanoparticle dimer plasmonics: finite element method calculations of the electromagnetic enhancement to surface-enhanced Raman spectroscopy. *Analytical and bioanalytical chemistry*, *394*(7), 1819-1825.

[42] Zhao, J., Pinchuk, A. O., McMahon, J. M., Li, S., Ausman, L. K., Atkinson, A. L., & Schatz, G. C. (2008). Methods for describing the electromagnetic properties of silver and gold nanoparticles. *Accounts of chemical research*, *41*(12), 1710-1720.

[43] Koh, A. L., Bao, K., Khan, I., Smith, W. E., Kothleitner, G., Nordlander, P., ... & McComb, D. W. (2009). Electron energy-loss spectroscopy (EELS) of surface plasmons in single silver nanoparticles and dimers: influence of beam damage and mapping of dark modes. *ACS nano*, *3*(10), 3015-3022.

[44] Nelayah, J., Kociak, M., Stéphan, O., de Abajo, F. J. G., Tencé, M., Henrard, L., ... & Colliex, C. (2007). Mapping surface plasmons on a single metallic nanoparticle. *Nature Physics*, *3*(5), 348.

[45] Schaffer, B., Hohenester, U., Trügler, A., & Hofer, F. (2009). High-resolution surface plasmon imaging of gold nanoparticles by energy-filtered transmission electron microscopy. *Physical Review B*, *79*(4), 041401.

[46] Schaffer, B., Grogger, W., Kothleitner, G., & Hofer, F. (2010). Comparison of EFTEM and STEM EELS plasmon imaging of gold nanoparticles in a monochromated TEM. *Ultramicroscopy*, *110*(8), 1087-1093.

[47] Atre, A. C., Brenny, B. J., Coenen, T., García-Etxarri, A., Polman, A., & Dionne, J. A. (2015). Nanoscale optical tomography with cathodoluminescence spectroscopy. *Nature nanotechnology*, *10*(5), 429.

[48] Losquin, A., Zagonel, L. F., Myroshnychenko, V., Rodríguez-González, B., Tencé, M., Scarabelli, L., ... & Kociak, M. (2015). Unveiling nanometer scale extinction and scattering phenomena through combined electron energy loss spectroscopy and cathodoluminescence measurements. *Nano letters*, *15*(2), 1229-1237.

[49] Nicoletti, O., de La Peña, F., Leary, R. K., Holland, D. J., Ducati, C., & Midgley, P. A. (2013). Three-dimensional imaging of localized surface plasmon resonances of metal nanoparticles. *Nature*, *502*(7469), 80.

[50] Tittl, A., Giessen, H., & Liu, N. (2014). Plasmonic gas and chemical sensing. *Nanophotonics*, *3*(3), 157-180.

[51] Lee, K. S., & El-Sayed, M. A. (2006). Gold and silver nanoparticles in sensing and imaging: sensitivity of plasmon response to size, shape, and metal composition. *The Journal of Physical Chemistry B*, *110*(39), 19220-19225.

[52] Bingham, J. M., Anker, J. N., Kreno, L. E., & Van Duyne, R. P. (2010). Gas sensing with high-resolution localized surface plasmon resonance spectroscopy. *Journal of the American Chemical Society*, *132*(49), 17358-17359.

[53] Jain, P. K., Lee, K. S., El-Sayed, I. H., & El-Sayed, M. A. (2006). Calculated absorption and scattering properties of gold nanoparticles of different size, shape, and composition: applications in biological imaging and biomedicine. *The journal of physical chemistry B*, *110*(14), 7238-7248.

[54] El-Sayed, I. H., Huang, X., & El-Sayed, M. A. (2005). Surface plasmon resonance scattering and absorption of anti-EGFR antibody conjugated gold nanoparticles in cancer diagnostics: applications in oral cancer. *Nano letters*, *5*(5), 829-834.

[55] Im, H., Shao, H., Park, Y. I., Peterson, V. M., Castro, C. M., Weissleder, R., & Lee, H. (2014). Label-free detection and molecular profiling of exosomes with a nano-plasmonic sensor. *Nature biotechnology*, *32*(5), 490.

[56] Jain, P. K., Huang, X., El-Sayed, I. H., & El-Sayed, M. A. (2008). Noble metals on the nanoscale: optical and photothermal properties and some applications in imaging, sensing, biology, and medicine. *Accounts of chemical research*, *41*(12), 1578-1586.

[57] Nath, N., & Chilkoti, A. (2004). Label-free biosensing by surface plasmon resonance of nanoparticles on glass: optimization of nanoparticle size. *Analytical Chemistry*, *76*(18), 5370-5378.

[58] Anker, J. N., Hall, W. P., Lyandres, O., Shah, N. C., Zhao, J., & Van Duyne, R. P. (2010). Biosensing with plasmonic nanosensors. In *Nanoscience and Technology: A Collection of Reviews from Nature Journals* (pp. 308-319).

[59] Liu, M., Chao, J., Deng, S., Wang, K., Li, K., & Fan, C. (2014). Dark-field microscopy in imaging of plasmon resonant nanoparticles. *Colloids and Surfaces B: Biointerfaces*, *124*, 111-117.

[60] Zapata-Herrera, M., Flórez, J., Camacho, A. S., & Ramírez, H. Y. (2018). Quantum Confinement Effects on the Near Field Enhancement in Metallic Nanoparticles. *Plasmonics*, *13*(1), 1-7.

[61] Schaadt, D. M., Feng, B., & Yu, E. T. (2005). Enhanced semiconductor optical absorption via surface plasmon excitation in metal nanoparticles. *Applied Physics Letters*, *86*(6), 063106.

[62] Pillai, S., Catchpole, K. R., Trupke, T., & Green, M. A. (2007). Surface plasmon enhanced silicon solar cells. *Journal of applied physics*, *101*(9), 093105.

[63] Hecker, N. E., Höpfel, R. A., Sawaki, N., Maier, T., & Strasser, G. (1999). Surface plasmon-enhanced photoluminescence from a single quantum well. *Applied physics letters*, *75*(11), 1577-1579.

[64] Yeshchenko, O. A., Dmitruk, I. M., Alexeenko, A. A., Losytskyy, M. Y., Kotko, A. V., & Pinchuk, A. O. (2009). Size-dependent surface-plasmon-enhanced photoluminescence from silver nanoparticles embedded in silica. *Physical Review B*, *79*(23), 235438.

[65] Liebermann, T., & Knoll, W. (2000). Surface-plasmon field-enhanced fluorescence spectroscopy. *Colloids and Surfaces A: Physicochemical and Engineering Aspects*, *171*(1-3), 115-130.

[66] Ming, T., Zhao, L., Yang, Z., Chen, H., Sun, L., Wang, J., & Yan, C. (2009). Strong polarization dependence of plasmon-enhanced fluorescence on single gold nanorods. *Nano letters*, *9*(11), 3896-3903.

[67] Talley, C. E., Jackson, J. B., Oubre, C., Grady, N. K., Hollars, C. W., Lane, S. M., ... & Halas, N. J. (2005). Surface-enhanced Raman scattering from individual Au nanoparticles and nanoparticle dimer substrates. *Nano letters*, *5*(8), 1569-1574.

[68] Chang, R. (Ed.). (2013). *Surface enhanced Raman scattering*. Springer Science & Business Media.

[69] Xu, H., & Käll, M. (2002). Surface-plasmon-enhanced optical forces in silver nanoaggregates. *Physical review letters*, *89*(24), 246802.

[70] Juan, M. L., Righini, M., & Quidant, R. (2011). Plasmon nano-optical tweezers. *Nature photonics*, *5*(6), 349.

[71] Verhagen, E., Kuipers, L., & Polman, A. (2007). Enhanced nonlinear optical effects with a tapered plasmonic waveguide. *Nano letters*, *7*(2), 334-337.

[72] Kauranen, M., & Zayats, A. V. (2012). Nonlinear plasmonics. *Nature photonics*, *6*(11), 737.

[73] Saikin, S. K., Chu, Y., Rappoport, D., Crozier, K. B., & Aspuru-Guzik, A. (2010). Separation of electromagnetic and chemical contributions to surface-enhanced Raman spectra on nanoengineered plasmonic substrates. *The Journal of Physical Chemistry Letters*, *1*(18), 2740-2746.

[74] Reilly, T. H., Chang, S. H., Corbman, J. D., Schatz, G. C., & Rowlen, K. L. (2007). Quantitative evaluation of plasmon enhanced Raman scattering from nanoaperture arrays. *The Journal of Physical Chemistry C*, *111*(4), 1689-1694.

[75] Le Ru, E., & Etchegoin, P. (2008). *Principles of Surface-Enhanced Raman Spectroscopy: and related plasmonic effects*. Elsevier.

[76] Moskovits, M. (2005). Surface-enhanced Raman spectroscopy: a brief retrospective. *Journal of Raman Spectroscopy: An International Journal for Original Work in all Aspects of Raman Spectroscopy, Including Higher Order Processes, and also Brillouin and Rayleigh Scattering*, *36*(6-7), 485-496.

[77] Tong, L., Xu, H., & Käll, M. (2014). Nanogaps for SERS applications. *Mrs Bulletin*, *39*(2), 163-168.

[78] Ding, S. Y., Yi, J., Li, J. F., Ren, B., Wu, D. Y., Panneerselvam, R., & Tian, Z. Q. (2016). Nanostructure-based plasmon-enhanced Raman spectroscopy for surface analysis of materials. *Nature Reviews Materials*, *1*(6), 16021.

[79] Nie, S., & Emory, S. R. (1997). Probing single molecules and single nanoparticles by surface-enhanced Raman scattering. *science*, *275*(5303), 1102-1106.

[80] Le Ru, E. C., Grand, J., Sow, I., Somerville, W. R., Etchegoin, P. G., Treguer-Delapierre, M., ... & Aubard, J. (2011). A scheme for detecting every single target molecule with surface-enhanced Raman spectroscopy. *Nano letters*, *11*(11), 5013-5019.

[81] Dieringer, J. A., Lettan, R. B., Scheidt, K. A., & Van Duyne, R. P. (2007). A frequency domain existence proof of single-molecule surface-enhanced Raman spectroscopy. *Journal of the American Chemical Society*, *129*(51), 16249-16256.

[82] Crozier, K. B., Zhu, W., Wang, D., Lin, S., Best, M. D., & Camden, J. P. (2014). Plasmonics for surface enhanced raman scattering: Nanoantennas for single molecules. *IEEE Journal of selected topics in quantum electronics*, *20*(3), 152-162.

[83] Ding, S. Y., Yi, J., Li, J. F., Ren, B., Wu, D. Y., Panneerselvam, R., & Tian, Z. Q. (2016). Nanostructure-based plasmon-enhanced Raman spectroscopy for surface analysis of materials. *Nature Reviews Materials*, *1*(6), 16021.

[84] Liao, P. F., & Wokaun, A. (1982). Lightning rod effect in surface enhanced Raman scattering. *The Journal of Chemical Physics*, *76*(1), 751-752.

[85] Rycenga, M., Kim, M. H., Camargo, P. H., Cobley, C., Li, Z. Y., & Xia, Y. (2009). Surface-enhanced Raman scattering: comparison of three different molecules on single-crystal

nanocubes and nanospheres of silver. *The Journal of Physical Chemistry A*, *113*(16), 3932-3939.

[86] Camargo, P. H., Au, L., Rycenga, M., Li, W., & Xia, Y. (2010). Measuring the SERS enhancement factors of dimers with different structures constructed from silver nanocubes. *Chemical physics letters*, *484*(4-6), 304-308.

[87] Inoue, M., & Ohtaka, K. (1983). Surface enhanced Raman scattering by metal spheres. I. Cluster effect. *Journal of the Physical Society of Japan*, *52*(11), 3853-3864.

[88] Xu, H., Bjerneld, E. J., Aizpurua, J., Apell, P., Gunnarsson, L., Petronis, S., ... & Kall, M. (2001, June). Interparticle coupling effects in surface-enhanced Raman scattering. In *Nanoparticles and Nanostructured Surfaces: Novel Reporters with Biological Applications* (Vol. 4258, pp. 35-43). International Society for Optics and Photonics.

[89] Zhu, W., & Crozier, K. B. (2014). Quantum mechanical limit to plasmonic enhancement as observed by surface-enhanced Raman scattering. *Nature communications*, *5*, 5228.

[90] Savage, K. J., Hawkeye, M. M., Esteban, R., Borisov, A. G., Aizpurua, J., & Baumberg, J. J. (2012). Revealing the quantum regime in tunnelling plasmonics. *Nature*, *491*(7425), 574.

[91] Hatab, N. A., Hsueh, C. H., Gaddis, A. L., Retterer, S. T., Li, J. H., Eres, G., ... & Gu, B. (2010). Free-standing optical gold bowtie nanoantenna with variable gap size for enhanced Raman spectroscopy. *Nano letters*, *10*(12), 4952-4955.

[92] Xiang, Q., Li, Z., Zheng, M., Liu, Q., Chen, Y., Yang, L., ... & Duan, H. (2018). Sensitive SERS detection at the single-particle level based on nanometer-separated mushroom-shaped plasmonic dimers. *Nanotechnology*, *29*(10), 105301.

[93] Haes, A. J., Haynes, C. L., McFarland, A. D., Schatz, G. C., Van Duyne, R. P., & Zou, S. (2005). Plasmonic materials for surface-enhanced sensing and spectroscopy. *MRS bulletin*, *30*(5), 368-375.

[94] Liu, G. L., Lu, Y., Kim, J., Doll, J. C., & Lee, L. P. (2005). Magnetic nanocrescents as controllable surface-enhanced Raman scattering nanoprobes for biomolecular imaging. *Advanced Materials*, *17*(22), 2683-2688.

[95] Etchegoin, P. G., & Le Ru, E. C. (2008). A perspective on single molecule SERS: current status and future challenges. *Physical Chemistry Chemical Physics*, *10*(40), 6079-6089.

[96] Brust, M., Walker, M., Bethell, D., Schiffrin, D. J., & Whyman, R. (1994). Synthesis of thiol-derivatised gold nanoparticles in a two-phase liquid–liquid system. *Journal of the Chemical Society, Chemical Communications*, (7), 801-802.

[97] Daniel, M. C., & Astruc, D. (2004). Gold nanoparticles: assembly, supramolecular chemistry, quantum-size-related properties, and applications toward biology, catalysis, and nanotechnology. *Chemical reviews*, *104*(1), 293-346.

[98] Romo-Herrera, J. M., Alvarez-Puebla, R. A., & Liz-Marzán, L. M. (2011). Controlled assembly of plasmonic colloidal nanoparticle clusters. *Nanoscale*, *3*(4), 1304-1315.

[99] Grzelczak, M., & Liz-Marzán, L. M. (2013). Colloidal nanoplasmonics: from building blocks to sensing devices. *Langmuir*, *29*(15), 4652-4663.

[100] Fan, J. A., Wu, C., Bao, K., Bao, J., Bardhan, R., Halas, N. J., ... & Capasso, F. (2010). Self-assembled plasmonic nanoparticle clusters. *science*, *328*(5982), 1135-1138.

[101] Hill, L. J., Pinna, N., Char, K., & Pyun, J. (2015). Colloidal polymers from inorganic nanoparticle monomers. *Progress in Polymer Science*, *40*, 85-120.

[102] Qian, Z., & Ginger, D. S. (2017). Reversibly reconfigurable colloidal plasmonic nanomaterials. *Journal of the American Chemical Society*, *139*(15), 5266-5276.

[103] Sung, K. M., Mosley, D. W., Peelle, B. R., Zhang, S., & Jacobson, J. M. (2004). Synthesis of monofunctionalized gold nanoparticles by Fmoc solid-phase reactions. *Journal of the American Chemical Society*, *126*(16), 5064-5065.

[104] Worden, J. G., Shaffer, A. W., & Huo, Q. (2004). Controlled functionalization of gold nanoparticles through a solid phase synthesis approach. *Chemical communications*, (5), 518-519.

[105] Xu, X., Rosi, N. L., Wang, Y., Huo, F., & Mirkin, C. A. (2006). Asymmetric functionalization of gold nanoparticles with oligonucleotides. *Journal of the American Chemical Society*, *128*(29), 9286-9287.

[106] Sardar, R., Heap, T. B., & Shumaker-Parry, J. S. (2007). Versatile solid phase synthesis of gold nanoparticle dimers using an asymmetric functionalization approach. *Journal of the American Chemical Society*, *129*(17), 5356-5357.

[107] Rycenga, M., McLellan, J. M., & Xia, Y. (2008). Controlling the assembly of silver nanocubes through selective functionalization of their faces. *Advanced Materials*, *20*(12), 2416-2420.

[108] Gu, H., Yang, Z., Gao, J., Chang, C. K., & Xu, B. (2005). Heterodimers of nanoparticles: formation at a liquid− liquid interface and particle-specific surface modification by functional molecules. *Journal of the American Chemical Society*, *127*(1), 34-35.

[109] Yim, T. J., Wang, Y., & Zhang, X. (2008). Synthesis of a gold nanoparticle dimer plasmonic resonator through two-phase-mediated functionalization. *Nanotechnology*, *19*(43), 435605.

[110] Wang, X., Li, G., Chen, T., Yang, M., Zhang, Z., Wu, T., & Chen, H. (2008). Polymer-encapsulated gold-nanoparticle dimers: facile preparation and catalytical application in guided growth of dimeric ZnO-nanowires. *Nano letters*, *8*(9), 2643-2647.

[111] Chen, G., Wang, Y., Tan, L. H., Yang, M., Tan, L. S., Chen, Y., & Chen, H. (2009). High-purity separation of gold nanoparticle dimers and trimers. *Journal of the American Chemical Society*, *131*(12), 4218-4219.

[112] Braun, G. B., Lee, S. J., Laurence, T., Fera, N., Fabris, L., Bazan, G. C., ... & Reich, N. O. (2009). Generalized approach to SERS-active nanomaterials via controlled nanoparticle linking, polymer encapsulation, and small-molecule infusion. *The Journal of Physical Chemistry C*, *113*(31), 13622-13629.

[113] Wang, Y., Chen, G., Yang, M., Silber, G., Xing, S., Tan, L. H., ... & Chen, H. (2010). A systems approach towards the stoichiometry-controlled hetero-assembly of nanoparticles. *Nature communications*, *1*, 87.

[114] Cho, E. C., Choi, S. W., Camargo, P. H., & Xia, Y. (2010). Thiol-induced assembly of Au nanoparticles into chainlike structures and their fixing by encapsulation in silica shells or gelatin microspheres. *Langmuir*, *26*(12), 10005-10012.

[115] Yang, M., Chen, G., Zhao, Y., Silber, G., Wang, Y., Xing, S., ... & Chen, H. (2010). Mechanistic investigation into the spontaneous linear assembly of gold nanospheres. *Physical Chemistry Chemical Physics*, *12*(38), 11850-11860.

[116] McLintock, A., Hunt, N., & Wark, A. W. (2011). Controlled side-by-side assembly of gold nanorods and dye molecules into polymer-wrapped SERRS-active clusters. *Chemical Communications*, *47*(13), 3757-3759.

[117] Nooney, R. I., Thirunavukkarasu, D., Chen, Y., Josephs, R., & Ostafin, A. E. (2003). Self-assembly of mesoporous nanoscale silica/gold composites. *Langmuir*, *19*(18), 7628-7637.

[118] Wang, H., Schaefer, K., & Moeller, M. (2008). In situ immobilization of gold nanoparticle dimers in silica nanoshell by microemulsion coalescence. *The Journal of Physical Chemistry C*, *112*(9), 3175-3178.

[119] Brown, L. O., & Doorn, S. K. (2008). A controlled and reproducible pathway to dye-tagged, encapsulated silver nanoparticles as substrates for SERS multiplexing. *Langmuir*, *24*(6), 2277-2280.

[120] Nepal, D., Park, K., & Vaia, R. A. (2012). High-Yield Assembly of Soluble and Stable Gold Nanorod Pairs for High-Temperature Plasmonics. *Small*, *8*(7), 1013-1020.

[121] Haidar, I., Lévi, G., Mouton, L., Aubard, J., Grand, J., Lau-Truong, S., ... & Boubekeur-Lecaque, L. (2016). Highly stable silica-coated gold nanorods dimers for solution-based SERS. *Physical Chemistry Chemical Physics*, *18*(47), 32272-32280.

[122] Stewart, A. F., Lee, A., Ahmed, A., Ip, S., Kumacheva, E., & Walker, G. C. (2014). Rational design for the controlled aggregation of gold nanorods via phospholipid encapsulation for enhanced Raman scattering. *ACS nano*, *8*(6), 5462-5467.

[123] Stewart, A. F., Gagnon, B. P., & Walker, G. C. (2015). Forming end-to-end oligomers of gold nanorods using porphyrins and phthalocyanines. *Langmuir*, *31*(24), 6902-6908.

[124] Alivisatos, A. P., Johnsson, K. P., Peng, X., Wilson, T. E., Loweth, C. J., Bruchez Jr, M. P., & Schultz, P. G. (1996). Organization of'nanocrystal molecules' using DNA. *Nature*, *382*(6592), 609.

[125] Loweth, C. J., Caldwell, W. B., Peng, X., Alivisatos, A. P., & Schultz, P. G. (1999). DNA-based assembly of gold nanocrystals. *Angewandte Chemie International Edition*, *38*(12), 1808-1812.

[126] Aldaye, F. A., & Sleiman, H. F. (2007). Dynamic DNA templates for discrete gold nanoparticle assemblies: control of geometry, modularity, write/erase and structural switching. *Journal of the American Chemical Society*, *129*(14), 4130-4131.

[127] Lim, D. K., Jeon, K. S., Kim, H. M., Nam, J. M., & Suh, Y. D. (2010). Nanogap-engineerable Raman-active nanodumbbells for single-molecule detection. *Nature materials*, *9*(1), 60.

[128] Connolly, S., & Fitzmaurice, D. (1999). Programmed assembly of gold nanocrystals in aqueous solution. *Advanced Materials*, *11*(14), 1202-1205.

[129] Caswell, K. K., Wilson, J. N., Bunz, U. H., & Murphy, C. J. (2003). Preferential end-to-end assembly of gold nanorods by biotin– streptavidin connectors. *Journal of the American Chemical Society*, *125*(46), 13914-13915.

[130] DeVries, G. A., Brunnbauer, M., Hu, Y., Jackson, A. M., Long, B., Neltner, B. T., ... & Stellacci, F. (2007). Divalent metal nanoparticles. *Science*, *315*(5810), 358-361.

[131] Krüger, C., Agarwal, S., & Greiner, A. (2008). Stoichiometric functionalization of gold nanoparticles in solution through a free radical polymerization approach. *Journal of the American Chemical Society*, *130*(9), 2710-2711.

[132] Brousseau III, L. C., Novak, J. P., Marinakos, S. M., & Feldheim, D. L. (1999). Assembly of phenylacetylene-bridged gold nanocluster dimers and trimers. *Advanced Materials*, *11*(6), 447-449.

[133] Novak, J. P., & Feldheim, D. L. (2000). Assembly of phenylacetylene-bridged silver and gold nanoparticle arrays. *Journal of the American Chemical Society*, *122*(16), 3979-3980.

[134] Shibu Joseph, S. T., Ipe, B. I., Pramod, P., & Thomas, K. G. (2006). Gold nanorods to nanochains: mechanistic investigations on their longitudinal assembly using α, ω-alkanedithiols and interplasmon coupling. *The Journal of Physical Chemistry B*, *110*(1), 150-157.

[135] Fabris, L., Dante, M., Nguyen, T. Q., Tok, J. B. H., & Bazan, G. C. (2008). SERS aptatags: new responsive metallic nanostructures for heterogeneous protein detection by surface enhanced Raman spectroscopy. *Advanced Functional Materials*, *18*(17), 2518-2525.

[136] Pramod, P., & Thomas, K. G. (2008). Plasmon coupling in dimers of Au nanorods. *Advanced Materials*, *20*(22), 4300-4305.

[137] Braun, G. B., Lee, S. J., Laurence, T., Fera, N., Fabris, L., Bazan, G. C., ... & Reich, N. O. (2009). Generalized approach to SERS-active nanomaterials via controlled nanoparticle linking, polymer encapsulation, and small-molecule infusion. *The Journal of Physical Chemistry C*, *113*(31), 13622-13629.

[138] Shao, L., Woo, K. C., Chen, H., Jin, Z., Wang, J., & Lin, H. Q. (2010). Angle-and energy-resolved plasmon coupling in gold nanorod dimers. *Acs Nano*, *4*(6), 3053-3062.

[139] Whitmore, D. D., El-Khoury, P. Z., Fabris, L., Chu, P., Bazan, G. C., Potma, E. O., & Apkarian, V. A. (2011). High sensitivity surface-enhanced Raman scattering in solution using engineered silver nanosphere dimers. *The Journal of Physical Chemistry C*, *115*(32), 15900-15907.

[140] Guarrotxena, N., Ren, Y., & Mikhailovsky, A. (2010). Raman response of dithiolated nanoparticle linkers. *Langmuir*, *27*(1), 347-351.

[141] Izquierdo-Lorenzo, I., Kubackova, J., Manchon, D., Mosset, A., Cottancin, E., & Sanchez-Cortes, S. (2013). Linking Ag nanoparticles by aliphatic α, ω-dithiols: a study of the aggregation and formation of interparticle hot spots. *The Journal of Physical Chemistry C*, *117*(31), 16203-16212.

[142] Indrasekara, A. S. D., Paladini, B. J., Naczynski, D. J., Starovoytov, V., Moghe, P. V., & Fabris, L. (2013). Dimeric Gold Nanoparticle Assemblies as Tags for SERS-Based Cancer Detection. *Advanced healthcare materials*, *2*(10), 1370-1376.

[143] Van Haute, D., Longmate, J. M., & Berlin, J. M. (2015). Controlled assembly of biocompatible metallic nanoaggregates using a small molecule crosslinker. *Advanced Materials*, *27*(35), 5158-5164.

[144] Brown, L. O., & Doorn, S. K. (2008). A controlled and reproducible pathway to dye-tagged, encapsulated silver nanoparticles as substrates for SERS multiplexing. *Langmuir*, *24*(6), 2277-2280.

[145] Li, W., Camargo, P. H., Lu, X., & Xia, Y. (2008). Dimers of silver nanospheres: facile synthesis and their use as hot spots for surface-enhanced Raman scattering. *Nano letters*, *9*(1), 485-490.

[146] Wang, Y., Chen, G., Yang, M., Silber, G., Xing, S., Tan, L. H., ... & Chen, H. (2010). A systems approach towards the stoichiometry-controlled hetero-assembly of nanoparticles. *Nature communications*, *1*, 87.

[147] Li, W., Camargo, P. H., Au, L., Zhang, Q., Rycenga, M., & Xia, Y. (2010). Etching and dimerization: a simple and versatile route to dimers of silver nanospheres with a range of sizes. *Angewandte Chemie International Edition*, *49*(1), 164-168.

[148] Wang, H., Schaefer, K., & Moeller, M. (2008). In situ immobilization of gold nanoparticle dimers in silica nanoshell by microemulsion coalescence. *The Journal of Physical Chemistry C*, *112*(9), 3175-3178.

[149] Cheng, L., Song, J., Yin, J., & Duan, H. (2011). Self-assembled plasmonic dimers of amphiphilic gold nanocrystals. *The Journal of Physical Chemistry Letters*, *2*(17), 2258-2262.

[150] Nepal, D., Park, K., & Vaia, R. A. (2012). High-Yield Assembly of Soluble and Stable Gold Nanorod Pairs for High-Temperature Plasmonics. *Small*, *8*(7), 1013-1020.

[151] Shanthil, M., Thomas, R., Swathi, R. S., & George Thomas, K. (2012). Ag@ SiO2 core–shell nanostructures: distance-dependent plasmon coupling and SERS investigation. *The journal of physical chemistry letters*, *3*(11), 1459-1464.

[152] Fontana, J., Charipar, N., Flom, S. R., Naciri, J., Piqué, A., & Ratna, B. R. (2016). Rise of the charge transfer plasmon: programmable concatenation of conductively linked gold nanorod dimers. *Acs Photonics*, *3*(5), 904-911.

[153] Novak, J. P., Nickerson, C., Franzen, S., & Feldheim, D. L. (2001). Purification of molecularly bridged metal nanoparticle arrays by centrifugation and size exclusion chromatography. *Analytical chemistry*, *73*(23), 5758-5761.

[154] Braun, G. B., Lee, S. J., Laurence, T., Fera, N., Fabris, L., Bazan, G. C., ... & Reich, N. O. (2009). Generalized approach to SERS-active nanomaterials via controlled nanoparticle

linking, polymer encapsulation, and small-molecule infusion. *The Journal of Physical Chemistry C*, *113*(31), 13622-13629.

[155] Tyler, T. P., Henry, A. I., Van Duyne, R. P., & Hersam, M. C. (2011). Improved monodispersity of plasmonic nanoantennas via centrifugal processing. *The Journal of Physical Chemistry Letters*, *2*(3), 218-222.

[156] Alexander, K. D., Hampton, M. J., Zhang, S., Dhawan, A., Xu, H., & Lopez, R. (2009). A high-throughput method for controlled hot-spot fabrication in SERS-active gold nanoparticle dimer arrays. *Journal of Raman Spectroscopy: An International Journal for Original Work in all Aspects of Raman Spectroscopy, Including Higher Order Processes, and also Brillouin and Rayleigh Scattering*, *40*(12), 2171-2175.

[157] Lee, S. Y., Hung, L., Lang, G. S., Cornett, J. E., Mayergoyz, I. D., & Rabin, O. (2010). Dispersion in the SERS enhancement with silver nanocube dimers. *ACS nano*, *4*(10), 5763-5772.

[158] Osberg, K. D., Rycenga, M., Harris, N., Schmucker, A. L., Langille, M. R., Schatz, G. C., & Mirkin, C. A. (2012). Dispersible gold nanorod dimers with sub-5 nm gaps as local amplifiers for surface-enhanced Raman scattering. *Nano letters*, *12*(7), 3828-3832.

[159] Brust, M., Schiffrin, D. J., Bethell, D., & Kiely, C. J. (1995). Novel gold-dithiol nano-networks with non-metallic electronic properties. *Advanced materials*, *7*(9), 795-797.

[160] Elliott III, E. W., Glover, R. D., & Hutchison, J. E. (2015). Removal of thiol ligands from surface-confined nanoparticles without particle growth or desorption. *ACS nano*, *9*(3), 3050-3059.

[161] Puspitasari, I., Skupien, E., Kapteijn, F., & Kooyman, P. (2016). Au Capping Agent Removal Using Plasma at Mild Temperature. *Catalysts*, *6*(11), 179.

[162] Mirkin, C. A., Letsinger, R. L., Mucic, R. C., & Storhoff, J. J. (1996). A DNA-based method for rationally assembling nanoparticles into macroscopic materials. *Nature*, *382*(6592), 607.

[163] Dujardin, E., Hsin, L. B., Wang, C. C., & Mann, S. (2001). DNA-driven self-assembly of gold nanorods. *Chemical Communications*, (14), 1264-1265.

[164] Hazarika, P., Ceyhan, B., & Niemeyer, C. M. (2004). Reversible switching of DNA–gold nanoparticle aggregation. *Angewandte Chemie International Edition*, *43*(47), 6469-6471.

[165] Kanaras, A. G., Wang, Z., Brust, M., Cosstick, R., & Bates, A. D. (2007). Enzymatic disassembly of DNA–gold nanostructures. *Small*, *3*(4), 590-594.

[166] Reismann, M., Bretschneider, J. C., Plessen, G. V., & Simon, U. (2008). Reversible Photothermal Melting of DNA in DNA–Gold-Nanoparticle Networks. *Small*, *4*(5), 607-610.

[167] Leunissen, M. E., Dreyfus, R., Cheong, F. C., Grier, D. G., Sha, R., Seeman, N. C., & Chaikin, P. M. (2009). Switchable self-protected attractions in DNA-functionalized colloids. *Nature materials*, *8*(7), 590.

[168] Zhang, C., Macfarlane, R. J., Young, K. L., Choi, C. H. J., Hao, L., Auyeung, E., ... & Mirkin, C. A. (2013). A general approach to DNA-programmable atom equivalents. *Nature materials*, *12*(8), 741.

[169] Liu, J., & Lu, Y. (2006). Fast colorimetric sensing of adenosine and cocaine based on a general sensor design involving aptamers and nanoparticles. *Angewandte Chemie International Edition*, *45*(1), 90-94.

[170] Zhao, W., Chiuman, W., Lam, J. C., McManus, S. A., Chen, W., Cui, Y., ... & Li, Y. (2008). DNA aptamer folding on gold nanoparticles: from colloid chemistry to biosensors. *Journal of the American Chemical Society*, *130*(11), 3610-3618.

[171] Lee, S. E., Chen, Q., Bhat, R., Petkiewicz, S., Smith, J. M., Ferry, V. E., ... & Bissell, M. J. (2015). Reversible aptamer-Au plasmon rulers for secreted single molecules. *Nano letters*, *15*(7), 4564-4570.

[172] Shenton, W., Davis, S. A., & Mann, S. (1999). Directed Self-Assembly of Nanoparticles into Macroscopic Materials Using Antibody–Antigen Recognition. *Advanced Materials*, *11*(6), 449-452.

[173] Wang, C., Chen, Y., Wang, T., Ma, Z., & Su, Z. (2007). Biorecognition-driven self-assembly of gold nanorods: a rapid and sensitive approach toward antibody sensing. *Chemistry of Materials*, *19*(24), 5809-5811.

[174] Sastry, M., Lala, N., Patil, V., Chavan, S. P., & Chittiboyina, A. G. (1998). Optical Absorption Study of the Biotin− Avidin Interaction on Colloidal Silver and Gold Particles. *Langmuir*, *14*(15), 4138-4142.

[175] Connolly, S., & Fitzmaurice, D. (1999). Programmed assembly of gold nanocrystals in aqueous solution. *Advanced Materials*, *11*(14), 1202-1205.

[176] Otsuka, H., Akiyama, Y., Nagasaki, Y., & Kataoka, K. (2001). Quantitative and reversible lectin-induced association of gold nanoparticles modified with α-lactosyl-ω-mercapto-poly (ethylene glycol). *Journal of the American Chemical Society*, *123*(34), 8226-8230.

[177] Aslan, K., Luhrs, C. C., & Pérez-Luna, V. H. (2004). Controlled and reversible aggregation of biotinylated gold nanoparticles with streptavidin. *The Journal of Physical Chemistry B*, *108*(40), 15631-15639.

[178] Lévy, R., Thanh, N. T., Doty, R. C., Hussain, I., Nichols, R. J., Schiffrin, D. J., ... & Fernig, D. G. (2004). Rational and combinatorial design of peptide capping ligands for gold nanoparticles. *Journal of the American Chemical Society*, *126*(32), 10076-10084.

[179] Aili, D., Enander, K., Rydberg, J., Lundström, I., Baltzer, L., & Liedberg, B. (2006). Aggregation-induced folding of a de novo designed polypeptide immobilized on gold nanoparticles. *Journal of the American Chemical Society*, *128*(7), 2194-2195.

[180] Shim, J. Y., & Gupta, V. K. (2007). Reversible aggregation of gold nanoparticles induced by pH dependent conformational transitions of a self-assembled polypeptide. *Journal of colloid and interface science*, *316*(2), 977-983.

[181] Si, S., & Mandal, T. K. (2007). pH-controlled reversible assembly of peptide-functionalized gold nanoparticles. *Langmuir*, *23*(1), 190-195.

[182] Tan, J., Liu, R., Wang, W., Liu, W., Tian, Y., Wu, M., & Huang, Y. (2009). Controllable aggregation and reversible pH sensitivity of AuNPs regulated by carboxymethyl cellulose. *Langmuir*, *26*(3), 2093-2098.

[183] Li, W., Kanyo, I., Kuo, C. H., Thanneeru, S., & He, J. (2015). pH-programmable self-assembly of plasmonic nanoparticles: hydrophobic interaction versus electrostatic repulsion. *Nanoscale*, *7*(3), 956-964.

[184] Raula, J., Shan, J., Nuopponen, M., Niskanen, A., Jiang, H., Kauppinen, E. I., & Tenhu, H. (2003). Synthesis of gold nanoparticles grafted with a thermoresponsive polymer by

surface-induced reversible-addition-fragmentation chain-transfer polymerization. *Langmuir*, *19*(8), 3499-3504.

[185] Zhu, M. Q., Wang, L. Q., Exarhos, G. J., & Li, A. D. (2004). Thermosensitive gold nanoparticles. *Journal of the American Chemical Society*, *126*(9), 2656-2657.

[186] Lemieux, V., Adams, P. H. H., & van Hest, J. C. (2010). Elastin-based stimuli-responsive gold nanoparticles. *Chemical Communications*, *46*(18), 3071-3073.

[187] Durand-Gasselin, C., Capelot, M., Sanson, N., & Lequeux, N. (2010). Tunable and Reversible Aggregation of Poly (ethylene oxide-st-propylene oxide) Grafted Gold Nanoparticles. *Langmuir*, *26*(14), 12321-12329.

[188] Durand-Gasselin, C., Sanson, N., & Lequeux, N. (2011). Reversible controlled assembly of thermosensitive polymer-coated gold nanoparticles. *Langmuir*, *27*(20), 12329-12335.

[189] Fava, D., Winnik, M. A., & Kumacheva, E. (2009). Photothermally-triggered self-assembly of gold nanorods. *Chemical Communications*, (18), 2571-2573.

[190] Han, H., Lee, J. Y., & Lu, X. (2013). Thermoresponsive nanoparticles+ plasmonic nanoparticles= photoresponsive heterodimers: Facile synthesis and sunlight-induced reversible clustering. *Chemical Communications*, *49*(55), 6122-6124.

[191] Ding, T., Valev, V. K., Salmon, A. R., Forman, C. J., Smoukov, S. K., Scherman, O. A., ... & Baumberg, J. J. (2016). Light-induced actuating nanotransducers. *Proceedings of the National Academy of Sciences*, *113*(20), 5503-5507.

[192] Liu, K., Nie, Z., Zhao, N., Li, W., Rubinstein, M., & Kumacheva, E. (2010). Step-growth polymerization of inorganic nanoparticles. *science*, *329*(5988), 197-200.

[193] Sánchez-Iglesias, A., Grzelczak, M., Altantzis, T., Goris, B., Perez-Juste, J., Bals, S., ... & Liz-Marzán, L. M. (2012). Hydrophobic interactions modulate self-assembly of nanoparticles. *ACS nano*, *6*(12), 11059-11065.

[194] Choueiri, R. M., Galati, E., Klinkova, A., Thérien-Aubin, H., & Kumacheva, E. (2016). Linear assembly of patchy and non-patchy nanoparticles. *Faraday discussions*, *191*, 189-204.

[195] Cheng, L., Song, J., Yin, J., & Duan, H. (2011). Self-assembled plasmonic dimers of amphiphilic gold nanocrystals. *The Journal of Physical Chemistry Letters*, *2*(17), 2258-2262.

[196] Kitayama, Y., & Takeuchi, T. (2014). Synthesis of CO2/N2-Triggered Reversible Stability-Controllable Poly (2-(diethylamino) ethyl methacrylate)-grafted-AuNPs by Surface-Initiated Atom Transfer Radical Polymerization. *Langmuir*, *30*(42), 12684-12689.

[197] Fullam, S., Rao, S. N., & Fitzmaurice, D. (2000). Noncovalent self-assembly of silver nanocrystal aggregates in solution. *The Journal of Physical Chemistry B*, *104*(26), 6164-6173.

[198] Boal, A. K., Ilhan, F., DeRouchey, J. E., Thurn-Albrecht, T., Russell, T. P., & Rotello, V. M. (2000). Self-assembly of nanoparticles into structured spherical and network aggregates. *Nature*, *404*(6779), 746.

[199] Zheng, W., Maye, M. M., Leibowitz, F. L., & Zhong, C. J. (2000). Imparting biomimetic ion-gating recognition properties to electrodes with a hydrogen-bonding structured core− shell nanoparticle network. *Analytical chemistry*, *72*(10), 2190-2199.

[200] Mandal, S., Gole, A., Lala, N., Gonnade, R., Ganvir, V., & Sastry, M. (2001). Studies on the reversible aggregation of cysteine-capped colloidal silver particles interconnected via hydrogen bonds. *Langmuir*, *17*(20), 6262-6268.

[201] Li, G., Wang, T., Bhosale, S., Zhang, Y., & Fuhrhop, J. H. (2003). Completely reversible aggregation of nanoparticles by varying the pH. *Colloid and Polymer Science*, *281*(11), 1099-1103.

[202] Thomas, K. G., Barazzouk, S., Ipe, B. I., Joseph, S. S., & Kamat, P. V. (2004). Uniaxial plasmon coupling through longitudinal self-assembly of gold nanorods. *The Journal of Physical Chemistry B*, *108*(35), 13066-13068.

[203] Templeton, A. C., Zamborini, F. P., Wuelfing, W. P., & Murray, R. W. (2000). Controlled and Reversible Formation of Nanoparticle Aggregates and Films Using Cu2+− Carboxylate Chemistry. *Langmuir*, *16*(16), 6682-6688.

[204] Kim, Y., Johnson, R. C., & Hupp, J. T. (2001). Gold nanoparticle-based sensing of "spectroscopically silent" heavy metal ions. *Nano Letters*, *1*(4), 165-167.

[205] Norsten, T. B., Frankamp, B. L., & Rotello, V. M. (2002). Metal directed assembly of terpyridine-functionalized gold nanoparticles. *Nano Letters*, *2*(12), 1345-1348.

[206] Si, S., Raula, M., Paira, T. K., & Mandal, T. K. (2008). Reversible Self-Assembly of Carboxylated Peptide-Functionalized Gold Nanoparticles Driven by Metal-Ion Coordination. *ChemPhysChem*, *9*(11), 1578-1584.

[207] Sreeprasad, T. S., & Pradeep, T. (2011). Reversible assembly and disassembly of gold nanorods induced by EDTA and its application in SERS tuning. *Langmuir*, *27*(7), 3381-3390.

[208] Liu, J., Mendoza, S., Román, E., Lynn, M. J., Xu, R., & Kaifer, A. E. (1999). Cyclodextrin-modified gold nanospheres. host− guest interactions at work to control colloidal properties. *Journal of the American Chemical Society*, *121*(17), 4304-4305.

[209] Lin, S. Y., Liu, S. W., Lin, C. M., & Chen, C. H. (2002). Recognition of potassium ion in water by 15-crown-5 functionalized gold nanoparticles. *Analytical chemistry*, *74*(2), 330-335.

[210] Liu, Z., & Jiang, M. (2007). Reversible aggregation of gold nanoparticles driven by inclusion complexation. *Journal of Materials Chemistry*, *17*(40), 4249-4254.

[211] Olson, M. A., Coskun, A., Klajn, R., Fang, L., Dey, S. K., Browne, K. P., ... & Stoddart, J. F. (2009). Assembly of polygonal nanoparticle clusters directed by reversible noncovalent bonding interactions. *Nano letters*, *9*(9), 3185-3190.

[212] Yao, Y., Jie, K., Zhou, Y., & Xue, M. (2014). Reversible assembly of silver nanoparticles driven by host–guest interactions based on water-soluble pillar [n] arenes. *Chemical Communications*, *50*(39), 5072-5074.

[213] Naka, K., Itoh, H., & Chujo, Y. (2003). Temperature-dependent reversible self-assembly of gold nanoparticles into spherical aggregates by molecular recognition between pyrenyl and dinitrophenyl units. *Langmuir*, *19*(13), 5496-5501.

[214] Han, X., Goebl, J., Lu, Z., & Yin, Y. (2011). Role of salt in the spontaneous assembly of charged gold nanoparticles in ethanol. *Langmuir*, *27*(9), 5282-5289.

[215] Liu, Y., Han, X., He, L., & Yin, Y. (2012). Thermoresponsive assembly of charged gold nanoparticles and their reversible tuning of plasmon coupling. *Angewandte Chemie International Edition*, *51*(26), 6373-6377.

[216] Sidhaye, D. S., Kashyap, S., Sastry, M., Hotha, S., & Prasad, B. L. V. (2005). Gold nanoparticle networks with photoresponsive interparticle spacings. *Langmuir*, *21*(17), 7979-7984.

[217] Klajn, R., Bishop, K. J., & Grzybowski, B. A. (2007). Light-controlled self-assembly of reversible and irreversible nanoparticle suprastructures. *Proceedings of the National Academy of Sciences*, *104*(25), 10305-10309.

[218] Klajn, R., Wesson, P. J., Bishop, K. J., & Grzybowski, B. A. (2009). Writing self-erasing images using metastable nanoparticle "inks". *Angewandte Chemie International Edition*, *48*(38), 7035-7039.

[219] Wei, Y., Han, S., Kim, J., Soh, S., & Grzybowski, B. A. (2010). Photoswitchable catalysis mediated by dynamic aggregation of nanoparticles. *Journal of the American Chemical Society*, *132*(32), 11018-11020.

[220] Yan, Y., Chen, J. I., & Ginger, D. S. (2012). Photoswitchable oligonucleotide-modified gold nanoparticles: Controlling hybridization stringency with photon dose. *Nano letters*, *12*(5), 2530-2536.

[221] Kim, T., Lee, K., Gong, M. S., & Joo, S. W. (2005). Control of gold nanoparticle aggregates by manipulation of interparticle interaction. *Langmuir*, *21*(21), 9524-9528.

[222] Lin, S., Li, M., Dujardin, E., Girard, C., & Mann, S. (2005). One-dimensional plasmon coupling by facile self-assembly of gold nanoparticles into branched chain networks. *Advanced Materials*, *17*(21), 2553-2559.

[223] Maye, M. M., Lim, I. I. S., Luo, J., Rab, Z., Rabinovich, D., Liu, T., & Zhong, C. J. (2005). Mediator− template assembly of nanoparticles. *Journal of the American Chemical Society*, *127*(5), 1519-1529.

[224] Zhang, H., Fung, K. H., Hartmann, J., Chan, C. T., & Wang, D. (2008). Controlled chainlike agglomeration of charged gold nanoparticles via a deliberate interaction balance. *The journal of physical chemistry C*, *112*(43), 16830-16839.

[225] Sreeprasad, T. S., Samal, A. K., & Pradeep, T. (2008). One-, two-, and three-dimensional superstructures of gold nanorods induced by dimercaptosuccinic acid. *Langmuir*, *24*(9), 4589-4599.

[226] Cho, E. C., Choi, S. W., Camargo, P. H., & Xia, Y. (2010). Thiol-induced assembly of Au nanoparticles into chainlike structures and their fixing by encapsulation in silica shells or gelatin microspheres. *Langmuir*, *26*(12), 10005-10012.

[227] Li, M., Johnson, S., Guo, H., Dujardin, E., & Mann, S. (2011). A Generalized Mechanism for Ligand-Induced Dipolar Assembly of Plasmonic Gold Nanoparticle Chain Networks. *Advanced Functional Materials*, *21*(5), 851-859.

[228] Lin, L., Peng, X., Wang, M., Scarabelli, L., Mao, Z., Liz-Marzán, L. M., ... & Zheng, Y. (2016). Light-directed reversible assembly of plasmonic nanoparticles using plasmon-enhanced thermophoresis. *ACS nano*, *10*(10), 9659-9668.

[229] Patra, P. P., Chikkaraddy, R., Tripathi, R. P., Dasgupta, A., & Kumar, G. P. (2014). Plasmofluidic single-molecule surface-enhanced Raman scattering from dynamic assembly of plasmonic nanoparticles. *Nature communications*, *5*, 4357.

[230] He, H., Feng, M., Chen, Q., Zhang, X., & Zhan, H. (2016). Light-Induced Reversible Self-Assembly of Gold Nanoparticles Surface-Immobilized with Coumarin Ligands. *Angewandte Chemie International Edition*, *55*(3), 936-940.

[231] Guarise, C., Pasquato, L., & Scrimin, P. (2005). Reversible aggregation/deaggregation of gold nanoparticles induced by a cleavable dithiol linker. *Langmuir*, *21*(12), 5537-5541.

[232] Lim, I. I. S., Vaiana, C., Zhang, Z. Y., Zhang, Y. J., An, D. L., & Zhong, C. J. (2007). X-shaped rigid arylethynes to mediate the assembly of nanoparticles. *Journal of the American Chemical Society*, *129*(17), 5368-5369.

[233] O'regan, B., & Grätzel, M. (1991). A low-cost, high-efficiency solar cell based on dye-sensitized colloidal TiO2 films. *nature*, *353*(6346), 737.

[234] Skrabalak, S. E., Au, L., Li, X., & Xia, Y. (2007). Facile synthesis of Ag nanocubes and Au nanocages. *Nature protocols*, *2*(9), 2182.

[235] Luo, M., Hong, Y., Yao, W., Huang, C., Xu, Q., & Wu, Q. (2015). Facile removal of polyvinylpyrrolidone (PVP) adsorbates from Pt alloy nanoparticles. *Journal of Materials Chemistry A*, *3*(6), 2770-2775.

[236] Henzie, J., Andrews, S. C., Ling, X. Y., Li, Z., & Yang, P. (2013). Oriented assembly of polyhedral plasmonic nanoparticle clusters. *Proceedings of the National Academy of Sciences*, *110*(17), 6640-6645.

[237] Bastús, N. G., Comenge, J., & Puntes, V. (2011). Kinetically controlled seeded growth synthesis of citrate-stabilized gold nanoparticles of up to 200 nm: size focusing versus Ostwald ripening. *Langmuir*, *27*(17), 11098-11105.

[238] Puurunen, R. L. (2005). Surface chemistry of atomic layer deposition: A case study for the trimethylaluminum/water process. *Journal of applied physics*, *97*(12), 9.

[239] Kirihara, M., Asai, Y., Ogawa, S., Noguchi, T., Hatano, A., & Hirai, Y. (2007). A mild and environmentally benign oxidation of thiols to disulfides. *Synthesis*, *2007*(21), 3286-3289.

[240] Castner, D. G., Hinds, K., & Grainger, D. W. (1996). X-ray photoelectron spectroscopy sulfur 2p study of organic thiol and disulfide binding interactions with gold surfaces. *Langmuir*, *12*(21), 5083-5086.

[241] Noh, J., Jang, S., Lee, D., Shin, S., Ko, Y. J., Ito, E., & Joo, S. W. (2007). Abnormal adsorption behavior of dimethyl disulfide on gold surfaces. *Current Applied Physics*, *7*(6), 605-610.

[242] Levanov, A. V., Isaikina, O. Y., Tyutyunnik, A. N., Antipenko, E. E., & Lunin, V. V. (2016). Molar absorption coefficient of ozone in aqueous solutions. *Journal of Analytical Chemistry*, *71*(6), 549-553.

[243] Banik, M., Rodriguez, K., Hulkko, E., & Apkarian, V. A. (2016). Orientation-dependent handedness of chiral plasmons on nanosphere dimers: How to turn a right hand into a left hand. *ACS Photonics*, *3*(12), 2482-2489.

[244] Ilavsky, J. (2012). Nika: software for two-dimensional data reduction. *Journal of Applied Crystallography*, *45*(2), 324-328.

[245] Johnson, P. B., & Christy, R. W. (1972). Optical constants of the noble metals. *Physical review B*, *6*(12), 4370.

[246] Skrabalak, S. E., Au, L., Li, X., & Xia, Y. (2007). Facile synthesis of Ag nanocubes and Au nanocages. *Nature protocols*, *2*(9), 2182.

[247] Wiley, B. J., Im, S. H., Li, Z. Y., McLellan, J., Siekkinen, A., & Xia, Y. (2006). Maneuvering the surface plasmon resonance of silver nanostructures through shape-controlled synthesis.

[248] Qiu, Z., Zhang, M., Wu, D. Y., Ding, S. Y., Zuo, Q. Q., Huang, Y. F., ... & Mao, B. W. (2013). Raman spectroscopic investigation on TiO2–N719 dye interfaces using Ag@ TiO2 nanoparticles and potential correlation strategies. *ChemPhysChem*, *14*(10), 2217-2224.

[249] Banik, M., Nag, A., El-Khoury, P. Z., Rodriguez Perez, A., Guarrotxena, N., Bazan, G. C., & Apkarian, V. A. (2012). Surface-enhanced Raman scattering of a single nanodumbbell: dibenzyldithio-linked silver nanospheres. *The Journal of Physical Chemistry C*, *116*(18), 10415-10423.

[250] Guarrotxena, N., Ren, Y., & Mikhailovsky, A. (2010). Raman response of dithiolated nanoparticle linkers. *Langmuir*, *27*(1), 347-351.

[251] Ahonen, P., Laaksonen, T., Nykänen, A., Ruokolainen, J., & Kontturi, K. (2006). Formation of stable Ag-nanoparticle aggregates induced by dithiol cross-linking. *The Journal of Physical Chemistry B*, *110*(26), 12954-12958.

[252] Lee, K. E., Gomez, M. A., Elouatik, S., & Demopoulos, G. P. (2010). Further understanding of the adsorption mechanism of N719 sensitizer on anatase TiO2 films for DSSC applications using vibrational spectroscopy and confocal Raman imaging. *Langmuir*, *26*(12), 9575-9583.

[253] Pérez León, C., Kador, L., Peng, B., & Thelakkat, M. (2006). Characterization of the adsorption of Ru-bpy dyes on mesoporous TiO2 films with UV− Vis, Raman, and FTIR spectroscopies. *The Journal of Physical Chemistry B*, *110*(17), 8723-8730.

[254] Díaz, E., Valenciano, R. B., & Katime, I. A. (2004). Study of complexes of poly (vinyl pyrrolidone) with copper and cobalt on solid state. *Journal of applied polymer science*, *93*(4), 1512-1518.

[255] Vanysek, P. (2000). Electrochemical series. *CRC handbook of chemistry and physics*, *8*.

[256] Crespo-Quesada, M., Andanson, J. M., Yarulin, A., Lim, B., Xia, Y., & Kiwi-Minsker, L. (2011). UV–ozone cleaning of supported poly (vinylpyrrolidone)-stabilized palladium

nanocubes: effect of stabilizer removal on morphology and catalytic behavior. *Langmuir*, *27*(12), 7909-7916.

[257] Luo, M., Hong, Y., Yao, W., Huang, C., Xu, Q., & Wu, Q. (2015). Facile removal of polyvinylpyrrolidone (PVP) adsorbates from Pt alloy nanoparticles. *Journal of Materials Chemistry A*, *3*(6), 2770-2775.

[258] Henzie, J., Andrews, S. C., Ling, X. Y., Li, Z., & Yang, P. (2013). Oriented assembly of polyhedral plasmonic nanoparticle clusters. *Proceedings of the National Academy of Sciences*, *110*(17), 6640-6645.

[259] Rycenga, M., Camargo, P. H., Li, W., Moran, C. H., & Xia, Y. (2010). Understanding the SERS effects of single silver nanoparticles and their dimers, one at a time. *The journal of physical chemistry letters*, *1*(4), 696-703.

[260] Banik, M., Nag, A., El-Khoury, P. Z., Rodriguez Perez, A., Guarrotxena, N., Bazan, G. C., & Apkarian, V. A. (2012). Surface-enhanced Raman scattering of a single nanodumbbell: dibenzyldithio-linked silver nanospheres. *The Journal of Physical Chemistry C*, *116*(18), 10415-10423.

[261] Guarrotxena, N., & Bazan, G. C. (2014). Antitags: SERS-Encoded Nanoparticle Assemblies that Enable Single-Spot Multiplex Protein Detection. *Advanced Materials*, *26*(12), 1941-1946.

[262] Xu, H., Bjerneld, E. J., Aizpurua, J., Apell, P., Gunnarsson, L., Petronis, S., ... & Kall, M. (2001, June). Interparticle coupling effects in surface-enhanced Raman scattering. In *Nanoparticles and Nanostructured Surfaces: Novel Reporters with Biological Applications* (Vol. 4258, pp. 35-43). International Society for Optics and Photonics.

[263] Wustholz, K. L., Henry, A. I., McMahon, J. M., Freeman, R. G., Valley, N., Piotti, M. E., ... & Van Duyne, R. P. (2010). Structure− activity relationships in gold nanoparticle dimers and trimers for surface-enhanced Raman spectroscopy. *Journal of the American Chemical Society*, *132*(31), 10903-10910.

[264] Morozov, P. A., Ershov, B. G., Abkhalimov, E. V., Dement'eva, O. V., Rumyantseva, T. B., Rudoy, V. M., & Roldughin, V. I. (2011). Aggregation stability of gold citrate hydrosol: Effect of ozone. *Colloid journal*, *73*(5), 668.

[265] Puckett, S. D., Heuser, J. A., Keith, J. D., Spendel, W. U., & Pacey, G. E. (2005). Interaction of ozone with gold nanoparticles. *Talanta*, *66*(5), 1242-1246.

[266] Ershov, B. G., Abkhalimov, E. V., Roldughin, V. I., Rudoy, V. M., Dement'eva, O. V., & Solovov, R. D. (2015). Adsorption of ozone and plasmonic properties of gold hydrosol: the effect of the nanoparticle size. *Physical Chemistry Chemical Physics*, *17*(28), 18431-18436.

[267] Morozov, P. A., Ershov, B. G., Abkhalimov, E. V., Dement'eva, O. V., Filippenko, M. A., Rudoy, V. M., & Roldughin, V. I. (2012). The effect of ozone on plasmon absorption of gold hydrosols. Quasi-metal and metal nanoparticles. *Colloid Journal*, *74*(4), 502-509.

[268] Cataldo, F., Ursini, O., & Angelini, G. (2016). COLLOIDAL GOLD NANOPARTICLES: Interaction with ozone and analytical potential. *European Chemical Bulletin*, *5*(1), 1-7.

[269] Park, J. W., & Shumaker-Parry, J. S. (2015). Strong resistance of citrate anions on metal nanoparticles to desorption under thiol functionalization. *ACS nano*, *9*(2), 1665-1682.

[270] Park, J. W., & Shumaker-Parry, J. S. (2014). Structural study of citrate layers on gold nanoparticles: role of intermolecular interactions in stabilizing nanoparticles. *Journal of the American Chemical Society*, *136*(5), 1907-1921.

[271] Otera, J., & Nishikido, J. (2009). *Esterification: methods, reactions, and applications*. John Wiley & Sons.

[272] Garrell, R. L., Chadwick, J. E., Severance, D. L., McDonald, N. A., & Myles, D. C. (1995). Adsorption of sulfur containing molecules on gold: the effect of oxidation on monolayer formation and stability characterized by experiments and theory. *Journal of the American Chemical Society*, *117*(46), 11563-11571.

[273] Joseph, Y., Guse, B., & Nelles, G. (2009). Aging of 1, ω-alkyldithiol interlinked au nanoparticle networks. *Chemistry of Materials*, *21*(8), 1670-1676.

[274] Mahou, R., & Wandrey, C. (2012). Versatile route to synthesize heterobifunctional poly (ethylene glycol) of variable functionality for subsequent pegylation. *Polymers*, *4*(1), 561-589.

[275] Andreozzi, R., Caprio, V., & Insola, A. (1996). Kinetics and mechanisms of polyethyleneglycol fragmentation by ozone in aqueous solution. *Water Research*, *30*(12), 2955-2960.

[276] Suzuki, J. (1976). Study on ozone treatment of water-soluble polymers. I. Ozone degradation of polyethylene glycol in water. *Journal of applied polymer science*, *20*(1), 93-103.

[277] Bordwell, F. G. (1988). Equilibrium acidities in dimethyl sulfoxide solution. *Accounts of Chemical Research*, *21*(12), 456-463.

[278] Smith, M. B., & March, J. (2007). *March's advanced organic chemistry: reactions, mechanisms, and structure*. John Wiley & Sons.

[279] Oae, S., & Doi, J. T. (1991). *Organic sulfur chemistry: structure and mechanism* (Vol. 1). Boca Raton, FL: CRC Press.

[280] McGrath, A. J., Garrett, G. E., Valgimigli, L., & Pratt, D. A. (2010). The redox chemistry of sulfenic acids. *Journal of the American Chemical Society*, *132*(47), 16759-16761.

[281] Malz, F., & Jancke, H. (2005). Validation of quantitative NMR. *Journal of pharmaceutical and biomedical analysis*, *38*(5), 813-823.

[282] Wuelfing, W. P., Gross, S. M., Miles, D. T., & Murray, R. W. (1998). Nanometer gold clusters protected by surface-bound monolayers of thiolated poly (ethylene glycol) polymer electrolyte. *Journal of the American Chemical Society*, *120*(48), 12696-12697.

[283] Bartz, M., Küther, J., Nelles, G., Weber, N., Seshadri, R., & Tremel, W. (1999). Monothiols derived from glycols as agents for stabilizing gold colloids in water: synthesis, self-assembly and use as crystallization templates. *Journal of Materials Chemistry*, *9*(5), 1121-1125.

[284] Foos, E. E., Snow, A. W., Twigg, M. E., & Ancona, M. G. (2002). Thiol-terminated di-, tri-, and tetraethylene oxide functionalized gold nanoparticles: a water-soluble, charge-neutral cluster. *Chemistry of Materials*, *14*(5), 2401-2408.

[285] Kanaras, A. G., Kamounah, F. S., Schaumburg, K., Kiely, C. J., & Brust, M. (2002). Thioalkylated tetraethylene glycol: a new ligand for water soluble monolayer protected gold clusters. *Chemical communications*, (20), 2294-2295.

[286] Bigall, N. C., Reitzig, M., Naumann, W., Simon, P., van Pée, K. H., & Eychmüller, A. (2008). Fungal templates for noble-metal nanoparticles and their application in catalysis. *Angewandte Chemie International Edition*, *47*(41), 7876-7879.

[287] Kassam, A., Bremner, G., Clark, B., Ulibarri, G., & Lennox, R. B. (2006). Place exchange reactions of alkyl thiols on gold nanoparticles. *Journal of the American Chemical Society*, *128*(11), 3476-3477.

[288] Kluenker, M., Mondeshki, M., Nawaz Tahir, M., & Tremel, W. (2018). Monitoring Thiol–Ligand Exchange on Au Nanoparticle Surfaces. *Langmuir*, *34*(4), 1700-1710.

[289] Alderighi, L., Gans, P., Ienco, A., Peters, D., Sabatini, A., & Vacca, A. (1999). Hyperquad simulation and speciation (HySS): a utility program for the investigation of equilibria involving soluble and partially soluble species. *Coordination chemistry reviews*, *184*(1), 311-318.

[290] Tijunelyte, I., Guenin, E., Lidgi-Guigui, N., Colas, F., Ibrahim, J., Toury, T., & de la Chapelle, M. L. (2016). Nanoplasmonics tuned "click chemistry". *Nanoscale*, *8*(13), 7105-7112.

[291] Sundararaman, R., Narang, P., Jermyn, A. S., Goddard III, W. A., & Atwater, H. A. (2014). Theoretical predictions for hot-carrier generation from surface plasmon decay. *Nature communications*, *5*, 5788.

[292] Hermanson, G. T. (2013). *Bioconjugate techniques*. Academic press.

[293] Northrop, B. H., Frayne, S. H., & Choudhary, U. (2015). Thiol–maleimide "click" chemistry: evaluating the influence of solvent, initiator, and thiol on the reaction mechanism, kinetics, and selectivity. *Polymer Chemistry*, *6*(18), 3415-3430.

[294] Lowe, A. B. (2010). Thiol-ene "click" reactions and recent applications in polymer and materials synthesis. *Polymer Chemistry*, *1*(1), 17-36.

[295] Hoyle, C. E., & Bowman, C. N. (2010). Thiol–ene click chemistry. *Angewandte Chemie International Edition*, *49*(9), 1540-1573.

[296] Nair, D. P., Podgorski, M., Chatani, S., Gong, T., Xi, W., Fenoli, C. R., & Bowman, C. N. (2013). The thiol-Michael addition click reaction: a powerful and widely used tool in materials chemistry. *Chemistry of Materials*, *26*(1), 724-744.